STUDY OF CRYSTAL MORPHOLOGIES OF HYDROGENATED CASTOR OIL AS A RHEOLOGY MODIFIER

STUDY OF CRYSTAL MORPHOLOGIES OF HYDROGENATED CASTOR OIL AS A RHEOLOGY MODIFIER

By

DINGZHENG YANG, B. ENG., M. A. Sc.

A Thesis
Submitted to the School of Graduate Studies
in Partial Fulfillment of the Requirements
for the Degree
Doctor of Philosophy

McMaster University
© Copyright by Dingzheng Yang, April 2012

DOCTOR OF PHILOSOPHY (2012)　McMaster University
(Chemical Engineering)　Hamilton, Ontario

TITLE: Study of Crystal Morphologies of Hydrogenated Castor Oil as a Rheology Modifier
AUTHOR: Dingzheng Yang
B.ENG. (Hebei University of Technology)
M.A.Sc. (Tianjin University)
SUPERVISOR: Professor Andrew N. Hrymak
NUMBER OF PAGES: xi, 115

Welcome | Log in | Cart (0) | Manage Account | Feedback | Help | Live Help

GET PERMISSION | LICENSE YOUR CONTENT | PRODUCTS AND SOLUTIONS | PARTNERS | EDUCATION | ABOUT US

Get Permission / Find Title

Industrial & engineering chemistry rese Go

Advanced Search Options

Industrial & engineering chemistry research

ISSN: 0888-5885
Publication year(s): 1987 - present
Author/Editor: AMERICAN CHEMICAL SOCIETY
Publication type: Journal
Publisher: AMERICAN CHEMICAL SOCIETY,
Rightsholder: AMERICAN CHEMICAL SOCIETY
Language: English
Country of publication: United States of America

Permission type selected: Republish or display content

Type of use selected: reuse in a Thesis/Dissertation

Select different permission

Article title: Crystal Morphology of Hydrogenated Castor Oil in the Crystallization of Oil-in-Water Emulsions: Part I. Effect of Temperature
Author(s): Yang, Dingzheng ; Hrymak, Andrew N.
DOI: 10.1021/IE1025985
Date: Oct 19, 2011
Volume: 50
Issue: 20

Select different article

PERMISSION/LICENSE IS GRANTED FOR YOUR ORDER AT NO CHARGE

This type of permission/license, instead of the standard Terms & Conditions, is sent to you because no fee is being charged for your order. Please note the following:

- Permission is granted for your request in both print and electronic formats.
- If figures and/or tables were requested, they may be adapted or used in part.
- Please print this page for your records and send a copy of it to your publisher/graduate school.
- Appropriate credit for the requested material should be given as follows: "Reprinted (adapted) with permission from (COMPLETE REFERENCE CITATION). Copyright (YEAR) American Chemical Society." Insert appropriate information in place of the capitalized words.
- One-time permission is granted only for the use specified in your request. No additional uses are granted (such as derivative works or other editions). For any other uses, please submit a new request.

Back

Get Permission | License Your Content | Products & Solutions | Partners | Education | About CCC
Privacy Policy | Terms & Conditions

Copyright 2012 Copyright Clearance Center

Industrial & engineering chemistry research

ISSN:	0888-5885	**Language:**	English
Publication year(s):	1987 - present	**Country of publication:**	United States of America
Author/Editor:	AMERICAN CHEMICAL SOCIETY		
Publication type:	Journal		
Publisher:	AMERICAN CHEMICAL SOCIETY,		
Rightsholder:	AMERICAN CHEMICAL SOCIETY		

Permission type selected: Republish or display content

Type of use selected: reuse in a Thesis/Dissertation

Select different permission

Article title: Crystal Morphology of Hydrogenated Castor Oil in the Crystallization of Oil-in-Water Emulsions: Part II. Effect of Shear
Author(s): Yang, Dingzheng ; Hrymak, Andrew N. ; Kamal, Musa R.
DOI: 10.1021/IE1025997
Date: Oct 19, 2011
Volume: 50
Issue: 20

Select different article

PERMISSION/LICENSE IS GRANTED FOR YOUR ORDER AT NO CHARGE

This type of permission/license, instead of the standard Terms & Conditions, is sent to you because no fee is being charged for your order. Please note the following:

- Permission is granted for your request in both print and electronic formats.
- If figures and/or tables were requested, they may be adapted or used in part.
- Please print this page for your records and send a copy of it to your publisher/graduate school.
- Appropriate credit for the requested material should be given as follows: "Reprinted (adapted) with permission from (COMPLETE REFERENCE CITATION). Copyright (YEAR) American Chemical Society." Insert appropriate information in place of the capitalized words.
- One-time permission is granted only for the use specified in your request. No additional uses are granted (such as derivative works or other editions). For any other uses, please submit a new request.

Back

Copyright 2012 Copyright Clearance Center

Abstract

Hydrogenated castor oil (HCO) crystals as a rheology modifier have been widely used in paints, cosmetics and household products. In this thesis, we are interested in the effect of crystal morphology on the suspension rheology of products. Three major types of micron-sized crystal morphologies have been observed: fiber, rosette and irregular crystal. Fibers show a high aspect ratio with the length ranging from 5 to 33 µm and width around 1~3 µm. The rosette (2~50 µm) is a three-dimensional spherulitic structure with nano-fibrous arms extruding from a heterogeneous central point. Irregular crystals with equivalent diameter ranging from 4 to 84 µm are hard solid and show irregular shapes. There is an additional fourth type of crystal morphology which is a nano-sized fibrous structure that is assumed to be broken down from arms of micron-sized rosettes and fibers. Due to the relatively small amount, the effects of nano-fibrous fragments on rheology were not considered separately in this work.

The effect of temperature and shear history on the HCO crystal morphology has been studied. The energy barrier to nucleation for fibers is suggested to be higher than that of rosettes. Irregular crystals are thermodynamically less stable and tend to transform into stable polymorphs. A non-isothermal crystallization study showed that the formation of rosettes and fibers was favored by a slow cooling rate (1°C/min) while the formation of irregular crystals was favored by a fast cooling rate (5°C/min). Shear rates from zero to 100 s^{-1} have been applied at cooling rates from 1°C/min to 5°C/min. Nucleation has been found to be promoted with the increase of shear rate. Morphological analysis indicated that the formation of fibers was favored by gentle shear (e.g., 1 s^{-1}), but fibers can be broken with the increase of shear time.

Kinetics of isothermal crystallization of hydrogenated castor oil in water emulsions exhibiting multiple crystal morphologies has been studied in the temperature range of 55°C to 70°C. The induction time of nucleation increases with the increase of the isothermal temperature under which crystallization occurred. A linear increase in induction time with increased temperature was found for both fibers and rosettes. A modified Avrami model was developed by introducing the volume fraction of each type of morphology into three dimensional and one dimensional full Avrami models. It was found that the experimental trends for mixed crystal morphologies could be captured by the modified Avrami model.

Due to the difficulty of obtaining samples with a single crystal morphology, rheological studies of suspensions containing mixtures of the three morphologies in a surfactant solution have been undertaken. The viscometry of dilute suspensions has shown that the magnitude of intrinsic viscosity is dominated by the fraction of a crystal morphology type, i.e. fiber > rosette > irregular crystal. A modified Farris model was fitted to the rheology data from mixtures of crystal morphology with interacting particles. A yield stress exists for concentrated suspensions followed by a shear thinning behavior with the increase of shear rate. A power-law relation has been found between yield stress and total particle volume fraction with a constant exponent of 1.5 regardless of crystal morphology.

Acknowledgements

I would like to express my sincere appreciation to my supervisor Dr. Andrew Hrymak who led me onto the right track and guided the overall progress of the project and thesis. I thank my supervisory committee members, Dr. Robert Pelton, Dr. Gianluigi Botton and Dr. Todd Hoare for their suggestions and help on my research work.

I thank the Natural Sciences and Engineering Research Council of Canada (NSERC) for their financial supports of my research work. I also thank Dr. Shaffiq Jaffer, Vincenzo Guida and Dr. Patrick Spicer from the Procter & Gamble Company for their insightful discussions. Additionally, I would like to thank Dr. Musa Kamal from Department of Chemical Engineering in McGill University to provide with Linkam Shear Stage and useful discussion. I would also like to thank Dr. Shiping Zhu to provide with ATS rheometer and Dr. Kari Dalnoki-Veress to provide with Linkam Hot Stage.

I will also extend my gratitude to research staffs in BIMR, Dr. Glynis de Silveira, Dr. Jim Britten, and Chris Butcher, for their training, help and suggestions on XRD, SEM and light microscopes. I would also thank Maria Reid in Electron Microscopy Facilities in Health Science Department for her training and help with TEM.

It is my great pleasure to study in the Polymer Processing Group and I would like to thank Elizabeth Takacs for trainings on DSC and rheometers, Dr. John Vlachopoulos and Dr. Michael Thompson for useful discussions on the rheology. Also, I would like to thank all the group members for their daily support either in the lab or office. We did have a good time studying together. In addition, I thank four outstanding summer students: Natalija Mirilovic, Stephanie Kedzior (University of Waterloo), Fadi Rishmawi and Nahreen Gorrges.

I also wish to give my special thanks to staffs in the Chemical Engineering Department: Kathy Goodram, Lynn Falkiner and Melisa for their administrative assistance, and Doug Keller, Paul Gatt, Justyna Derkach and Dan Wright for their technical support.

Finally, I wish to thank my family for their love and understanding.

Preface

This is a sandwich type of thesis which is based on the following journal articles and submitted manuscripts:

- Yang, D**.**, Hrymak, A. N., Rheology of Aqueous Dispersions of Hydrogenated Castor Oil. **2012**, being developed for a journal submission.

- Yang, D., Hrymak, A. N., Kedzior, S., Kinetics of Isothermal Crystallization of Hydrogenated Castor Oil-in-Water Emulsions. **2012**, submitted to *J. Am. Oil Chem. Soc*.

- Yang, D., Hrymak, A. N., Kamal, M. R., Crystal Morphology of Hydrogenated Castor Oil in the Crystallization of Oil-in-Water Emulsions: Part 2. Effect of Shear. *Ind. Eng. Chem. Res*. **2011**, 50(20), 11594-11600.

- Yang, D., Hrymak, A. N., Crystal Morphology of Hydrogenated Castor Oil in the Crystallization of Oil-in-Water Emulsions: Part 1. Effect of Temperature. *Ind. Eng. Chem. Res*. **2011,** 50(20), 11585-11593.

TABLE OF CONTENTS

Abbreviation

DIC	differential inference contrast
DSC	differential scanning calorimetry
HCO	hydrogenated castor oil
HLAS	linear alkylbenzen sulfonate acid
NaLAS	sodium linear alkylbenzen sulfonate
NMR	nuclear magnetic resonance
PLM	polarized light microscope
SEM	scanning electron microscope
TAG	triacylglycerol
TEM	transmitted electron microscope
XRD	x-ray diffraction

Chapter 1 Introduction

Rheology modifiers have been developed for decades and widely used in paints (Magauran 1994), cosmetics (Floyd et al.1982), ceramics (Pabst et al. 2006), food (Marangoni and Narine 2002) and household products. Rheology modifiers play the role of thickening agents and phase stabilizers. The microstructure of the rheology modifier, in its applicable matrix, plays the key role in determining the macro- physical and dynamic properties of products (Solomon and Spicer 2010). Therefore, the choice and manufacture of a suitable rheology modifier to structure the dispersing matrix becomes a key decision step for industrial applications.

1.1 Background Review

1.1.1 Hydrogenated Castor Oil (HCO)

Hydrogenated castor oil, a triacylglycerol (TAG), also called castor wax or tri-12-hydroxylstearin, is a water-insoluble wax-like powder or flake. It is prepared from castor oil through hydrogenation in the presence of a nickel catalyst (Sreenivasan et al. 1957). The detailed physical properties of HCO are shown in Table 1.1 and the molecular structure of pure tri-12-hydroxylstearin is shown in Figure 1.1.

Table 1.1 Physical properties of hydrogenated castor oil.

Boiling range/point (°C)	Melting point (°C)	Flash point (°C)	Solubility in water (kg/m^3)	Density at 25°C (kg/m^3)
>300	82-87	310	insoluble	990

HCO has many applications in paint, cosmetics and personal care products. Jones et al. (2002) used non-melting HCO powder as a component of a topical ointment to make it smoother in texture and more spreadable. HCO has also been embodied in laundering solutions as a fabric conditioning component (Brock, 1978). After laundering, the dried fabrics exhibited excellent softness and low static charge. However, the widest use of HCO is as a rheology modifier. Sommese (1995) applied HCO to stabilize the water-in-oil dispersion of water soluble vinyl polymer. The dispersion could be destabilized by shear but would recover soon after shear was removed. Magauran (1994) also incorporated HCO into paints as the rheological build component as well as enhancing the resistance of seeding.

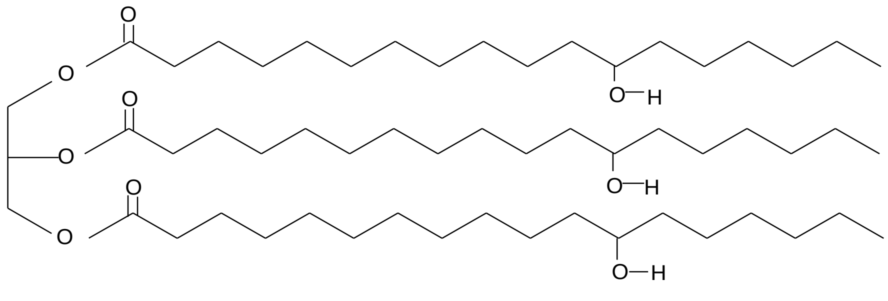

Figure 1.1 Molecular structure of hydrogenated castor oil.

1.1.2 Crystal Morphology

Crystallization of triacylglycerols has been extensively studied by Garti and Sato (2001), Hartel (2001), Marangoni and Narine (2002) and Windhab et al. (2009). Molecular structures of fats (Timms 1984, Grahame et al. 2011), phase of fats (i.e., melts, emulsions or microemulsions) (Dickinson et al. 1990, Kogan and Garti 2007), impurities (McClements et al. 1993, Kaneko et al. 1999) and processing conditions (Herrera and Hartel 2000) all affect the crystallization kinetics and observed crystal morphology, which then further affect the rheological (Thareja et al. 2011) and mechanical (Kloek 1998) properties of products.

Thermodynamics and kinetics

The difference in chemical potentials between liquid and solid phases is the thermodynamic driving force for the crystallization. This thermodynamic driving force can be modeled by either supersaturation or supercooling depending on the availability of parameters of materials (Narine 2002). Nucleation is the early stage of the formation of solid phases and then followed by the crystal growth. Gibbs free energy as the unit chemical potential of the material system (e.g. solutions or melts) is minimized during the nucleation, and a classic expression for Gibbs free energy of homogeneous nucleation is shown as

$$\Delta G_{\mathrm{hom}} = -\Delta G_V V + \Delta G_S S = -\frac{4}{3}\pi r^3 \Delta G_V + 4\pi r^2 \sigma \qquad (1.1)$$

where V, S and r are the volume, surface and radius of molecular clusters; σ is the surface free energy. Equation 1.1 describes the changes of Gibbs free energy caused by the free energy per volume (or enthalpy of fusion) and the surface energy due to the surface tension. Gibbs free energy decreases until a critical nuclei size is reached, and then with growth the nuclei become increasingly stable. This critical value of free energy, the activation free energy ($-\Delta G^{*}_{\hom}$), of nucleation was calculated as a function of supersaturation or supercooling (Narine 2002). As it is generally assumed that the size distribution of nuclei clusters follow a Boltzmann distribution, the homogeneous nucleation rate considering both activation free energy and diffusion barrier ($-\Delta G^{*}_{diff}$) is expressed as

$$J_{\hom} = \frac{N_A kT}{h} \exp\left(\frac{-\Delta G^{*}_{\hom}}{kT}\right) \exp\left(\frac{-\Delta G^{*}_{diff}}{kT}\right) \tag{1.2}$$

where *N* is Avogadro number; *k* is Boltzmann constant, *h* is Planck constant; *T* is absolute temperature. However, in real processing heterogeneous nucleation happens as well due to the existence of impurities, such as dusts, surfactants (McClements et al. 1993), mono- or diglycerides (Wright et al. 2000), wall and impellers of the crystallizer and so on. The activation free energy for heterogeneous nucleation ($-\Delta G^{*}_{het}$) is lower than that of homogeneous nucleation, and the two can be related as $\Delta G^{*}_{het} = \Delta G^{*}_{\hom} f(\theta)$ which is attributed to the contact angle (θ) of melt onto the solid heterogeneous phase.

The induction time, τ_{ind}, which is the time used for nuclei to reach their critical crystal sizes is another parameter used to reflect the nucleation rate (Myerson 2002). The induction time is inversely proportional to the nucleation rate. Therefore, the nucleation rate can be calculated by experimental obtaining the induction time (Toro-Vazquez et al.

2002).

The growth rate of nuclei is controlled by mass and heat transfer from the environment to the growing surface and the attachment of growth unit onto the right crystal lattices (Mullin 2001). The latter, the surface attachment, is usually considered as the rate controlling step (Garti and Sato 2001). One can test it by comparing the melting rate (mass and heat transfer controlled) and the growth rate. If the melting rate is much faster than the growth rate, the surface attachment kinetics dominates and vice versa.

The relative growth rate of every crystal surfaces decides the crystal morphology, and an equilibrium shape forms when the surface free energy of all faces is minimized. Fat crystal morphology could be different for different polymorphs (Garti and Sato 2001). It could be also different even for the same polymorph at different processing conditions (Kellens et al. 1992). The traditional theory of predicting the crystal morphology is Bravais-Friedel-Donnay-Harker (BFDH) theory (Mullin 2001), which assumes the growth rate of each crystal face is proportional to its surface energy. Another theory (Hartman-Perdok theory) especially used for modeling TAG systems was developed by Hartman and Bennema (1980, 1995) by employing attachment energy as the growth-controlling parameter. The attachment free energy equals the energy loss if cutting the crystal along its crystallographic orientation. The needle-like growth morphology of TAGs was well predicted by computer simulation method (Meekes et al. 2003) using the Hartman-Perdok (HP) theory. Thus, the growth rate of commonly seen spherulites which are considered as aggregate of radially growing crystalline needles can be predicted (Hollander et al. 2002). However, there is still much to understand to extend the crystal growth theories into various and multi-component fat systems.

A sigmoidal shaped curve for TAG crystallization kinetics is normally shown, which is the consequence of nucleation, growth and impingement. A deterministic model for overall crystallization kinetics was derived by Avrami (1939) first used in metal systems and then extended to other systems including TAGs. Due to the simple expression, the Avrami model is widely used to estimate the overall crystallization kinetics. The simplified Avrami equation is shown below:

$$X = 1 - \exp(-kt^{n}) \tag{1.3}$$

where X is the degree of crystallization; k and n are fitting parameters.

A variety of techniques are available for the measurements of kinetics, such as: differential scanning calorimetry (DSC) (Foubert et al. 2003, MacNaughtan et al. 2006), polarized light microscopy (PLM) (Wright et al. 2000), ultrasound (Povey 1995), turbidimetry (Wright et al. 2000), pulsed nuclear magnetic resonance (NMR) (Kloek et al. 2000), x-ray diffraction (XRD) (Mazzanti et al. 2009) and viscometry (de Graef 2006, Thareja et al. 2011). However, no one technique works on all material systems. For example, polarized light microscopy (Martini and Herrera 2002) was reported to be the most sensitive to detect nucleation but it was limited by its resolution. Turbidimetry is often limited by the concentration of crystals suspended.

Processing conditions

Cooling and shear are the two most important processing conditions for TAG crystallization. Narine and Marangoni (2002) investigated the effect of cooling rate (from 0.1°C/min to 5°C/min) on nucleation and crystal morphology of milk fat and lard-in-water systems. The results showed that upon slow cooling, there were low solid fat content and crystal sizes were usually large but the polymorphism was always stable. When fast cooling is applied, higher values of the Avrami constant and lower exponential index were obtained, and the crystals were always smaller. Cooling rates over a larger range from 0.1 to 20°C/min were used and nucleation was investigated by Humphrey and Narine (2007). Differential scanning calorimetry (DSC) results showed that the onset of crystallization temperatures decreased with the increasing of cooling rate as well as induction time. The explanation for this phenomenon was that fast cooling increased the viscosity of emulsions and subsequently increased the resistance to heat transfer.

Herrera et al. (1996) investigated the effects of crystallization temperature, and suggested that induction time is higher at higher crystallization temperature and higher cooling rate. Also, the addition of surfactants prolonged the induction time and delayed the nucleation. Hindle et al. (2000) employed the curve-fitting method (Kloek, 1998) to investigate the effect of crystallization temperature on the nucleation. It was found that the maximum solid fat content increased with the lowering of crystallization temperature, which showed more crystals at higher supercooling.

Sonwai and Mackley (2006) did a systematic study on the effect of shear on the crystallization kinetics and crystal morphology of cocoa butter in the shear rate range of 50 s^{-1} to 1500 s^{-1}. Integrated x-ray intensity results, which represent the crystallized solid content, showed that an increase in shear rate induced the transformation of polymorphism of cocoa butter from an unstable form to a preferred stable form and resulted in early nucleation. Sonwai and Mackley (2006) stated that without shear, spheroid crystals appeared. Under gentle shear, the crystal size increased attributed to two reasons (Grall and Hartel, 1992). First, the gentle collision between crystals may provide broken surfaces to make fat molecules much easier to pack into the crystals. Second, gentle shear can optimize the heat transfer on the crystal surface by efficiently removing heat released during crystal growth process. When the shear rate reached 100 s^{-1}, the crystal size decreased and the number of crystals increased. This is because high shear rate produces more crystals, which induce secondary nucleation. Also, under high shear rate, crystals aggregated together to form a solid mass, because shear increased the probability of collision of particles and subsequent van der Waals attraction force effects.

Summary

The crystal morphology of TAGs is usually controlled and modified by controlling the material systems and processing conditions. Sometimes, a desired nucleation and polymorph can also be controlled by adding well characterized foreign nuclei (Takiguchi et al. 1998). Secondary nucleation (Mullin 2001) and granulation (Reynolds et al. 2005) are also useful for designing demanding shapes of crystals. Although a common phenomenon in TAGs, spherulitic growth is not well understood and studies on the roles of surface attachment control and transportation control are still continuing.

1.1.3 Rheology Modifier

Braun and Rosen (2000) defined rheology modifier as “a material that alters the rheology of a fluid composition to which it is added”. The rheology modifier plays important roles in achieving desirable flow behaviour and microstructure of the products. Examples of products required rheological modification by additives are paints, food, cosmetics and pharmaceuticals. Many rheology modifiers are used, such as microcrystalline cellulose, biopolymers like gellan gum, silica, acrylic polymers, and organic clays and so on (Koleske 1995). In foods, rheology modifiers can be diary milk fiber powders dispersed into melt chocolate (Marti, 2004). In pharmaceuticals, silica is used in topical therapeutic cream. In personal care products, acrylic polymers are used as thickeners in toothpaste. Gellan gum is also attracting increasing interest due to its forming thermoreversible gels (Caggioni et al. 2007) utilized in miscellaneous household products.

Many factors influence the choice of rheology modifier, such as shape, size, charge, medium and processing conditions and so on (Mewis and Wagner, 2009). Figure 1.3 shows the viscosity profile of a typical architectural coating for different coating processes at varying shear rates. The modifier(s) must provide a relative higher viscosity to level the paint, but also a lower viscosity for brush coating (Koleske 1995).

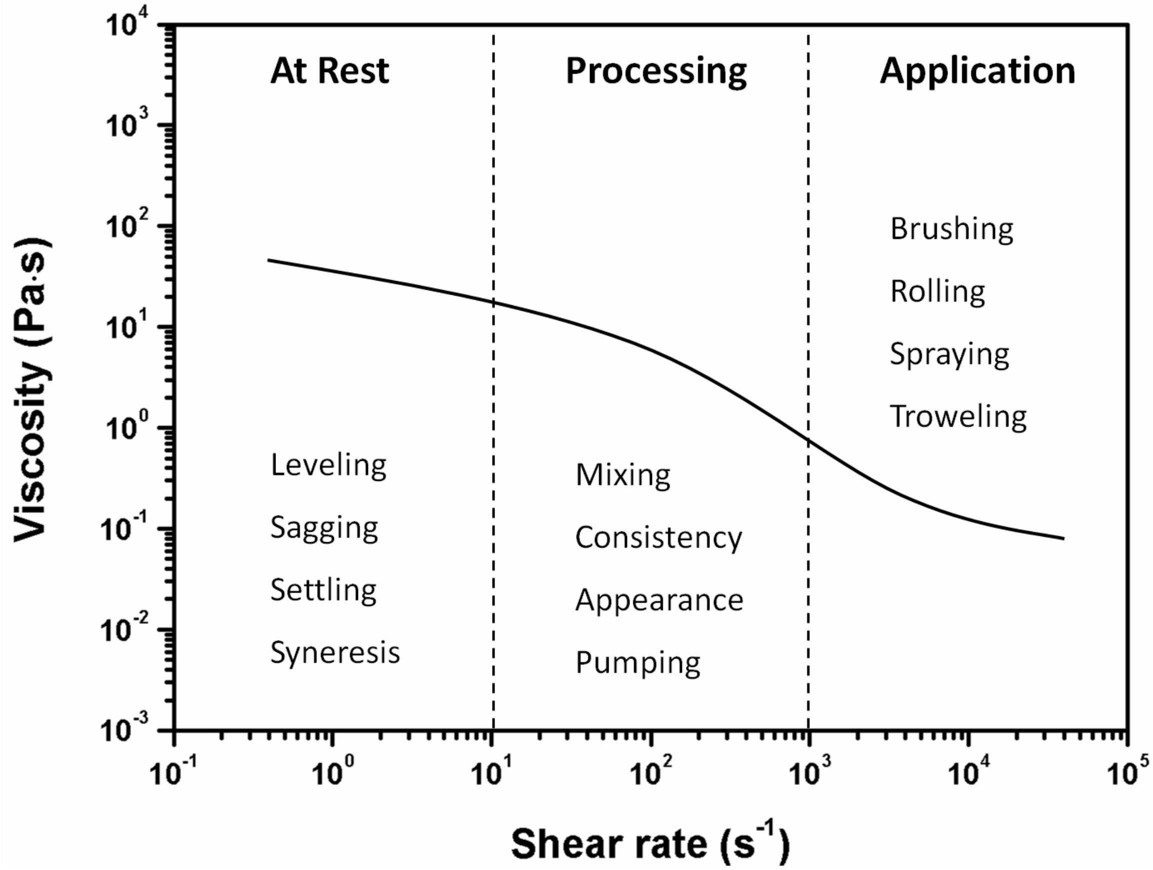

Figure 1.3. A typical architectural coating viscosity profile with three important shear rate ranges for application purpose (Koleske 1995).

The rheology modifier added could be a solid, liquid or gas. During the past decades, the rheology of suspensions has been studied systematically and reviews can refer to Mewis (1994), Mewis and Wagner (2009), Russel (1989) and Wierenga and Philipse (1998). Rheology of suspensions is usually influenced by microstructural changes caused by fluid/particle or particle/particle interactions or both. For dilute dispersions, hydrodynamic effects and Brownian forces at low shear will dominate the rheological behaviour. However, with increasing concentration of particles, particulate interactions become more important, such as colloidal forces (Russel 1989), steric effects, and van der Waals attraction.

The concentration regime of particulate suspensions can be divided into *dilute*, *semi-dilute*, *concentrated* and *nematic* (Doi and Edwards 1986) as shown in Figure 1.4. In dilute solution, the particle volume concentration (v) is low enough that particles can rotate freely and the distances between particles are much larger than the length of particles. In a semi-dilute solution, particles are considered as mathematical lines without thickness but cannot translate or rotate easily. In concentrated solutions, the thickness of particles cannot be neglected. Therefore, the difference is that for semi-dilute solutions the interaction between particles can be neglected in the static properties such as thickness of the particles. But in concentrated situations, both static and dynamic properties (i.e. shear viscosity, shear modulus) cannot be neglected. In this research, we are interested in the dynamic properties of suspensions and also particle thickness (i.e., fibers) is very important, so the semi-dilute and concentrated regimes are studied together. At still higher concentrations, an anisotropic nematic state forms due to the excluded volume interaction as shown in Figure 1.4(d).

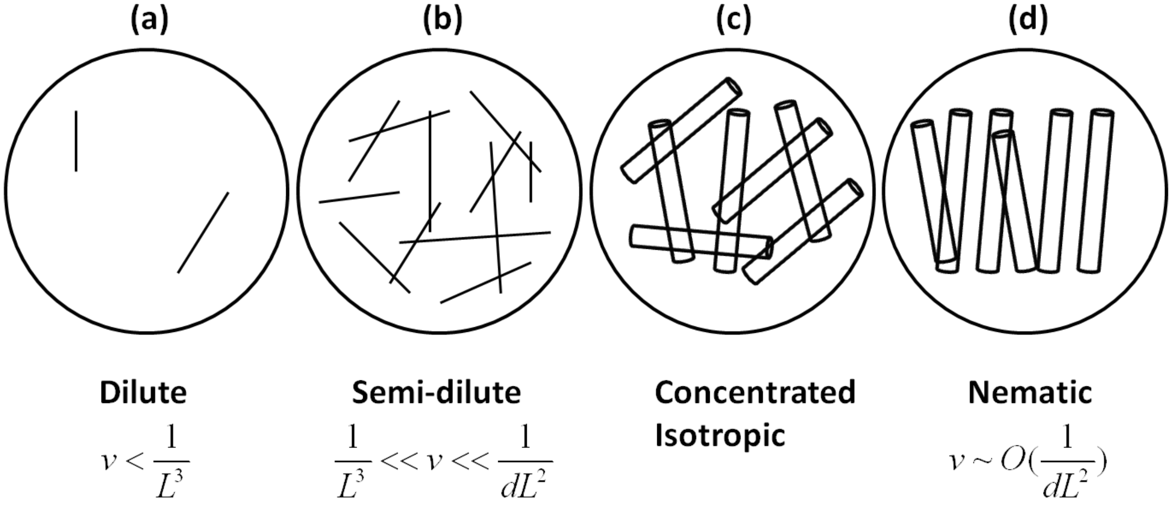

Figure 1.4 Concentration regimes of rodlike suspensions. (a) dilute; (b) semi-dilute; (c) concentrated; (d) nematic. (Doi and Edwards 1986).

Dilute dispersions

Theories of suspension rheology of dilute dispersions are well understood (Mewis and Macosko 1994). For dilute suspensions, the shear viscosity η of a material which is defined as the ratio of shear stress σ and shear rate $\dot{\gamma}$ can be expressed as follows:

$$\eta = \mu(1+[\eta]\phi + k_H[\eta]^2\phi^2 + ...) \tag{1.4}$$

where μ is the viscosity of the media; ϕ is the particulate volume fraction; k_H is the Huggins coefficient which reflects the particle/particle interactions; $[\eta]$ is the intrinsic viscosity which stands by the average contribution of particles to the shear viscosity and is expressed as:

$$[\eta] = \lim_{\phi \to 0} \frac{\eta - \mu}{\mu\phi} \tag{1.5}$$

Einstein in 1911 suggested an intrinsic viscosity of 2.5 for hard spheres. Batchelor (1977) obtained a magnitude of 6.2 for the coefficient of the ϕ^2 term at low shear limit and suggested that the intrinsic viscosity and Huggins coefficient will both increase for anisotropic particle suspensions. Jeffery (1922) calculated intrinsic viscosity for anisometric particles as a function of aspect ratio. Brenner (1974) published the most comprehensive and precise expression relating intrinsic viscosity to particle aspect ratio r and the Peclet number Pe. When loading shear on the dilute suspension, the motion of the particles are determined by the shear stress and Brownian motion, especially rotary Brownian motion. Rotary Peclet number is defined as the ratio between shear rate $\dot{\gamma}$ and rotational diffusivity D_r which can be obtained everywhere (Brenner 1967 and 1974):

$$Pe = \frac{\dot{\gamma}}{D_r} \tag{1.6}$$

In comparison with hard spheres, an additional orientation effect exists for axisymmetric particles. In dilute dispersions, hydrodynamic forces tend to align particles in the flow direction, while Brownian motion tends to randomize the particulate orientation. As Brownian motion is a decreasing function of particle size, if both shear forces and particle size are small, the rotary Peclet number will approach zero. Otherwise, high shear rate and large particle will give $Pe \to \infty$.

An orientation distribution function for dilute dispersions was well developed and applied to many types of axisymmetric particles by Goldsmith and Mason (1967), Hinch and Leal (1972), Brenner (1974) among others. Jeffery (1922) found the periodic rotation of non-Brownian axisymmetric particles under shear flow and the rotation was termed the

Jeffery orbit. Goldsmith and Mason (1967) used visualization methods to study the non-Brownian rodlike particulate dispersions and directly observed the periodic rotation of particles. The period is a function of shear rate and aspect ratio for rodlike particles.

Concentrated dispersions

When the concentration of particles is beyond the dilute regime, particles cannot move or rotate freely without being impeded by other particles. In the semi-dilute Brownian suspension, Doi and Edwards (1978) developed a *cage model* to predict the rotary diffusivity of rods. The *cage model* assumes rods mainly diffuse along their own contour, and when the rod leaves its tube-like confinement its orientation can only change by a little angle. Marrucci (1985) extended the Doi-Edwards theory into polydispersed rod suspensions, and found that long rods could escape from the “cage” more quickly when shorter rods moved to dissolve the “cage”.

For semi-dilute non-Brownian suspension, hydrodynamic interactions between particles become dominant. Batchelor (1971) developed a *hydrodynamic screening model* to predict the viscous drag coefficient. Shaqfeh and Fredrickson (1990) modified Batchelor’s model (1971) by considering multiparticle hydrodynamic interactions of slender bodies. Hinch and Leal (1973) and Stover et al. (1992) used simulation and experimental results respectively to explain the orientation distribution of fibers in semi-dilute dispersions under steady shear flow. As Brownian motion could be neglected, weak hydrodynamic interactions would be enough to imbalance the *Jeffery orbit* to create a steady state flow.

A critical concentration called *maximum packing fraction* ($\phi_{\max}$) exists in the case where the suspension is too viscous to flow. Krieger (1972) developed a semi-empirical equation containing both maximum packing fraction and intrinsic viscosity as shown:

$$\eta_r = (1 - \frac{\phi}{\phi_{\max}})^{-[\eta]\phi_{\max}} \tag{1.7}$$

The Krieger model was used widely for any aspect ratio (Wierenga, 1998). $\phi_{\max}$ can be fitted from experimental data for equation 1.7 and has been reported to be a function of aspect ratio by Kitano et al. (1981).

Dynamic modulus

Linear viscoelasticity of particle dispersions has been extensively studied by Shikata and Pearson (1994) and de Kruif et al. (1989). Storage (G’) and loss (G”) modulus are considered as a function of reduced frequency: $a_T \omega \tau_\omega$. a_T is the shift factor used to collapse modulus data from different temperatures onto one curve. ω is the frequency and τ_ω is the longest relaxation time. Relaxation time is inversely proportional to particle diffusivity and proportional to the volume fraction. This is because closely packed particles relax slowly back to their original interparticle spacing. Shikata and Pearson (1994) investigated spherical silica particles with diameters of 60 nm and found viscous properties dominate elastic properties for a volume fraction between 0.30 and 0.55. With increased volume fraction, G’ and G” will shift to lower frequencies and higher moduli.

At high frequency, the particles move much faster between each other than relaxation by Brownian motion. A high frequency viscosity ($\eta_\infty(\phi) = \lim_{\omega\to\infty} G''/\omega$) is used to characterize the viscoelastic behavior at high frequency, so $\eta_\infty(\phi)$ is higher at higher volume fraction. The theoretical relationship between $\eta_\infty(\phi)$ and ϕ was studied by Beenakker (1984) and then extended by Shikata and Pearson (1994).

Summary

Stable particulate suspensions exhibit diverse rheological behaviors depending on the particle size, shape, volume fraction, charge, as well as the property of medium. Shear thinning and shear thickening (Wagner and Brady 2009, Cheng et al. 2011) for dilute dispersions of hard spheres are well studied. However, investigations for suspensions with high concentrations are not completely understood in both experimental and simulation (Michailidou et al. 2009) aspects. Nonspherical particles, e.g. rods, show shear thinning even at infinite dilute dispersion due to the orientation effects of such particles. But the observed large normal stress difference for non-Brownian rod dispersions has not been well understood. In addition to linear viscoelasticity effects of particle dispersions, recent suspension rheology studies on large amplitude oscillatory shear (LAOS) (McMullan and Wagner 2009) are of great interest to researchers.

1.2 Thesis Objectives

The overall objective of my work in this thesis is to understand the effects of HCO crystal morphology as the desired rheology modifier and the process conditions by which to achieve the preferred crystal morphology. In this thesis, I am not going to target on a specific application but a general understanding of the crystal morphology on the function of the rheology modifier. Chapters 2-4 investigate crystallization process conditions and chapter 5 is about the rheological characterization of the HCO solution. The specific objectives of this research are:

1. *Effect of the temperature history on the crystal morphology.* A study how cooling as a function of time influences the proportion of the three observed crystal morphologies: fiber, rosette and irregular crystal.

2. *Effect of the shear history on the crystal morphology.* A study how the shear rate and time influence the proportion of fiber, rosette and irregular crystal.

3. *Kinetics of isothermal crystallization.* An investigation of the kinetics of isothermal crystallization and a modified Avrami model.

4. *Relationship between rheology and morphology.* An investigation of the effects of crystal morphology and microstructure on the rheology of HCO aqueous dispersions.

1.3 Layout of the Thesis

Chapter 1: The research background of this thesis is summarized in this chapter, including the introduction of the material system, influencing factors of fat crystal morphology, and recent progress in rheology modifiers. The specific objectives and an outline of the thesis are also presented here.

Chapter 2: This chapter describes the observation of HCO crystal morphology, and the variation of crystal morphology at isothermal and non-isothermal cooling histories. The thermodynamic parameters of rosettes and fibers are calculated and related to different nucleation mechanisms.

Chapter 3: This chapter states the effect of shear history on the emulsification of oil-in-water emulsion, nucleation and crystal morphology.

Chapter 4: This chapter describes the kinetics of isothermal crystallization, including nucleation, growth and overall crystallization rate. The overall crystallization rate was captured by both experiments and models.

Chapter 5: This chapter illustrates the rheology of HCO particulate suspensions affected by different crystal morphology. A correlation between the relative viscosity and morphology at dilute situation was developed.

Chapter 6 This chapter summarizes the main conclusions and contributions of this project.

1.4 References

Avrami M, (1939) Kinetics of phase change, 1. General theory. J Chem Phys 7:

1103-1112.

Batchelor GK, (1971) The stress generated in a non-dilute suspension of elongated particles by pure straining motion. J Fluid Mech 46: 813-829.

Batchelor GK, (1977) The effect of Brownian motion on the bulk stress in a suspension of spherical particles. J Fluid Mech 83: 97-117.

Beenakker CWJ, (1984) The effective viscosity of a concentrated suspensions of spheres. Physica A 128: 48-81.

Braun DB, Rosen MR, (2000) Rheology Modifier Handbook. William Andrew Publishing, NY, USA.

Brenner H, (1967) Coupling between the translational and rotational Brownian motions of rigid particles of arbitrary shape. J Colloid Int Sci 23: 407-436.

Brenner H, (1974) Rheology of a dilute suspension of axisymmetric Brownian particles. Int J Multiphase Flow 1: 195-341.

Brock JF, Schilling KJ, (1978) Fabric conditioning compositions. U.S. Patent 4,096,072, The Procter & Gamble Co., Cincinnati, OH, USA.

Caggioni M, (2007) Rheology and microrheology of a microstructured fluid: The gellan gum case. J Rheol 51: 851-865.

Cheng X, McCoy JH, Israelachvili JN, Cohen I, (2011) Imaging the microscopic structure of shear thinning and thickening colloidal suspensions. Science 333: 1276-1279.

de Graef V, Dewettinck K, Verbeken D, Foubert I, (2006) Rheological behavior of crystallizing palm oil. Eur J Lipid Sci Technol 108: 864-870.

de Kruif CG, van Iersel EMF, Vrij A, Russel WB, (1985) Hard sphere colloidal dispersions: viscosity as a function of shear rate and volume fraction. J Chem Phys 83: 4717-4725.

Dickinson E, Goller MI, McClements DJ, Peasgood S, Povey MJW, (1990) Ultrasonic monitoring of crystallization in an oil-in-water emulsion. J Chem Soc Faraday Trans 86: 1147-1148.

Doi M, Edwards SF, (1978) Dynamic of rod-like macromolecules in concentrated solution. J Chem Soc Faraday 2 74: 560-570.

Doi M, Edwards SF, (1986) Semidilute and concentrated solutions of rigid rodlike polymers. In: Doi M, Edwards SF (ed) The Theory of Polymer Dynamics, Clarendon Press, Oxford, pp: 324.

Erni P, Cramer C, Marti I, Windhab EJ, Fischer P, (2009) Continuous flow structuring of anisotropic biopolymer particles. Adv Colloid Int Sci 150: 16-26.

Foubert I, Vanrolleghem PA, Dewettinck K, (2003) A differential calorimetry method to determine the isothermal crystallization kinetics of cocoa butter. Therm Acta 400: 131-142.

Floyd DT, Murphy JH, Brodzinski JJ, (1982) Cosmetic pencil. U.S. Patent 4,334,546, Kolmar Laboratories Inc., Port Jervis, NY, USA.

Garti N, Sato K, (2001) Crystallization Processes in Fats and Lipid Systems. Marcel Dekker Inc., NY, USA.

Goldsmith HL, Mason SG, (1967) Microrheology of dispersions. In: Eirich FR (ed) Rheology, Vol. 4, Pergamon, NY, pp 85.

Grahame DAS, Olauson C, Lam RSH, Pedersen T, Borondics F, Abraham S, Weiss RG, Rogers MA, (2011) Influence of chirality on the modes of self-assembly of 12-hydroxystearic acid in molecular gels of mineral oil. Soft Matter 7: 7359-7365.

Grall DS, Hartel WR, (1992) Kinetics of butterfat crystallization. J Am Oil Chem Soc 69: 741-747.

Hartel RW, (2001) Crystallization in Foods. Food Engineering Series, Aspen Publishers, Inc., USA.

Hartman P, Bennema P, (1980) The attachment free energy as a habit controlling factor. J Cryst Growth 49: 145-156.

Herrera M, Hartel R, (2000) Effect of processing conditions on crystallization kinetics of a milk fat model system. J Am Oil Chem Soc 77: 1177-1188.

Herrera M, Rocha F, (1996) Effects of sucrose ester on the kinetics of polymorphic transition in hydrogenated sunflower oil, J Am Oil Chem Soc 73: 321-325.

Hinch EJ, Leal LG, (1972) The effect of Brownian motion on the rheological properties of a suspension of non-spherical particles. J Fluid Mech 52: 683-712.

Hinch EJ, Leal LG, (1973) Time-dependent shear flows of a suspension of particles with weak Brownian rotations. J Fluid Mech 57: 753-767.

Hindle S, (2000) Kinetics of crystallization in n-hexadecane and cocoa butter oil-in-water emulsions accounting for droplet collision-mediated nucleation. J Colloid Int Sci 232: 370–380.

Hollander F, Kaminski D, Duret D, van Enckevort W, Meekes H, Bennema P, (2002) Growth and morphology of thin fat crystals. Food Res International 35: 909-918.

Humphrey K, Narine S, (2007) Diminishing marginal utility of cooling rate increase on the crystallization behavior and physical properties of a lipid sample. J Am Oil Chem Soc 84:709–716.

Jeffery GB, (1922) The motion of ellipsoidal particles immersed in a viscous fluid. Proc R Soc Lond A 102: 161-179.

Jones DP, Hobson DW, Duque PP, (2002) Elegant hydrogenated castor oil ointment. U.S. Patent 6,479,060, Healthpoint Ltd., Fort Worth, TX, USA.

Kaneko N, Horie T, Ueno S, Yano J, Katsuragi T, Sato K, (1999) Impurity effects on crystallization rates of n-hexadecane in oil-in-water emulsions. J Cryst Growth 197: 263-270.

Kellens M, Meeussen W, Reynaers H, (1992) Study of polymorphism and the crystallization kinetics of tripalmitin: A microscopic approach. J Am Chem Oil Soc 69: 906-911.

Kitano T, Kataoka T, Shirota T, (1981) An empirical equation of the relative viscosity of polymer melts filled with various inorganic fillers. Rheol Acta 20: 207-209.

Kloek W, (1998). Mechanical properties of fats in relation to their crystallizatioin. PhD thesis, Landbouwuniversiteit Wageningen.

Kloek W, Walstra P, van Vliet T, (2000) Nucleation kinetics of emulsified triglyceride mixtures. J Am Oil Chem Soc 77: 643-652.

Kogan A, Garti N, (2007) Improved solubilization of carbamazepine and structural transitions in nonionic microemulsions upon aqueous phase dilution. J Colloid Int Sci 315: 637-647.

Koleske JV, (1995) Paint and coating testing manual: fourteenth edition of the Gardner-Sward handbook, ASTM manual series, PA, USA.

Krieger MI, (1972) Rheology of monodisperse lattices. Adv Colloid Int Sci 3: 111-136.

Liu X, Boek ES, Briels WJ, Bennema P, (1995) Prediction of crystal growth morphology based on structural analysis of the solid-fluid interface. Nature 374: 342-345.

Magauran ED, Reynolds W, DiCarlo L, Cody CA, Chiavoni A, El-Shoubary M, (1994) Rheological additive comprising derivatives of castor oil. U.S. Patent 5,340,390, Rheox Inc., Hightstown, NJ, USA.

MacNaughtan W, Farhat IA, Himawan C, Starov VM, Stapley AG.F, (2006) A differential scanning calorimetry study of the crystallization kinetics of tristearin-tripalmitin mixture. J Am Oil Chem Soc 83:1-9.

Marangoni AG, Narine S, (2002) Physical Properties of Lipids, Marcel Dekker, NY, USA.

Marrucci G, (1985) Relaxation by reptation and tube enlargement: A model for polydisperse polymers. J Polym Sci Polym Phys Ed 23: 159-177.

Marti I, (2004) Dairy fibre powders- processing and application as rheology modifiers in confectionery systems. PhD dissertation, ETH, Swiss.

Martini S, Herrera ML, (2002) Practical considerations in nucleation studies: The polarized light microscopy technique. J Am Oil Chem Soc 79: 411-412.

Mazzanti G., Marangoni AG, Idziak SHJ, (2009) Synchrotron study on crystallization kinetics of milk fat under shear flow. Food Res Int 42: 682-694.

McClements DJ, Dickinson E, Dungan SR, Kinsella JE, Ma JG, Povey MJW, (1993) Effect of emulsifier type on the crystallization kinetics of oil-in-water emulsions containing a mixture of solid and liquid droplets. J Colloid Inter Sci 160: 293-297.

McMullan JM, Wagner NJ, (2009) Directed self-assembly of suspensions by large amplitude oscillatory shear flow. J Rheol 53: 575-588.

Meekes H, Boerrigter S, Hollander F, Bennema P, (2003) Needle crystal morphology explained. Chem Eng Technol 26: 256-261.

Mewis J, Macosko CW, (1994) Suspension rheology. In: Macosko CW (ed) Rheology: Principle, Measurements, and Applications, VCH Publishers Inc., NY, pp 425-474.

Mewis J, Wagner NJ, (2009) Current trends in suspension rheology. J Non-Newtonian Fluid Mech 157: 147-150.

Michailidou VN, Petekidis G, Swan JW, Brady JF, (2009) Dynamics of concentrated hard-sphere colloids near a wall. Phys Rev Lett 102: 068302(1-4).

Mullin MJ, (2001) Crystallization. Oxford: Butter-worth-Heinemann.

Myerson AS, (2002) Handbook of Industrial Crystallization. Boston: Butter-worth -Heinemann.

Narine S, Marangoni AG, (2002) Effect of cooling rate on the structure and mechanical properties of milk fat and lard. Food Res Int 35: 971-981.

Pabst W, Gregorova E, Berthold C, (2006) Particle shape and suspension rheology of short-fiber systems. J Euro Ceram Soc 26: 149-160.

Povey MJW, (1995) Ultrasound studies of shelf-life and crystallization. In: Dickinson E (ed) New Physico-Chemical Techniques for the Characterization of Complex Food Systems, Chapman & Hall, London, pp 196-212.

Reynolds GK, Fu JS, Cheong YS, Hounslow MJ, Salman AD, (2005) Breakage in granulation: A review. Chem Eng Sci 60: 3969-3992.

Russel WB, Saville DA, Schowalter WR, (1989) Colloidal dispersions. Cambridge University Press, UK.

Shaqfeh ERG, Fredrickson GH, (1990) The hydrodynamic stress in a suspension of rods. Phys Fluid A 2: 7-24.

Shikata T, Pearson DS, (1994) Viscoelastic behavior of concentrated spherical suspensions. J Rheol 38: 601-616.

Solomon MJ, Spicer PT, (2010) Microstructural regimes of colloidal rod suspensions, gels, and glasses. Soft Matt 6: 1391-1400.

Sommese AG., Nagarajan R, (1995) Settling stabilization of polymer containing particle dispersions in oil. U.S. Patent 5,438,088, Nalco Chemical Company, Naperville, Ill, USA.

Sonwai S, Mackley MR, (2006) The effect of shear on the crystallization of cocoa butter. J Am Oil Chem Soc 83: 583-596.

Sreenivasan B, Kamath NR, Kane JG, (1957) Studies on castor oil. 2. Hydrogenation of castor oil. J Am Oil Chem Soc 34: 302-307.

Stover CA, Koch DL, Cohen C, (1992) Observation of fiber orientation in simple shear flow of semi-dilute suspensions. J Fluid Mech 238: 277-296.

Takiguchi H, Iida K, Ueno S, Yano J, Sato K, (1998) Heterogeneous nucleation of n-alcohol crystals from solution assisted by vapor-deposited thin films of fatty acids. J Cryst Growth 193: 641-647.

Thareja P, Street CB, Wagner NJ, Vethamuthu MS, Hermanson KD, Ananthapadmanabhan KP, (2011) Development of an in situ rheological method to characterize fatty acid crystallization in complex fluids. Colloid Surf A 338: 12-20.

Timms R, (1984) Phase behavior of fats and their mixtures. Prog Lipid Res 23: 1-38.

Toro-Vazquez J, Herrera-Coronado V, Dibildox-Alvarado E. Charo-Alonso M, Gomez-Aldapa C, (2002) Induction time of crystallization in vegetable oils, comparative measurements by differential scanning calorimetry and diffusive light scattering. J Food Sci 67: 1057-1065.

Wagner NJ, Brady JF, (2009) Shear thickening in colloidal dispersions. Phys Today 62: 27-32.

Wierenga AM, Philipse AP, (1998) Low-shear viscosity of isotropic dispersions of (Brownian) rods and fibres: a review of theory and experiments. Colloids Surf A 134: 355-372.

Wright AJ, Hartel RW, Narine SS, Marangoni AG, (2000) The effect of minor components on milk fat crystallization. J Am Oil Chem Soc 77: 463-475.

Wright AJ, Narine SS, Marangoni AG, (2000) Comparison of experimental techniques used in lipid crystallization studies. J Am Oil Chem Soc 12: 1239-1242.

Chapter 2 Crystal Morphology of Hydrogenated Castor Oil in the Crystallization of Oil-in-Water Emulsion: Part 1. Effect of Temperature

In this chapter, I performed all the experiments, characterization and manuscript preparation. Dr. Andrew Hrymak supervised this work and participated in the edits on the manuscript. The manuscript has been published in the journal *Industrial & Engineering Chemistry Research*.

Yang, D., Hrymak, A. N., Crystal Morphology of Hydrogenated Castor Oil in the Crystallization of Oil-in-Water Emulsions: Part 1. Effect of Temperature. *Ind. Eng. Chem. Res*. **2011,** 50(20), 11585-11593.

I&EC research
Industrial & Engineering Chemistry Research

ARTICLE

pubs.acs.org/IECR

Crystal Morphology of Hydrogenated Castor Oil in the Crystallization of Oil-in-Water Emulsions: Part I. Effect of Temperature

Dingzheng Yang[†] and Andrew N. Hrymak[*,‡]

[†]Department of Chemical Engineering, McMaster University, Hamilton, Ontario L8S4L7, Canada

[‡]Department of Chemical and Biochemical Engineering, University of Western Ontario, London, Ontario, N6A 5B9, Canada

ABSTRACT: Crystallization of hydrogenated castor oil-in-water emulsions has been studied by polarized light microscopy, scanning electron microscopy, X-ray powder diffraction, and differential scanning calorimetry. Three types of crystal morphologies have been observed: rosettes, fibers, and irregular crystals. The energy barrier to nucleation for fibers is suggested to be higher than that of rosettes. Irregular crystals are thermodynamically less stable and tend to transform into stable polymorphs. Under isothermal crystallization at a temperature of 70 °C, mainly rosettes are observed. With an increase of supercooling, by decreasing the temperature to 55 °C, more fibers form due to a lower energy barrier to nucleation. If the crystallization temperature is set to 45 °C, irregular crystals form first and then transform into rosettes. A nonisothermal crystallization study shows that at a cooling rate of 1 °C/min, more rosettes and fibers are produced compared to a higher cooling rate of 5 °C/min, which produces more irregular crystals.

1. INTRODUCTION

Suspensions of hydrogenated castor oil (HCO) crystals are encountered in industrial processing of intermediates to produce rheological modifiers for a variety of products.[1,2] Paint[3] and shampoos[4] are examples of industrial applications of HCO suspensions used as a rheological modifier. HCO modified products show shear thinning and thixotropic behavior. Crystal morphology is one of the most important factors that influence the suspension rheology[1] and significantly depends on the nucleation and relative growth rate of the crystals in every direction. The growth directions will follow the crystallographic orientations most likely to grow depending on the thermodynamic and kinetic factors.[5,6] Polymorphism is a common phenomenon for most substances[7] and also appears in the HCO system. However, HCO crystal morphology studies have been rarely reported.[8]

Cooling history plays a key effect on the crystallization of oil-in-water emulsions.[9−11] It is generally suggested that less thermally stable structures form under fast cooling and more stable structures form under slow cooling.[12] Lopez et al.[13] studied the crystallization of milk fat in water emulsions and concluded that at a slow cooling rate (0.5 °C/min) more spherulitic crystals were observed, while at a fast cooling rate (>1000 °C/min) more needles were obtained. It is also suggested that the faster the cooling rate the smaller the crystals and the less influence of the interface on crystal morphology.

In this work, the mechanism of the formation of the HCO crystal morphologies will be studied, and the variation of crystal morphology dependence on the cooling history (isothermal and nonisothermal) will be elucidated.

2. MATERIALS AND METHODS

2.1. Materials. Hydrogenated castor oil (BP Chemicals Ltd.) has as its major component tri-12-hydroxystearin. HCO as used is supplied in a white flake form. The surfactant, linear alkylbenzene sulfonate acid (HLAS) was diluted by distilled water and neutralized with sodium hydroxide solution to pH = 7.5 ± 0.5 to form sodium linear alkylbenzene sulfonate (NaLAS). The concentration of NaLAS is 16.7 wt %. The method of preparing the surfactant is similar to that used in industrial applications.[4]

2.2. Preparation of Oil-in-Water Emulsions. HCO-in-water emulsions were prepared as follows: (i) 4 wt % HCO was added into 96 wt % NaLAS solution; (ii) the above mixture was melted in a 250 mL round-bottom flask at 92 °C[4,8] in an oil bath and then stirred with a mechanical stirrer at 300 rpm to disperse the oil phase into water by mediation of surfactant; (iii) after holding 5 min to remove the crystal memory, the emulsion was cooled in the oil bath under 300 rpm mechanical agitation until the temperature of the final crystal suspension reached room temperature. The crystal suspension was stored at room temperature and remained stable for more than a month. The HCO suspension can be easily withdrawn with a pipet and remelted to form emulsions. On the basis of microscopic observation, flocculation might happen before crystallization but coalescence rarely occurred.

2.3. Polarized Light Microscopy (PLM). A polarized light microscope (Olympus, Japan) with reflected cross polarized light was used for crystal morphology observation under a 20× objective lens using a Linkam Hot Stage TM94 (Linkam Scientific, Surrey, U.K.) to quantify the effects on crystallization due to heating and cooling of oil-in-water emulsions. The two polarizers were not perpendicular in order to obtain more surrounding information, which is beneficial for the analysis of morphology and size. Differential interference contrast (DIC) was used to increase the contrast between the crystals and the background. A sealed sample cell comprised of a round cover glass with a thickness

Received: December 30, 2010
Accepted: September 12, 2011
Revised: August 28, 2011
Published: September 12, 2011

ACS Publications © 2011 American Chemical Society

dx.doi.org/10.1021/ie1025985 | *Ind. Eng. Chem. Res.* 2011, 50, 11585–11593

of 0.17 mm and diameter of 18 mm (Fisher Scientific, Canada), a silicon wafer (University Wafer), and a stainless supporting ring with a height of 0.5 mm used as spacer created a sample cell to load emulsions. The sample cell was sealed using high vacuum silicon grease (Dow Corning) avoiding contact between the emulsion samples and the grease. A digital camera was used to take pictures during the crystallization process. ImageJ (NIH) was used for image analysis. Crystal number and sizes were measured manually. Three experiments were performed, and the average and standard deviation of the measured variable were calculated for statistical purposes.

2.4. Scanning Electron Microscopy (SEM). A field emission scanning electron microscope (JEOL JSM-7000F, JEOL) was used to obtain the crystal morphology. A drop of HCO crystal suspension was loaded on an aluminum sample holder and dried before introduction into the microscope chamber. A lower voltage of 2.0 kV was used to avoid destruction of the crystals.

2.5. X-ray Powder Diffraction (XRD). X-ray powder diffraction measurements were performed using a Rigaku RU-200 Cu (wavelength of radiation source λ = 1.5498 Å) generator, a Bruker 2-circle D8 goniometer, and a two-dimensional Bruker SMART 6000 CCD detector positioned 30 cm from the sample. Emulsified samples (prior to crystallization) were sandwiched between two Mylar polyester films (DuPont) with a stainless steel ring supporting the two films. Silicon grease was used for sealing. The emulsified samples were introduced into the Linkam Hot Stage TM94 (Linkam Scientific, Surrey, U.K.) to complete the crystallization under a given isothermal temperature and then transferred immediately into the X-ray facility, where a 300 s scanning time was used for each sample. Because of the short transfer time, changes in crystal structure were considered negligible; the 2θ angle varied from 1° to 24°. Preferred orientation effects were neglected assuming that orientations of aqueous suspended HCO particles were randomly distributed. A sample with the surfactant sandwiched by two Mylar sheets was used to create the background signal. The powder XRD patterns were obtained by background signal subtraction.

2.6. Differential Scanning Calorimetry (DSC). A TA Q200 differential scanning calorimeter (TA Instrument, New Castle, DE) was used to characterize the thermal behavior during the crystallization of emulsions and melting of HCO crystals. Prior to use, indium (T_{on} = 155 °C) and n-hexatriacontane (T_{on} = 76.1 °C) were used for temperature calibration. The heat flow due to phase changes was calibrated by pure indium. An empty hermetical aluminum pan covered with a lid was used for baseline calibration. Approximately 5−10 mg samples were introduced into the DSC hermetically sealed aluminum pans. The samples were first heated to 92 °C[4,8] at the rate of 10 °C/min and held for 5 min to erase the crystal memory before cooling. After application of different temperature time profiles (shown in section 2.7), the crystals were heated to 92 °C again at the rate of 10 °C/min to obtain the melting curves of crystals formed under various cooling histories.

The onset temperature of crystallization, T_{on}, was obtained by DSC[14] from the tangent point of the exothermic peak and baseline and microscopy observation of the appearance of the first HCO crystal. The difference between the two methods was less than 2 °C. The induction time (τ) of isothermal crystallization was the time period between the onset of crystallization and the time to reach the target isothermal temperature. The induction time of nonisothermal crystallization was the difference in time from the start of crystallization to the time to reach the melting point from the initial holding temperature (normally above the melting point).[15] The melting points for the observed polymorphs are different as shown by DSC data in section 3.3.1. However, the difference in melting points among different polymorphs is relatively small (<4 °C), thus a mixture of polymorphs is normally obtained. Therefore, the highest melting point of 84 °C is used to simplify the estimation of the induction time.

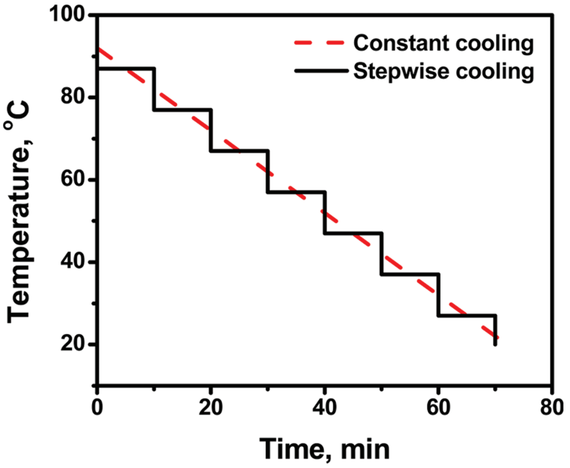

Figure 1. Temperature−time profiles for 1 °C/min constant cooling (dashed line) and 10 °C stepwise cooling (solid line) from 92 to 20 °C.

2.7. Temperature−time Profiles for Crystallization. The HCO-in-water emulsions were cooled to a specified target temperature T_c (i.e., 70, 55, 45 °C) and held for 80 min. The cooling rates used to reach the isothermal temperatures T_c were 40, 10, and 1 °C/min. Only the 40 °C/min cooling rate was fast enough to reach the isothermal temperature before any significant change in the sample, which was considered as nearly isothermal crystallization.

Three constant cooling rates (1, 2, and 5 °C/min) were used to cool HCO-in-water emulsions from 92 to 20 °C. For each cooling rate, stepwise cooling with two different temperature step sizes (10 and 5 °C) was applied for emulsion crystallization. Temperature time profiles were steps composed of a sharp temperature drop and isothermal hold as shown in Figure 1. In order to make a better comparison between constant rate cooling and stepwise cooling, the temperature time profile of the former always goes through the center points of both a sharp temperature drop and isothermal hold of the profile of stepwise cooling.

3. RESULTS AND DISCUSSION

3.1. Crystal Morphologies of Hydrogenated Castor Oil. Three types of HCO crystal morphologies have been observed: rosette, fiber, and irregular crystal. Micrographs of the three morphologies are shown in Figure 2. HCO is composed of triacylglycerols (TAGs), which can crystallize in a spherulitic pattern depending on the processing conditions.[16] Rosettes, which have a similar structure as spherulites, are composed of a core and radially grown fibers from the surface of the core. Winderlich[17] suggested the formation of polymer spherulites need a heterogeneously nucleated core, which may be have been due to the impurities of the system. Hollander et al.[18] implied that many needlelike single crystals grow out radially after a three-dimensional nucleation from a central point to form spherulites. The morphology of β-n,n,n TAG spherulitic crystal

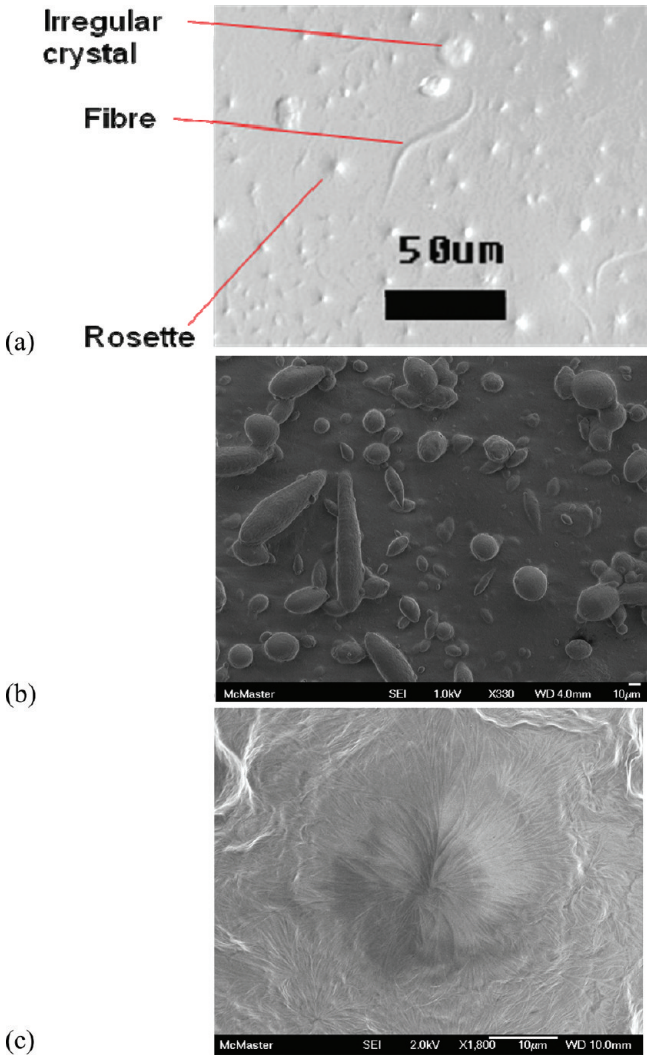

Figure 2. HCO crystal morphology: (a) the three morphologies, (b) irregular crystals, (c) rosettes obtained by SEM.

has also been proved experimentally and theoretically using Monte Carlo simulation by Hollander et al.,[19] indicating that the top face has a smaller edge free energy than the basal and side faces resulting in fastest growth rate.[20−22] Kellens et al.[23] also reported different branching components in forming a spherulitic structure. On the basis of isothermal crystallization temperature, grainy, fibrous, feathery, and lamellar microstructures were observed. However, TAGs do not always form spherulitic structures. Depending on the cooling history, they can form individual needles, which are the primary elements of spherulites.[9] In this work, HCO rosettes are a unique, differentiating crystal structure compared with that of the spherulites. In HCO-in-water emulsions, the oil-in-water interface is mediated by the surfactant. The process of crystal growth is controlled by both arrangement of HCO molecules onto the nuclei and diffusion of oil droplets to the nuclei surface through the aqueous medium.

Fibers observed in the crystallization of HCO-in-water emulsions have large aspect ratios, and are usually not straight but curved as shown in Figure 2. A single fibrous crystal has a similar appearance as the branches of a rosette, but the fibers were different structures compared with the rosettes from the beginning of crystallization. The small edge free energy on the top face leads to fast growth in the elongated direction.[19] Crystal morphologies other than rosettes and fibers are categorized as irregular crystals that show irregular shape (Figure 2a).

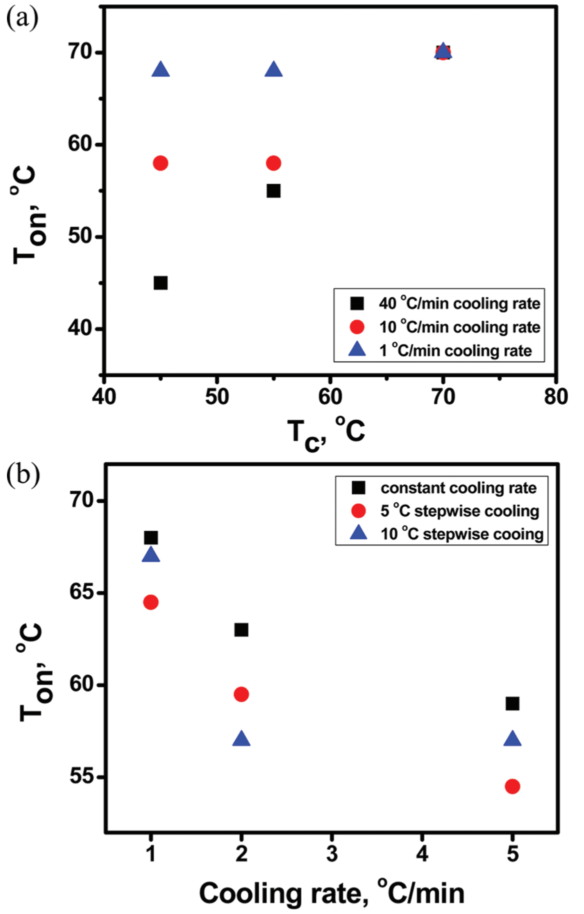

Figure 3. Onset crystallization temperatures versus (a) isothermal temperature and (b) cooling rate.

Irregular crystals are usually formed under high supercooling at quiescent emulsion crystallization. High supercooling provides high driving forces to crystallization such that 2D nucleation does not only start after completion of one layer but may occur simultaneously in different layers resulting in concave faces to form irregular structures. Himawan[16] reported irregular structures when crystallizing a mixture of tripalmitin and tristearin under high supercooling. This type of irregular structure is also reported by Rousset et al.[24]

3.2. Onset Crystallization Temperature. Figure 3a showed the onset temperature of crystallization (T_{on}) at various isothermal target temperatures (T_c) and cooling rates used to reach T_c. Above 75 °C, no crystallization appeared because the supercooling was too small relative to the highest melting temperature (T_m = 84 °C) of HCO crystal suspensions. At T_c = 70 °C, crystallization occurred no matter what cooling rate was used to reach the isothermal temperature. Also, the onset crystallization temperatures were all 70 °C, which meant crystallization did not occur before T_c was reached. When a 40 °C/min cooling rate was used to decrease the temperature of emulsions from 92 °C to the targeted three isothermal temperatures, T_{on} was equal to T_c. Therefore, 40 °C/min was fast enough to create the targeted amount of supercooling (22 °C for T_c = 70 °C, 37 °C for T_c = 55 °C, 47 °C for T_c = 45 °C) without inducing crystallization

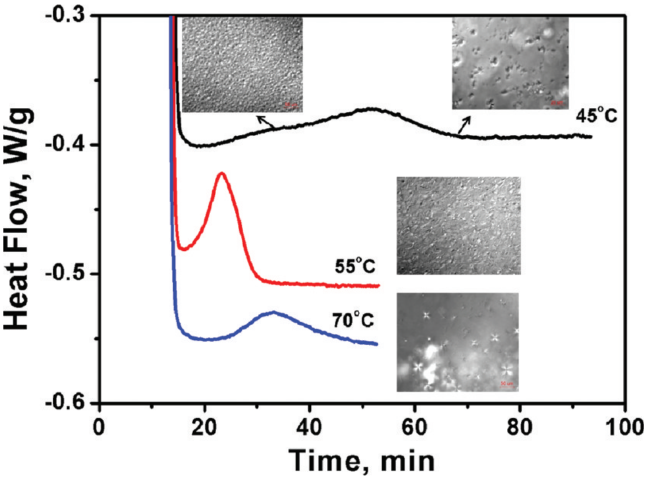

Figure 4. DSC exothermic peaks of HCO-in-water emulsion crystallization at various isothermal temperatures.

during the cooling process. With a cooling rate of 10 °C/min to 55 and 45 °C, T_{on} was the same at 58 °C. For a cooling rate of 1 °C/min to 55 and 45 °C, T_{on} was the same at 68 °C. Hence the crystallization started before T_c was reached. In the case of cooling emulsions to 45 °C, at the rate of 1 °C/min, crystallization was completed before reaching T_c based on the DSC exothermic peak.

In Figure 3b, the onset temperatures of crystallization decreased with increased cooling rates. During constant rate cooling, T_{on} decreased from 68 °C for a 1 °C/min cooling rate to 63 °C for a 2 °C/min cooling rate and 59 °C for a 5 °C/min cooling rate. This implied that HCO molecules had time to rearrange into their thermodynamically favorable conformation at a slow cooling rate, and then molecules packed into the crystals leading to a fast crystallization.[25] On the other hand, during fast cooling rates, the crystallization process was likely transport controlled. HCO molecules needed time to diffuse and grow even if the supercooling was large enough for crystallization.[26−28] During the stepwise cooling, because the sharp cooling procedure went very fast, the crystallization mainly occurred at the isothermal stage. Therefore, the onset temperature of crystallization did not only depend on the supercooling and diffusion but also relied on the temperature values of the isothermal stages. For example, under stepwise cooling with a cooling rate of 1 °C/min and step size of 10 °C, T_{on} was 67 °C and did not equal 68 °C, as found for the constant cooling rate case. It is also noticeable that the order of data points for 2 °C/min differed from the order for 1 °C/min and 5 °C/min. This occurred because before reaching the isothermal step (57 at 2 °C/min cooling rate), the cooling rate was so fast that no nucleation was detected.

3.3. Isothermal Crystallization: High Cooling Rate of 40 °C/min.

3.3.1. DSC and Microscopy. In Figure 4, the DSC exothermic curves representing the crystallization processes at three different isothermal temperatures (70, 55, and 45 °C) and the corresponding micrographs of the crystal morphology are shown. Table 1 provided the specific proportion of each morphology observed at the three isothermal conditions. The single crystallization peak at T_c = 70 °C mainly represented the formation of rosettes, and it took 30 min for the completion of crystallization. However, at T_c = 55 °C, which gave higher supercooling, faster crystallization occurred and about 15 min was used to finish the crystallization. The crystal morphology obtained was a mixture of 31.3% fibers and 68.7% rosettes. After lowering the crystallization temperature to 45 °C, a metastable structure (irregular crystals) formed first and then most of the crystals transformed into rosettes. It required about 50 min to finish the transition, thus the DSC peak was much broader than that of 55 and 70 °C. As triacylglycerols transitioned from less thermal stable structures into more thermal stable ones,[26,29] rosettes showed a more thermally stable nature than irregular crystals.

Table 1. Percentage of Crystal Morphology Crystallized at Different Isothermal Temperature[a]

temperature (°C)	rosettes (%)	fibers (%)	irregular (%)
70	98.4 ± 0.2	1.6 ± 0.2	0
55	31.3 ± 0.3	68.7 ± 0.3	0
45 (16 min)	0	0	100
45 (50 min)	96.2 ± 2.7	0	3.8 ± 2.7

[a] The number after the "±" shows the standard deviation.

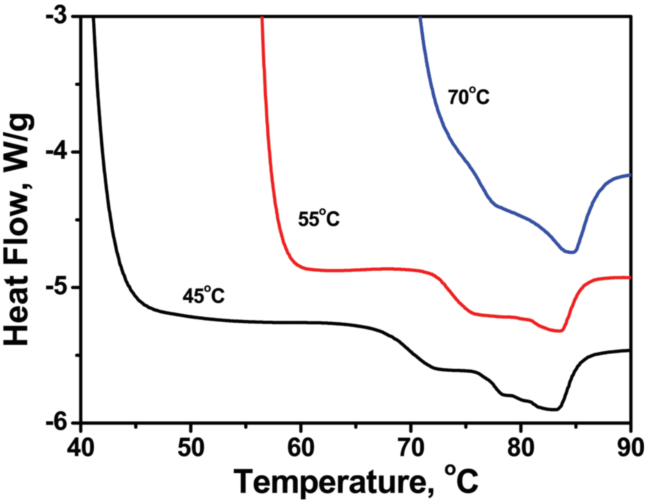

Figure 5. DSC melting curves after crystallization at three different isothermal temperatures: 45, 55, and 70 °C.

In Figure 5, the DSC melting curves showed the thermal behavior of crystals obtained immediately after the formation of different morphologies in Figure 4. The curves for 70 and 55 °C showed similar patterns and the same characteristic melting points of ∼84 and ∼77 °C. Therefore, either the rosettes or fibers had the two characteristic melting points. The melting curve for 45 °C gave two more melting points (∼72 and ∼80 °C) due to the introduction of irregular crystals. The lesser values of melting points for irregular crystals also showed a less thermal stable nature as compared to rosettes and fibers. In summary, for HCO it was found that rosettes and fibers were relatively thermally stable and irregular crystals were relatively less stable.

3.3.2. X-ray Powder Diffraction. Small and wide-angle X-ray powder diffraction were applied for HCO polycrystalline phase analysis. In Figure 6, diffraction patterns of HCO powder obtained by isothermal crystallization were shown for the crystallization temperature range from 45 to 70 °C. The scattering angle 2θ ranged from 1 to 24°. The X-ray pattern of the HCO particle showed its characterized d-spacings at the small angle range were: 47.2, 32.5, and 16.9 Å, and those at wide angle range were 4.46 and 3.97 Å. It was found that the X-ray patterns of samples

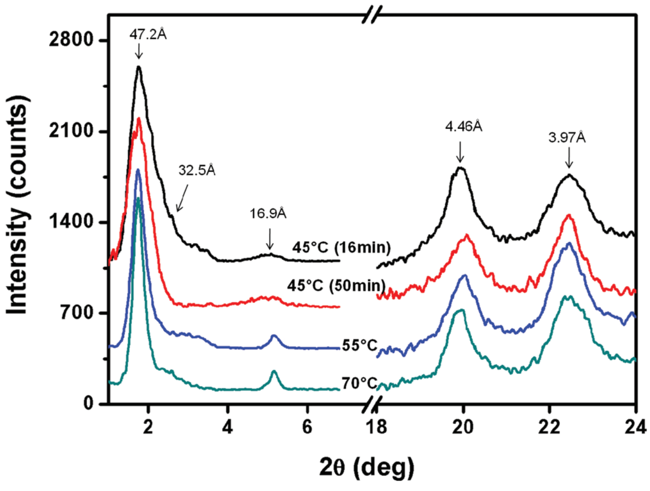

Figure 6. Small and wide-angle X-ray diffraction pattern for HCO particles crystallized from different isothermal temperatures.

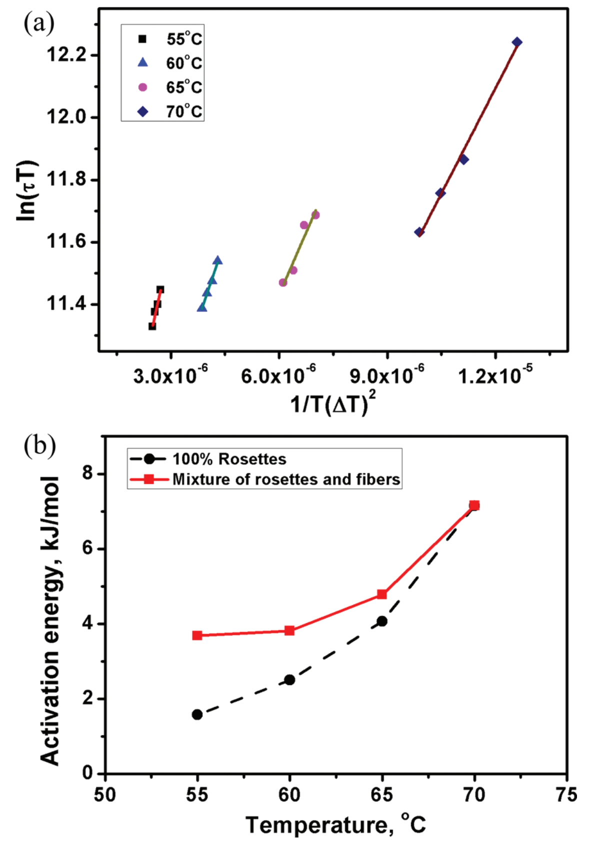

Figure 7. Activation free energy for nucleation at isothermal temperatures from 55 to 70 °C by the Fisher−Turnbull equation: (a) calculation of activation energy and (b) activation energy versus isothermal temperature.

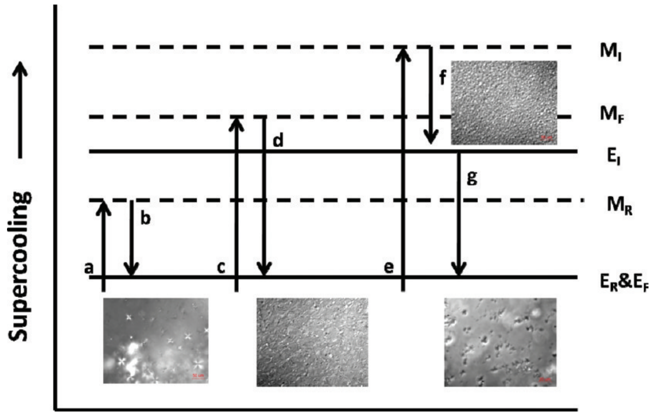

Figure 8. Possible arrangement of the equilibrium and metastable zones for the three morphologies versus the temperature. The direction of the arrow showed the increase of the supercooling. The temperature of equilibrium and metastable zones had been represented by solid lines and dashed lines, respectively.

crystallized at 55 and 70 °C were similar, which suggested that no polymorphism change existed. The result of no polymorphic change coincided with the information from the DSC melting curves for samples crystallized at 55 and 70 °C showing the same two characteristic peaks (Figure 5). In the wide angle region (18−24°), X-ray patterns of HCO powder obtained at 45 °C with a 16 min hold showed a larger peak at 4.46 Å compared with a 50 min hold, which indicated the polymorphic transition. The polymorphic transition at 45 °C from a 16 to 50 min hold was also shown in the small angle region (1−7°) where the magnitude of the peak at 32.5 Å decreased but increased at 16.9 Å. The polymorphic change reflected the morphological change from irregular crystals to rosettes with the increase in hold time at 45 °C. However, the pattern after transition at 45 °C was different with that obtained by primary nucleation at 70 °C, although both showed similar rosettelike morphology.

3.3.3. Nucleation and Activation Free Energy. The Fisher−Turnbull equation was used for a nucleation kinetics study for triacylglycerols and their emulsions.[14,30,31] The nucleation rate J was expressed as

$$J = \frac{NkT}{h}\exp\left(-\frac{\Delta G_d}{kT}\right)\exp\left(-\frac{\Delta G_c}{kT}\right) \qquad (1)$$

where the first exponential term denoted diffusion effects and the second exponential term denoted the activation energy where ΔG_c was the activation free energy. As the nucleation rate was inversely proportional to induction time, plotting the slope (s) of log (τT) versus $1/T(\Delta T)^2$, the activation free energy was calculated as $\Delta G_c = sk/(\Delta T)^2$, where ΔT was the supercooling. In Figure 7a, the activation free energy for nucleation from isothermal temperature 55 to 70 °C was calculated and the actual values versus temperature shown as square plots in Figure 7b. The round plots represented the activation energy when 100% rosettes formed. The difference in activation energy between the two situations increased with a decrease of the temperature. From Table 1 it was shown that with a decrease of the isothermal temperature from 70 to 55 °C, the proportion of fibers increased. Therefore, the increased proportion of fibers indicated a higher activation energy to nucleate compared to the rosettes.

In Figure 8, a sketch of the nucleation barrier as a function of temperature[6] explained the formation and transition of morphologies. Rosettes and fibers showed the same equilibrium temperatures (E_R and E_F), around 84 °C obtained from DSC melting curves in Figure 5. The larger peak of the two melting peaks was chosen to represent the melting point of rosettes and fibers. In the same way, the melting point of irregular crystals (E_I) was chosen as 72 °C. The effective energy barrier must be

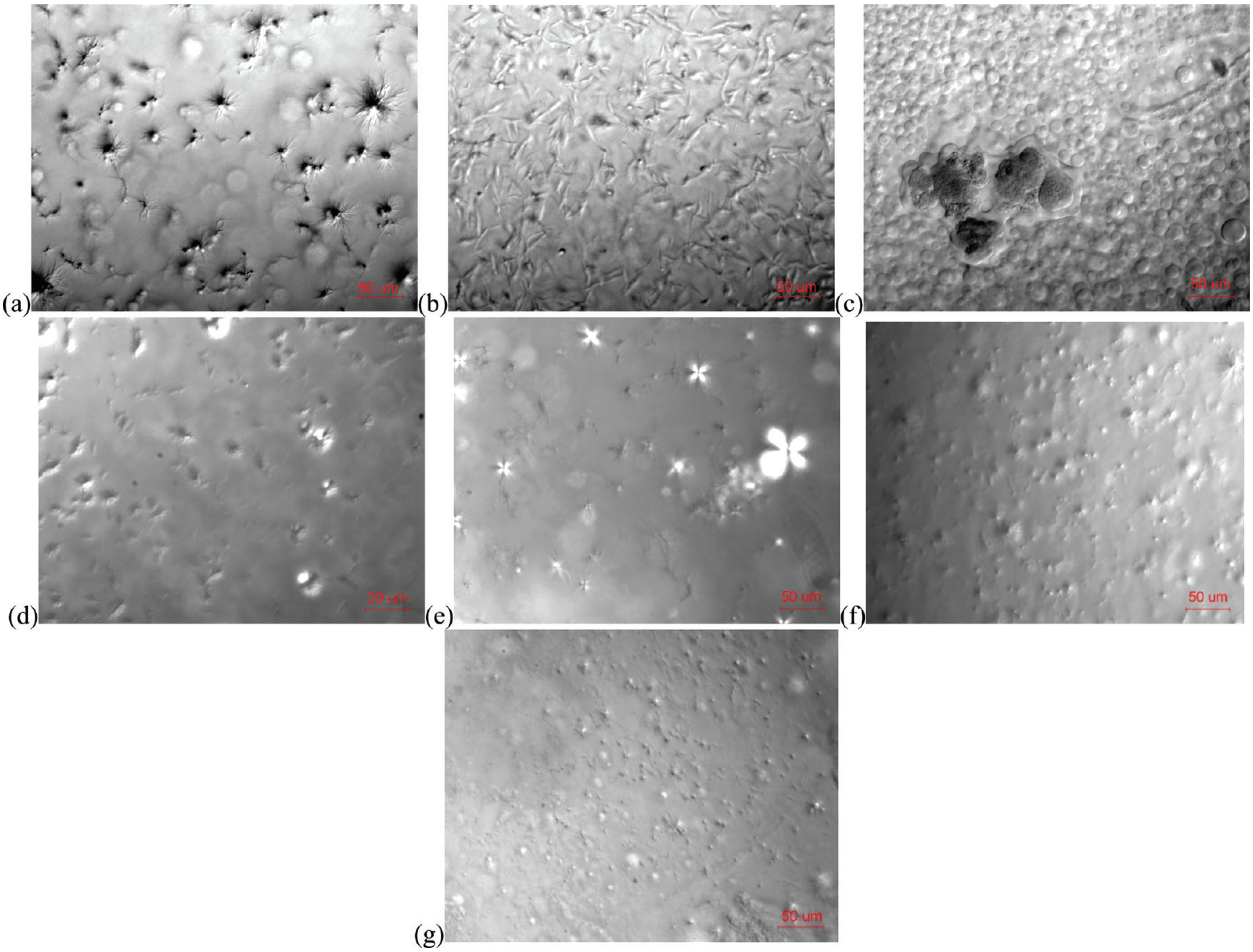

Figure 9. HCO crystal morphology under various crystallization temperatures with the cooling rate of 10 °C/min (a) 70 °C, (b) 55 °C, (c) hold at 45 °C for 10 min, (d) hold at 45 °C for 45 min; cooling rate of 1 °C/min (e) 70 °C, (g) 55 °C, (f) 45 °C.

overcome to achieve nucleation that gave rise to metastable zones (M_R, M_F, and M_I) for rosettes, fibers, and irregular crystals. Step a–g denoted the trajectories of crystallization as a result of fast cooling from the melt. Steps a, c, and e represented isothermal crystallization at 70, 55, and 45 °C, respectively. Step a applied the lowest supercooling compared to steps c and e. For step c, the supercooling was large enough to reach the metastable zone of fibers so both rosettes and fibers appeared. After further increasing the supercooling (step e), the metastable zone of irregular crystals was reached. On the basis of the Ostwald rule of stages,[32] the thermodynamically least stable polymorph would crystallize first (step f). That was the reason why irregular crystals were observed at the beginning. It was suggested that the transformation would happen from the less stable polymorph to the more stable polymorph[33] (step g). This coincided with the phenomena of irregular crystals transforming into rosettes. Also it was reasonable to suggest that the metastable zone of fibers was wider than the equilibrium zone of irregular crystals. Therefore, the solid state transition occurred from irregular crystals to rosettes rather than fibers.

3.4. Nonisothermal Crystallization. *3.4.1. Lower Cooling Rate: 10 and 1 °C/min.* When 10 and 1 °C/min were used to bring emulsions to the crystallization temperature of 70 °C, HCO crystal morphology (Figure 9) showed similar patterns with that observed for cooling with 40 °C/min. Table 2 showed that the proportions of rosettes of all three conditions were close to unity. For all three conditions, the same supercooling was applied to induce nucleation because no nucleation started before reaching the isothermal temperature. This is also termed as near-isothermal crystallization by Marangoni et al.[34] On the basis of the discussion in section 3.3.1, it was suggested that the amount of supercooling was so small that the activation energy provided was only large enough for the nucleation of rosettes.

For T_c = 55 °C, with a 10 °C/min cooling rate, crystallization started at 58 °C, as indicated in Figure 3a. The supercooling ($T_M - 58$) was smaller compared to ($T_M - 55$) for T_{on} = 55 °C with a 40 °C/min cooling rate. However, the morphology was similar under the two cooling rates, which suggested that the difference of the two supercooling cases was too small to produce a difference in the morphology ratio. However, when cooling emulsions at 1 °C/min, the proportion of rosettes increased dramatically while that of the fibers decreased. For constant cooling at 1 °C/min, crystallization started at 68 °C, the peak temperature was 58 °C, and crystallization was completed around 45 °C. In this case, the actual supercooling starting the nucleation was not ($T_M - 55$) but ($T_M - 68$), which was much smaller, so less fibers were found.

Table 2. Proportions of Crystal Morphology for Isothermal Crystallization with the Cooling Rate of 10 and 1 °C/min[a]

	10 °C/min			1 °C/min		
isothermal temperature (°C)	rosette (%)	fiber (%)	irregular (%)	rosette (%)	fiber (%)	irregular (%)
70	96.5 ± 1.1	3.5 ± 1.1	0	100	0	0
55	21.6 ± 1.7	78.4 ± 1.7	0	93.6	6.4	0
45 (16 min)	0	0	100	91.6 ± 1.2	8.4 ± 1.2	0
45 (45 min)	98.0 ± 2.9	0	2.0 ± 2.9	91.6 ± 1.2	8.4 ± 1.2	0

[a] The number after the "±" shows the standard deviation.

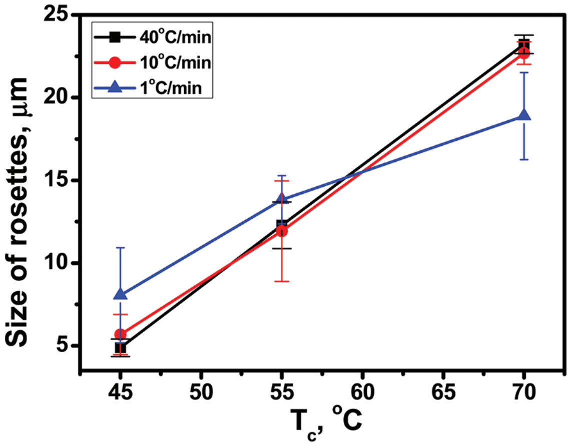

Figure 10. Mean size of rosettes for isothermal crystallization with different cooling rates.

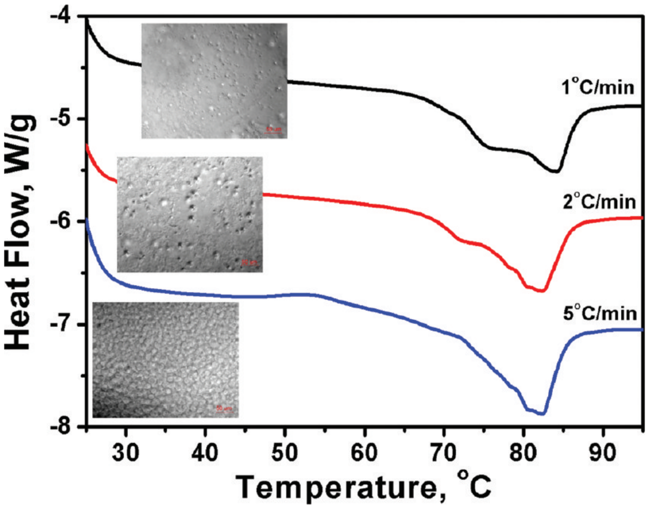

Figure 11. DSC endothermic curves coupled with the corresponding morphology.

Table 3. Percentage of Crystal Morphology at Different Isothermal Temperature[a]

cooling rate (°C/min)	rosettes (%)	fibers (%)	irregular (%)
1	91.6 ± 1.2	8.4 ± 1.2	0
2	42.1 ± 7.4	1.6 ± 1.4	56.3 ± 8.8
5	1.1 ± 1.5	0	98.9 ± 1.5

[a] The number after the "±" shows the standard deviation.

At a crystallization temperature of 45 °C, the same transition of crystal morphology from irregular crystals to rosettes at 40 °C/min cooling rate were obtained for a cooling rate of 10 °C/min. However, at a cooling rate of 1 °C/min, there was no such transition because the crystallization had completed before reaching 45 °C based on the DSC results.

3.4.2. Mean Crystal Size. In Figure 10, the mean crystal size of rosettes was plotted at various cooling conditions. It was shown that with the decrease of crystallization temperature, the mean size of the rosettes decreased because higher supercooling induced a higher nucleation rate. As the total amount of crystals was constant, at the higher nucleation rate, the crystal size decreased.

At T_c = 70 °C, it was found that the size of the rosette decreased with a decreased cooling rate. This meant the lower the cooling rate, the higher the nucleation rate. For low cooling rates, before reaching the crystallization temperature, the HCO molecules had enough time to prepare for packing into the favored position to crystallize. Thus, the induction for nucleation was low, which gave rise to a higher nucleation rate.

At T_c = 55 °C, because the supercooling between 40 °C/min cooling ($T_M - 55$) and 10 °C/min cooling ($T_M - 58$) was similar, no major difference was observed between the crystal sizes. However, for a cooling of 1 °C/min, the supercooling ($T_M - 68$) to induce nucleation was much smaller, so larger crystal sizes were obtained. Similar results were shown for T_c = 45 °C, where cooling at 1 °C/min had a larger crystal size than cooling at 40 and 10 °C/min. The crystal size for 10 °C/min cooling was larger than that of 40 °C/min because of lower supercooling for nucleation.

3.4.3. Constant Cooling Rate. The constant rate and stepwise cooling studies are of importance in industrial applications. For example, crystallization can occur during the recycling of emulsions through cooling equipment, which would be similar to the stepwise cooling profile. In Figure 11, DSC endothermic curves were shown and corresponding microscopy results are included beside the DSC curves. The melting curve of 1 °C/min cooling showed a similar pattern with that of 70 and 55 °C in Figure 5. The two melting points ~84 and ~77 °C indicated the crystal morphology of the combination of rosettes and fibers (Table 3). The results could also be explained through the trajectories shown in Figure 8. At a 1 °C/min cooling rate, which was very low for crystallization, the relatively stable phase of rosettes and fibers formed.[35] At a 2 °C/min cooling rate to 20 °C, more irregular crystals were observed and the DSC melting curve showed similar patterns with that of isothermal cooling at 45 °C (Figure 5). However, these irregular crystals did not transform to the more thermodynamically stable shapes. The occurrence of the solid state transition required the melting of less stable phases and generation of more stable forms.[33] The released energy from forming more stable phases was provided for melting more less

Table 4. Proportion of Morphology under Stepwise Cooling with Different Cooling Rates[a]

	5 °C			10 °C		
cooling rate (°C/min)	rosette (%)	fiber (%)	irregular (%)	rosette (%)	fiber (%)	irregular (%)
1	94.9 ± 1.0	5.1 ± 1.0	0	90.7 ± 2.1	9.3 ± 2.1	0
2	39.5 ± 1.5	0	60.5 ± 1.5	33.6 ± 1.1	2.8 ± 1.0	63.6 ± 2.1
5	0	0	100	0	0	100

[a] The number after the "±" shows the standard deviation.

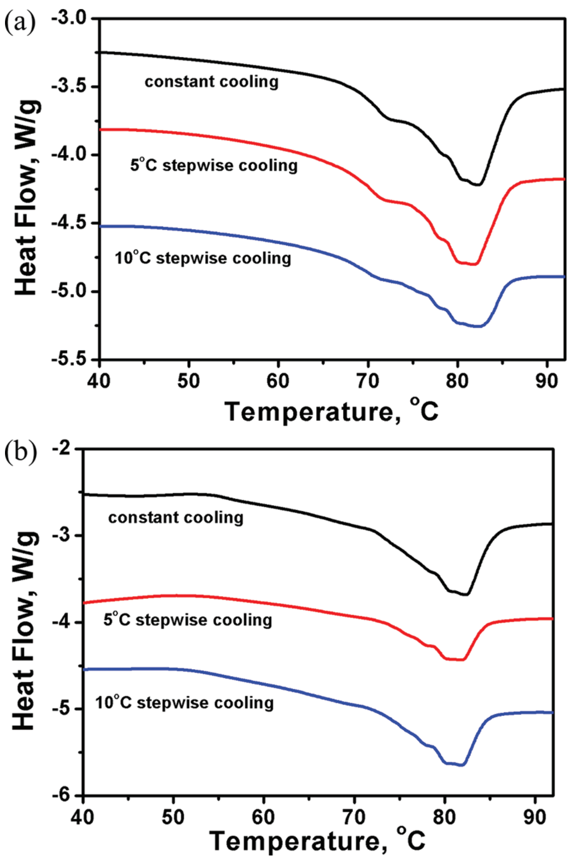

Figure 12. DSC melting curves under (a) 2 °C/min cooling rate and (b) 5 °C/min cooling rate.

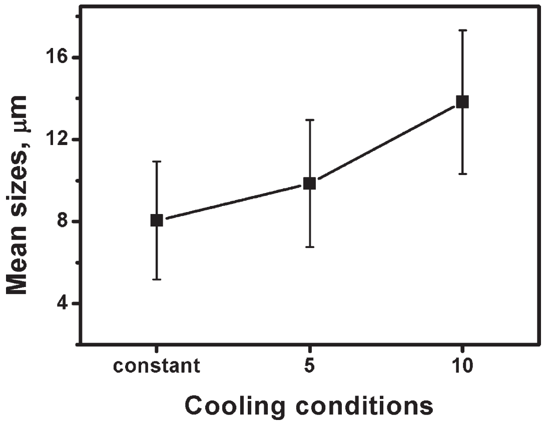

Figure 13. Mean sizes of rosettes crystallized under a 1 °C/min cooling rate; constant—constant rate cooling; 5—5 °C step size; 10—10 °C step size.

stable phases. This crystallization process might happen due to any factors that reduced the energy barrier to nucleation, i.e., impurities, temperature.[35] Compared to the solid state transition of isothermal crystallization at 45 °C (Figure 5), 20 °C was much further away from the melting points of irregular crystals (~72 °C), so the energy required to melt irregular crystals was much larger. The transition at 45 °C took 34 min as indicated previously, but at 20 °C almost no transition happened during 24 h. At a cooling rate of 5 °C/min, before the formation of rosettes and fibers, the metastable zone of irregular crystals has been overcome and nearly all irregular crystals were obtained.

3.4.4. Stepwise Cooling. In Table 4, it was shown that the proportion of crystal morphology was similar within the same cooling rate, although the onset points of crystallization was slightly different based on Figure 3b. The DSC melting curves in Figure 12 showed no difference in crystal morphology at the same cooling rate.

In Figure 13, the mean sizes of rosettes formed under the 1 °C/min cooling rate were shown. It was implied that the mean sizes of rosettes increased with the increase of temperature step size. In Figure 3b, it was shown that T_{on} was 67 °C for 10 °C stepwise cooling, which was similar to that observed for the constant rate cooling with a value of 68 °C. After T_{on} was reached, there was 10 min isothermal crystallization for 10 °C stepwise cooling, but the temperature for constant rate cooling was always decreasing. Therefore, the driving force of nucleation for constant rate cooling was larger than 10 °C stepwise cooling, which produced smaller crystals. The onset of crystallization for 5 °C stepwise cooling was 64.5 °C, which produced a higher driving force for nucleation, as compared to that found for 10 °C stepwise cooling, and was the reason for smaller crystals.

4. CONCLUSIONS

Rosettes composed of radially grown fibrous structures starting from a heterogeneously nucleated core required lower activation free energy to nucleate than fibers. Irregular crystals showed less thermally stable behavior than rosettes and fibers. For isothermal crystallization, the crystal morphology and size were mainly determined by the supercooling and induction time for nucleation. Different cooling rates not only gave rise to different proportions of crystal morphologies but also produced different crystal size distributions. The higher the crystallization temperature, the more stable the crystals. Lower crystallization temperatures (55 °C) reduced the nucleation barrier, and further reductions in the crystallization temperature (45 °C) produced a less thermodynamically stable irregular crystal.

For nonisothermal crystallization, the lower the cooling rate, the more stable the polymorph, specifically rosettes and fibers. A fast cooling rate (i.e., 5 °C/min) produced less stable irregular crystals, which usually transformed into more stable forms that depended on the transition temperature.

AUTHOR INFORMATION

Corresponding Author

*Phone: +1-519-661-2128. Fax: +1-519-850-2399. E-mail: ahrymak@uwo.ca.

ACKNOWLEDGMENT

The authors thank Dr. Kari Dalnoki-Veress for facilitating this work through the use of the hot-stage microscope.

REFERENCES

(1) Marti, I.; Hofler, O.; Fischer, P.; Windhab, E. Rheology of Concentrated Suspensions Containing Mixtures of Spheres and Fibers. *Rheol. Acta* **2005**, *44*, 502.

(2) Johansen, A.; Schafer, T. Effects of Interactions between Powder Particle Size and Binder Viscosity on Agglomerate Growth Mechanisms in a High Shear Mixer. *Eur. J. Pharm. Sci.* **2001**, *12*, 297.

(3) Magauran, E. D.; Reynolds, W.; DiCarlo, L.; Cody, C.; Chiavoni, A.; El-Shoubary, M. *Rheological Additive Comprising Derivatives of Castor Oil.* U.S. Patent 5,340,390, August 23, 1994.

(4) Goddinger, D.; Nordende, K.; Schroeder, T. *Antidandruff Shampoo.* U.S. Patent Application 20090169644 A1, July 2, 2009.

(5) Threlfall, T. Crystallization of Polymorphs: Thermodynamic Insight into the Role of Solvent. *Org. Process Res. Dev.* **2000**, *4*, 384.

(6) Boerrigter, S. *Modeling of Crystal Morphology- Growth Simulation on Facets in Arbitrary Orientations.* Ph.D. Thesis, University of Nijmegen, The Netherlands, 2003.

(7) Bernstein, J.; Davey, R. J.; Henck, J. Concomitant Polymorphs. *Angew. Chem., Int. Ed.* **1999**, *38*, 3440.

(8) Spicer, P. T.; Hartel, R. W. Crystal Comets: Dewetting During Emulsion Droplet Crystallization. *Aust. J. Chem.* **2005**, *58*, 655.

(9) Marangoni, A.; Narine, S. *Physical Properties of Lipids*; Marcel Dekker: New York, 2002.

(10) Hartel, R. *Crystallization in Foods*, 1st ed.; Food Engineering Series; Aspen Publishers: Gaithersburg, MD, 2001.

(11) Garti, N.; Sato, K. *Crystallization Processes in Fats and Lipid Systems*; Marcel Dekker: New York, 2001.

(12) Coupland, J. N. Crystallization in Emulsions. *Curr. Opin. Colloid Interface Sci.* **2002**, *7*, 445.

(13) Lopez, C.; Bourgaux, C.; Lesieur, P.; Bernadou, S.; Keller, G.; Ollivon, M. Thermal and Structural Behavior of Milk Fat: 3. Influence of Cooling Rate and Droplet Size on Cream Crystallization. *J. Colloid Interface Sci.* **2002**, *254*, 64.

(14) Toro-Vazquez, J.; Herrera-Coronado, V.; Dibildox-Alvarado, E.; Charo-Alonso, M.; Gomez-Aldapa, C. Induction Time of Crystallization in Vegetable Oils, Comparative Measurements by Differential Scanning Calorimetry and Diffusive Light Scattering. *J. Food Sci.* **2002**, *67*, 1057.

(15) Tahabukina, E.; Jego, F.; Haudin, J.-M.; Navard, P.; Peuvrel-Disdier, E. Effect of Shear on the Rheology and Crystallization of Palm Oil. *J. Food Eng.* **2009**, *74*, E405.

(16) Himawan, C.; Starov, V.; Stapley, A. Thermodynamic and Kinetic Aspects of Fat Crystallization. *Adv. Colloid Interface Sci.* **2006**, *122*, 3.

(17) Winderlich, B. *Macromolecular Physics*, Vol. 1 Crystal Structure, Morphology, Defects; Academic Press: New York, 1973.

(18) Hollander, F.; Kaminski, D.; Duret, D.; van Enckevort, W.; Meekes, H.; Bennema, P. Growth and Morphology of Thin Fat Crystals. *Food Res. Int.* **2002**, *35*, 909.

(19) Hollander, F.; Boerrigter, S.; van der Streek, J.; Grimbergen, R.; Meekes, H.; Bennema, P. The Implication of the Connected Net Topology on the Morphology of β−monoacid Triacylglycerol Crystals. *J. Phys. Chem. B* **1999**, *103*, 8301.

(20) Hollander, F.; Boerrigter, S.; van der Streek, J.; Bennema, P.; Meekes, H. Comparing the Morphology of β-n,n,n with β'-n,n+2,n and β'-n,n,n-2 Triacylglycrol Crystals. *J. Phys. Chem. B* **2003**, *107*, 5680.

(21) Boerrigter, S.; Hollander, F.; van der Streek, J.; Bennema, P.; Meekes, H. Explanation for the Needle Morphology of Crystals Applied to a β' Triacylglycerol. *Cryst. Growth Des.* **2002**, *2*, 51.

(22) Meekes, H.; Boerrigter, S.; Hollander, F.; Bennema, P. Needle Crystal Morphology Explained. *Chem. Eng. Technol.* **2003**, *26*, 3.

(23) Kellens, M.; Meeussen, W.; Reynaers, H. Study of the Polymorphism and the Crystallization Kinetics of Tripalmitin: A Microscopic Approach. *J. Am. Oil Chem. Soc.* **1992**, *69*, 906.

(24) Rousset, Ph.; Rappaz, M. Crystallization Kinetics of the Pure Triacylglycerols Glycerol-1,3-diplamitate-2-oleate, Glycerol-1-plamitate-2-oleate-3-stearate, and Glycerol-1,3-distearate-2-oleate. *J. Am. Oil Chem. Soc.* **1996**, *73*, 1051.

(25) Martini, S.; Herrera, M. L.; Hartel, R. W. Effect of Cooling Rate on Nucleation Behavior of Milk Fat-Sunflower Oil Blends. *J. Agric. Food Chem.* **2001**, *49*, 3223.

(26) Sato, K. Crystallization Behavior of Fats and Lipids — A Review. *Chem. Eng. Sci.* **2001**, *56*, 2255.

(27) Campos, R.; Narine, S. S.; Marangoni, A. G. Effect of Cooling Rate on the Structure and Mechanical Properties of Milk Fat and Lard. *Food Res. Int.* **2002**, *35*, 971.

(28) Tippetts, M.; Martini, S. Effect of Cooling Rate on Lipid Crystallization in Oil-in-Water Emulsions. *Food Res. Int.* **2009**, *42*, 847.

(29) Timms, R. E. Phase Behavior of Fats and Their Mixtures. *Prog. Lipid Res.* **1984**, *23*, 1.

(30) Herrera, M L.; Falabella, C.; Melgarejo, M.; Anon, M. C. Isothermal Crystallization of Hydrogenated Sunflower Oil: 1- Nucleation. *J. Am. Oil Chem. Soc.* **1998**, *75*, 1273.

(31) Kloek, W.; Walstra, P.; van Vliet, T. Nucleation Kinetics of Emulsified Triglyceride Mixtures. *J. Am. Oil Chem. Soc.* **2000**, *77*, 643.

(32) Nyvlt, J. The Ostwald Rule of Stages. *Cryst. Res. Technol.* **1995**, *30*, 443.

(33) Sato, K. Polymorphic Transformations in Crystal Growth. *J. Phys. D: Appl. Phys.* **1993**, *26*, B77.

(34) Marangoni, A. G.; Tang, D.; Singh, A. P. Non-isothermal Nucleation of Triacylglycerol Melts. *Chem. Phys. Lett.* **2005**, *419*, 259.

(35) Sonoda, T.; Takata, Y.; Ueno, S.; Sato, K. Effect of Emulsifiers on Crystallization Behavior of Lipid Crystals in Nano-size Oil-in-Water Emulsion Droplets. *Cryst. Growth Des.* **2006**, *6*, 306.

Chapter 3 Crystal Morphology of Hydrogenated Castor Oil in the Crystallization of Oil-in-Water Emulsion: Part 2. Effect of Shear

In this chapter, I performed all the experiments, characterization and manuscript preparation. Dr. Andrew Hrymak supervised this work and participated in the edits on the manuscript. Dr. Musa Kamal provided the experimental facility with the Linkam Shear Stage and useful discussions. The manuscript has been published in the journal *Industrial & Engineering Chemistry Research*.

Yang, D., Hrymak, A. N., Kamal, M. R., Crystal Morphology of Hydrogenated Castor Oil in the Crystallization of Oil-in-Water Emulsions: Part 2. Effect of Shear. *Ind. Eng. Chem. Res*. **2011**, 50(20), 11594-11600.

I&EC research
Industrial & Engineering Chemistry Research

ARTICLE

pubs.acs.org/IECR

Crystal Morphology of Hydrogenated Castor Oil in the Crystallization of Oil-in-Water Emulsions: Part II. Effect of Shear

Dingzheng Yang,[†] Andrew N. Hrymak,[*,‡] and Musa R. Kamal[§]

[†]Department of Chemical Engineering, McMaster University, Hamilton, Ontario, L8S4L7, Canada
[‡]Department of Chemical and Biochemical Engineering, University of Western Ontario, London, Ontario, N6A 5B9, Canada
[§]Department of Chemical Engineering, McGill University, Montreal, Quebec, Canada

ABSTRACT: Crystallization of hydrogenated castor oil-in-water emulsions has been studied by polarized light microscopy under controlled shear. Shear rates from 0 to 100 s^{-1} have been applied at cooling rates from 1 to 5 °C/min. Emulsions have been redispersed by shear before crystals formed. The higher the shear rate, the smaller the droplet size. Nucleation has been promoted with the increase of shear rate. Morphology analysis indicates that crystals in the form of fibers favor gentle shear, i.e., 1 s^{-1}, but fibers can be broken up with the increase of shear time. Crystals as rosettes tend to become elongated in the flow direction. At lower cooling rate (<2 °C/min), mean crystal size decreases with shear rate.

1. INTRODUCTION

In food[1−4] and personal care products,[5] particle structures are important to the rheological properties of the crystal suspensions.[6] The crystal morphology describing the shape of particles depends not only on the component formulation but also on the processing conditions, such as temperature, time, and shear. Studies on the effect of shear on fat crystal morphology are very limited.[7−9] The present study focuses on hydrogenated castor oil (HCO), which is composed of triacylglycerols (TAGs). HCO exhibits three types of crystal morphology: rosettes, fibers, and irregular crystals. Rosettes have a three-dimensional structure composed of a heterogeneously nucleated core and fibers radially grown out from the core. Fibers grow one-dimensionally and often show curves. Other than rosettes and fibers, HCO forms irregular crystals which are formed by the less ordered packing of HCO molecules due to high supercooling or fast cooling.

Davies et al.[10] studied the destabilization of triacylglycerols in a water emulsion using sodium caseinate as the surfactant and suggested that a critical shear stress existed beyond which the emulsions could be destabilized readily. Also, it was found that the crystallized particles acted as an emulsion stabilizer by packing on the oil-in-water interface.[11] Partial coalescence has been studied by many researchers[12−15]suggesting that the protruding crystals into emulsified droplets significantly influence the stability of emulsions.

Shear-induced acceleration of nucleation has been investigated extensively.[4,16−18] Dhonsi[16] concluded that the crystallization kinetics of cocoa butter was independent of shear at 20 °C, but at 23 °C the induction time decreased under shear. This was also confirmed by MacMillian[19] that only the crystallization of high polymorphs was dependent on shear.

The crystal morphology variation induced by shear was studied by Sonwai and Mackley[8] who suggested spherulites formed at low shear, but smaller sized fragments formed when shear increased. When the shear rate is increased further to 100 s^{-1}, crystals tended to aggregate into clusters due to van der Waals forces. A similar morphology transition has been obtained by Tarabukina[9] in the crystallization of palm oil under shear.

Application of shear during the crystallization and crystal formation process significantly affects the final fat crystal morphology and size distribution. However, very little work has been done on the shear-induced crystallization of oil-in-water emulsion systems. The aim of the present study is to elucidate the variation of the three crystal morphologies observed in HCO, rosettes, fibers, and irregular crystals, based on different shear rates and different cooling procedures.

2. MATERIALS AND METHODS

2.1. Materials. Hydrogenated castor oil (BP Chemicals Ltd.) is an industrial chemical, and its major component is tri-12-hydroxystearin. HCO is supplied in a white flake form. The surfactant, linear alkylbenzene sulfonate acid (HLAS), is diluted by distilled water and neutralized with sodium hydroxide solution to pH = 7.5 ± 0.5 to form sodium linear alkylbenzene sulfonate (NaLAS). The concentration of NaLAS is 16.7 wt %. The method of preparation is similar to the industrial practice.[5] No crystallization occurred on NaLAS during the experimental procedures.[20]

2.2. Preparation of HCO-in-Water Emulsions. HCO-in-water emulsions were prepared as follows: (i) 4 wt % HCO was added into 96 wt % NaLAS solution; (ii) the above mixture was melted in a 250 mL round-bottom flask at 92 °C[5,21] in an oil bath and then stirred with a mechanical stirrer at 300 rpm to disperse the oil phase into water by mediation of surfactant; (iii) after holding 5 min to remove the crystal memory, the emulsion was cooled in the oil bath under 300 rpm mechanical agitation until the temperature of final crystal suspension reached room

Received: December 30, 2010
Accepted: September 12, 2011
Revised: August 28, 2011
Published: September 12, 2011

ACS Publications © 2011 American Chemical Society

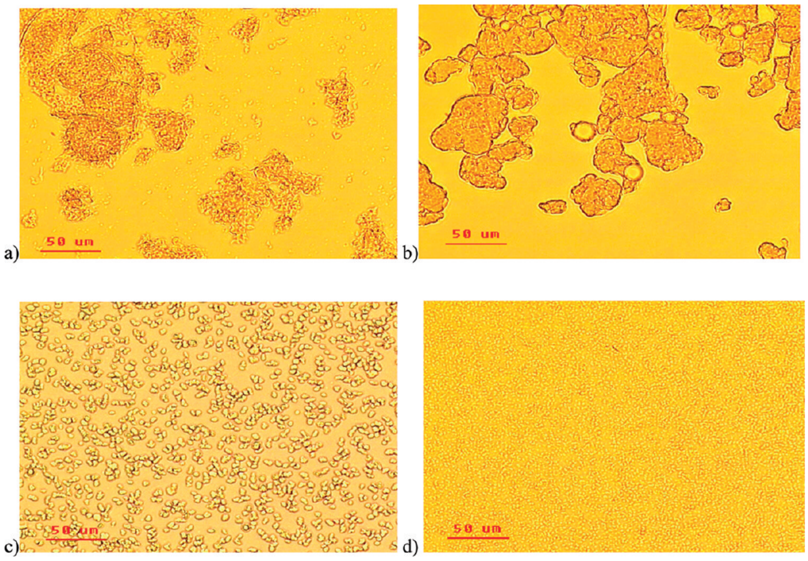

Figure 1. Micrographs of HCO-in-water emulsions under different shear rates: (a) quiescent, (b) 1 s^{-1}, (c) 10 s^{-1}, and (d) 100 s^{-1}.

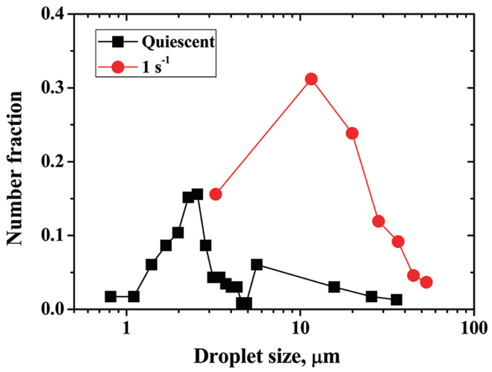

Figure 2. Droplet size distributions of emulsions at quiescent condition and 1 s^{-1} shear rate. (lines to guide the eyes).

temperature. The crystal suspension was stored at room temperature and was stable for more than a month. The HCO suspension can be easily withdrawn with a pipet and remelted to form emulsions. On the basis of optical microscope observation, flocculation may happen before crystallization but coalescence rarely occurred.

The droplet size was measured by microscopy and characteristic parameters, specifically droplet size (d_{32}) and the relative standard deviation (C_x) of the droplet size distribution, were determined as follows:[22,23]

$$d_{ab} = \left(\frac{S_a}{S_b}\right)^{1/a-b} \qquad (1)$$

$$S_x = \sum_i n_i d_i^{\,x} \qquad (2)$$

$$C_x = \sqrt{\frac{S_x S_{x+2}}{S_{x+1}^{\;2}} - 1} \qquad (3)$$

where n_i is the number of droplets with the diameter d_i. a and b are Euclidian dimensions.

Table 1. Characteristic Droplet Sizes, Their Relative Standard Deviation, and Capillary Number at Different Shear Rates

shear rate (s^{-1})	d_{32} (μm)	C_x (μm)	Ca
0	36.34	0.52	
1	40.98	0.44	0.023
10	3.33	0.27	0.018
100	2.24	0.31	0.124

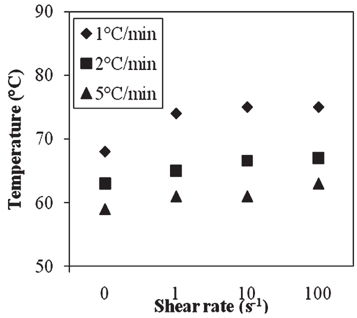

Figure 3. Onset of crystallization temperature at different shear rates and cooling rates.

2.3. Polarized Light Microscopy (PLM).

A polarized light microscope (Olympus, Japan) with transmitted polarized light was used for *in situ* crystal morphology observation under a 20× objective lens. A Linkam Shear Stage CSS450 (Linkam Scientific, Surry, U.K.) was used to quantify the effects of heating and cooling during shear of oil-in-water emulsions. Shear was applied on samples by two parallel highly polished transparent quartz plates with the upper stage stationary and the lower stage rotating in order to generate shear. The gap between the two plates was set at 500 μm to allow HCO three-dimensional crystal growth and avoid wall effects that confine growth.[24] The sample shear was continuous, unidirectional, and steady. Shear rates used were 1, 10, and 100 s^{-1}, and cooling rates were 1, 2, and 5 °C/min.

A digital camera was used to take micrographs of HCO crystals during the crystallization process. It was difficult to obtain images with good quality, while the lower stage was rotating, so the rotation was stopped for 5 s at the end of every minute of rotation to allow for pictures to be taken.[8] The commercial software package ImageJ (NIH) was used for image analysis. Crystal number and sizes were measured manually.

2.4. Onset Crystallization Temperature, T_{on}. Onset temperature of crystallization, T_{on}, was obtained by direct observation through the microscope. The induction time of nonisothermal cooling, τ, was the difference between the start time for crystallization and the time to reach the melting point.[9] The melting point of 84 °C obtained by differential scanning calorimetry (DSC) was used for our studies.

3. RESULTS AND DISCUSSION

3.1. Shear-Induced Destabilization of Emulsions and Redispersion of Droplets. Shear was applied as soon as the temperature started to decrease from 92 °C. Before the onset of crystallization there was enough time for shear to redisperse the oil droplets. Shear-induced destabilization of emulsions depends on the balance between shear forces and interaction between droplets which relies on the chemical properties of oil and surfactants. For shear-induced destabilization in the HCO-in-water emulsion system, flocculation and coalescence dominate the emulsion destabilization at low shear rate. Flocculation is due to the effect of both the London van der Waals attractive force and the electrostatic repulsive force between droplets, which is well-described by DLVO theory (named after Derjaguin, Landau, Verwey, and Overbeek).[25] For flocculation, there is still distance between oil droplets, which is a function of overall interfacial potential, such that droplets maintain their integrity. However for coalescence, the energy barrier between droplets is overcome and small droplets converge into bigger clumps.[11] At higher shear rate, shear forces will overwhelm the effect of flocculation and coalescence to break up droplets into smaller and more uniform sized daughter droplets.[14]

Micrographs of HCO-in-water emulsion at quiescent conditions and 92 °C are shown in Figure 1a. It was found that flocculation happened among droplets because the surfactant

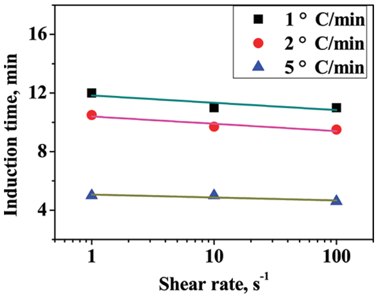

Figure 4. Induction time at different shear rates and cooling rates.

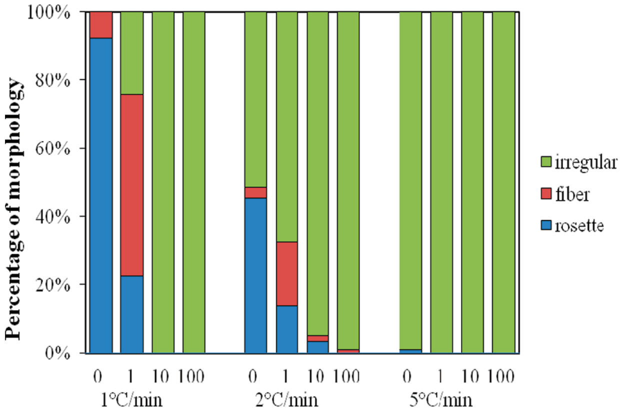

Figure 6. Proportion of crystal morphology at 20 °C under different shear rates and different cooling rates. The first line of the *x*-axis stands by shear rates from 0 to 100 s^{-1}, and the second line stands by different cooling rates from 1 to 5 °C/min.

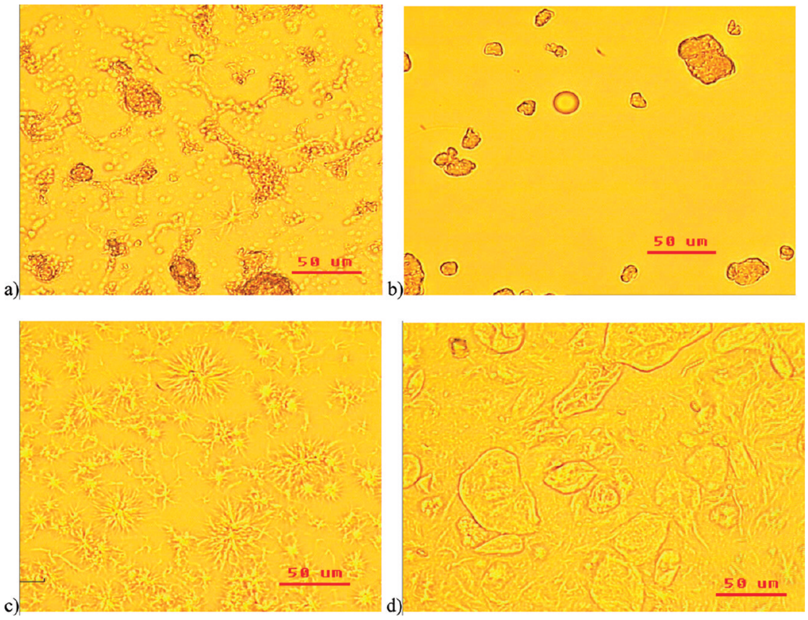

Figure 5. Crystal morphology at the beginning and end of crystallization under quiescent and 1 s^{-1} shear: (a) quiescent crystallization at 65 °C, (b) crystallization with 1 s^{-1} shear rate at 74 °C, (c) quiescent crystallization at 20 °C, and (d) crystallization with 1 s^{-1} shear rate at 20 °C.

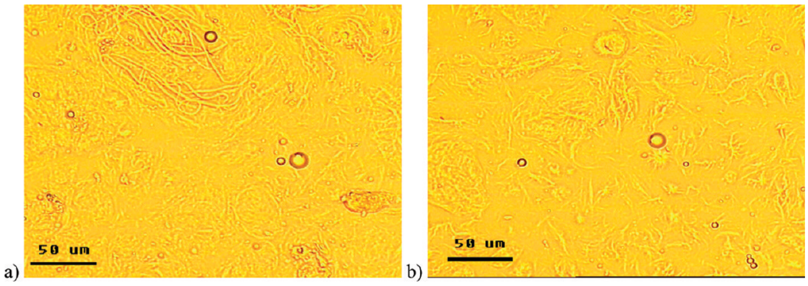

Figure 7. Crystal morphology: (a) aggregation of fibers at 63 °C and (b) breakup of fibers at 55 °C.

NaLAS provides a low energy barrier and van der Waals attraction forces play the key role. At longer times, coalescence occurred producing much larger droplets. At 1 s^{-1} shear rate, the droplet size became bigger and more droplets coalesce to form clumps as shown in Figure 2. The characteristic droplet sizes (d_{32}) and their standard deviation (C_x) were calculated and summarized in Table 1. The characteristic size of droplets increased from 36.34 to 40.98 μm by increasing the shear rate to 1 s^{-1}. In Figure 2, it is clearly shown that droplet size exhibited a bimodal distribution under quiescent conditions but the distribution at 1 s^{-1} only exhibited one peak. Also the number density in the smaller droplet size region (from 8 to 13 μm) for quiescent situations is much larger than that at 1 s^{-1} shear, with the implication that smaller droplets coalesced into larger ones. Shear contributes to the increase of collision frequency between droplets leading to more occurrences of flocculation and coalescence.

At a shear rate of 10 s^{-1}, shear stresses tend to deform and rupture droplets and are larger than the effects of interfacial tension which tends to keep droplets stable.[26] Capillary number (Ca), the ratio between shear stress and interfacial tension, is expressed as follows:

$$\mathrm{Ca} = \frac{\mu\dot{\gamma}}{\sigma/r} \tag{4}$$

where μ is the viscosity of the aqueous surfactant, $\dot{\gamma}$ is the shear rate, σ is the interfacial tension, and r is the dimension of HCO droplets. The interfacial tension can be calculated based on the van Oss approach[27] by introducing van der Waals and acid—base interactions. Because of the lack of parameters of acid—base interactions, accurate calculations are not provided here but estimations are made. The critical capillary number can be estimated from the simple shear curve made by Grace.[28] A critical capillary number of 0.7 is obtained when the relative viscosity between droplets and the continuous phase is 0.4. When the shear rate is increased, the capillary number exceeds its critical value and droplets cannot exist in the stable form and break up into smaller ones.[28,29] As shown in Table 1, the characteristic droplet size deceases dramatically to 3.33 μm compared to 40.98 μm at 1 s^{-1}. The capillary numbers are estimated by eq 4 and shown in Table 1. All the values are smaller than the critical capillary number to maintain the stable mean droplet size. This can also explain why in Figure 1d at much higher shear rate (100 s^{-1}), the mean size of droplet decays further to 2.24 μm in order to maintain a stable form.

At high shear rate, i.e., 100 s^{-1}, the collision frequency[12,28] increases while the time of each interaction decreases. However, van Boekel et al.[30] suggested that the time scale of the encounters were more important for coalescence of paraffin oil-in-water emulsions rather than surfactant and interdroplet forces. Therefore, it is likely that the collision efficiency for coalescence is not high enough such that shear can induce stable oil-in-water emulsions.

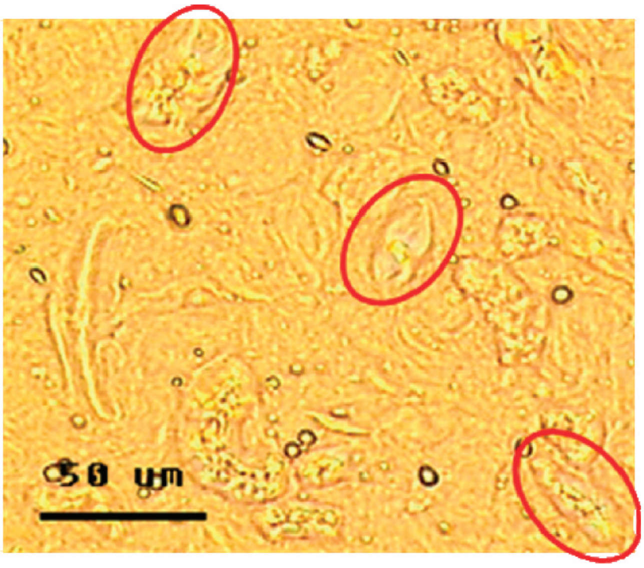

Figure 8. Rosettes with elongated shape: 2 °C/min cooling rate and 1 s^{-1} shear rate.

The shear rate directly affects the droplet size distribution and emulsion morphology, which will further affect the crystal size during the cooling process. From Table 1, it was found that with an increase of the shear rate, the mean droplet size decreased as well as the final crystal size after crystallization. This implies that the mean crystal size is dependent on the size of the emulsified droplet.

3.2. Shear-Induced Enhancement of Nucleation. Supercooling is the driving force for the crystallization of redispersed HCO-in-water emulsions under shear, so when the temperature cools to the onset crystallization temperature (T_{on}) at a given rate, nucleation starts to occur. In Figure 3 it is shown that with the increase of shear rate from 0 to 100 s^{-1}, the onset crystallization temperature (T_{on}) increases continuously at all three cooling rates with accelerated nucleation. This is likely due to the shear rate such that droplet size decreases, leading to a larger curvature of the droplets. The surfaces of these droplets offer a lower barrier for heterogeneous nucleation on those surfaces. Because HCO droplets are deformable under shear, another possible reason for the increase in the onset crystallization temperature is that HCO molecule chains are parallel under

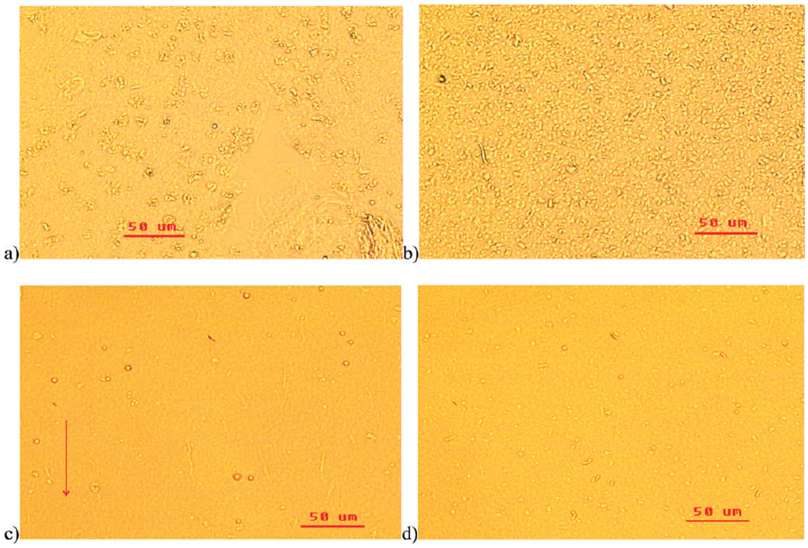

Figure 9. Crystal morphology under 1 °C/min cooling rate at different shear rates: (a) 10 s^{-1} at 65 °C, (b) 10 s^{-1} at 20 °C, (c) 100 s^{-1} at 55 °C, the direction of arrow shows the shear direction, and (d) 100 s^{-1} at 20 °C.

shear stress so that they do not need to adjust their orientation before packing into the crystal conformation reducing the time for the onset of nucleation.[17,31]

Padar et al.[4] suggested that the induction time of β_V cocoa butter was a linear function of the logarithm of the shear rate. Mazzanti et al.[32] reported the similar function between induction time (τ) and shear rate ($\dot{\gamma}$) during the crystallization of β' palm oil and the general equation was summarized as follows:

$$\tau = -m \log(k\dot{\gamma}) \tag{5}$$

Figure 4 shows the experimental data for the induction time, and the straight lines represented the fitted curves to eq 5. On the basis of eq 5, m was estimated as 0.5 min, which was higher than $m \sim 0.2$ min for 5 °C/min cooling. k was 2.2×10^{-24}, 1.58×10^{-21}, and 4.47×10^{-26} for 1, 2, and 5 °C/min, respectively.

The effect of shear on the enhancement of the nucleation rate influenced the final crystal morphology, which depended on both nucleation and growth. With the increase of shear rate, the nucleation rate and number of nuclei increased. The activation energy barrier for nucleation has also been reduced so that the probability of homogeneous nucleation will increase.

3.3. Shear-Induced Crystal Morphology Variation.

3.3.1. Crystallization at Shear Rate of 1 s^{-1} with Cooling Rate of 1 °C/min. If the effect of redispersion of emulsions and nucleation on crystal morphology is indirect, the effect of crystal growth on crystal morphology is direct. As mentioned above, crystallization with shear starts earlier than quiescent crystallization. Therefore, in Figure 5a,b, it is clearly shown that in a quiescent situation crystals form at around 66 °C while at a lower shear rate of 1 s^{-1} crystals form around 74 °C. The crystal morphology at 1 s^{-1} shear rate contains more fibers than rosettes compared to the crystal morphology without shear. This can also be shown by the crystal morphology at the end of crystallization at 20 °C shown in Figure 5c,d. The proportion of each type of morphology that was obtained is shown in Figure 6. The number percentage of fibers increases from 7.6% to 53.2% but that of rosettes decreases from 92.4% to 22.7%. As discussed previously, the formation of fibers required higher activation energy to overcome the energy barrier to nucleate compared to that for rosettes. Therefore, when shear is applied, the activation energy barrier is reduced and it is more likely for fibers to nucleate at the beginning of crystallization. The surface free energy of the fiber is lower at its tip than its base and side, so it tends to grow very long in one dimension.[33−35] Therefore, more fibers are found at the end of crystallization at the 1 s^{-1} shear rate.

In Figure 5d, it is found that some fibers or rosettes grow together with irregular shaped crystals. This interesting phenomenon is caused by shear-induced partial coalescence followed by crystallization. Under shear, the collision frequency of crystal/crystal, crystal/oil, and oil/oil has been enhanced. Upon collision, crystals may aggregate together due to van der Waals attraction forces; oil droplets may coalesce into larger droplets. For collisions between crystals and oil droplets, the crystal can be easily incorporated into the oil drop. When cooling is applied at the same time, a heterogeneous nucleation on the surface of crystals will happen considering the crystal as the nuclei.

As fibers have a long aspect ratio, it is easy for fibers to tangle together during shear flow as shown in Figure 7a. In Figure 7b, with an increase of shear time, long fibers are broken up into short pieces.

Rosettes are three-dimensional crystals with radially distributed fibrils growing out from a nucleus, which is usually sphere-like. However under shear, many elongated rosettes have been observed as shown in Figure 8. Some of these elongated rosettes are formed due to the shear deformation and also some are caused by variation of local mass transfer under shear flow. The shear distribution around a sphere particle under laminar flow has been demonstrated by Wagner et al.[36] It was found that the velocity gradient was the highest at the tangential point and lowest at the stagnation point. Therefore, HCO drops at the tangential point moves fast providing short time for crystal growth. On the contrary, at the stagnation point, fluid is almost stagnant so HCO droplets have more time to grow onto the nuclei. As a result, rosettes will prefer to grow along the flow direction leading to elongated rosettes.[36]

3.3.2. Crystallization at Shear Rates of 10 and 100 s^{-1} with Cooling Rate of 1 °C/min. After a comparison between quiescent crystallization and low shear (1 s^{-1}) crystallization, we focused our study on the effect of higher shear rates (10 and 100 s^{-1}). At a

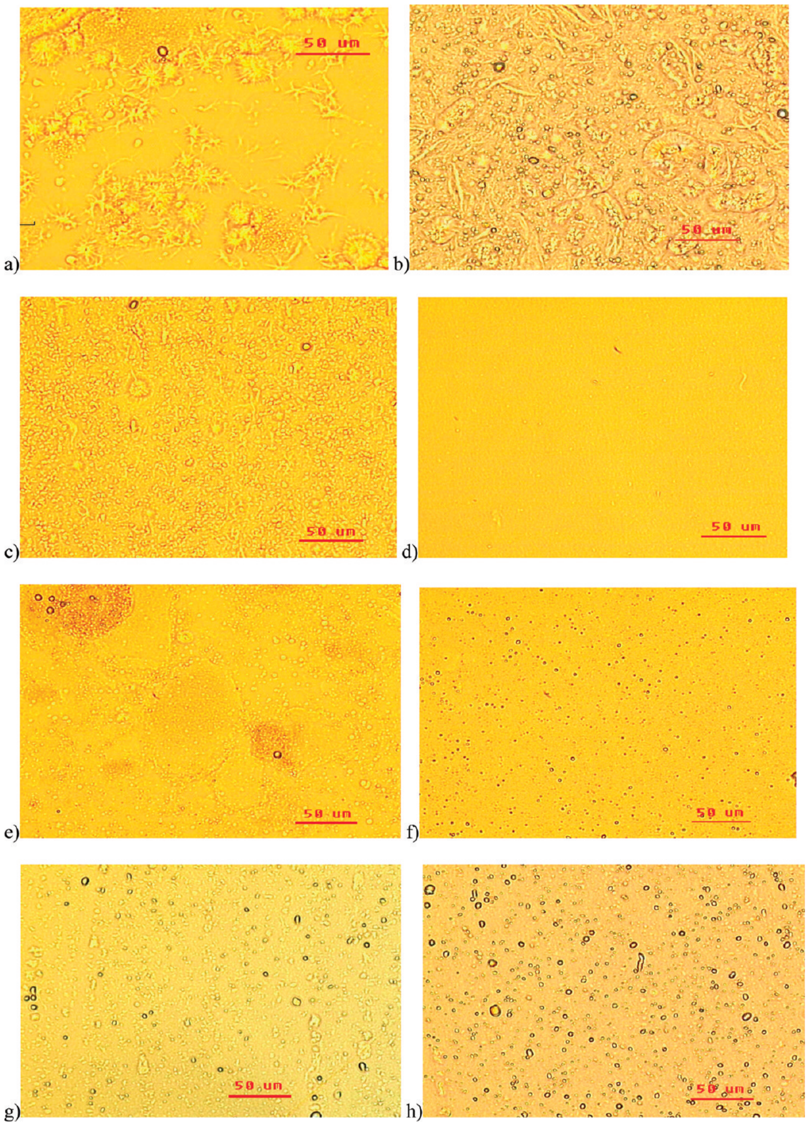

Figure 10. Crystal morphology under 2 and 5 °C/min cooling rates at different shear rates at 20 °C. 2 °C/min: (a) quiescent, (b) 1 s^{-1}, (c) 10 s^{-1}, and (d) 100 s^{-1}. 5 °C/min: (e) quiescent, (f) 1 s^{-1}, (g) 10 s^{-1}, and (h) 100 s^{-1}.

shear rate of 10 s^{-1}, no rosettes are found during the entire crystallization process but fibers do form from the beginning. In Figure 9a, clusters of fibers are clearly shown at 65 °C; however, with increased time under shear, fibers tend to be broken up. As a consequence, fewer fibers can be observed and finally almost no fibers are observed when the sample cools to 20 °C. At a shear rate of 100 s^{-1}, fibers form at first. It is also shown in Figure 10c that the fibers align with a dominant flow direction under laminar flow. However fibers break up by the end of the experiment (Figure 9c,d).

Rosettes are not favored at shear rates of 10 and 100 s^{-1} as shown in Figure 6. It has been explained that at high shear, rosettes are not preferred to form. At high shear rates, HCO droplets move very fast so that the residence time of surrounding oil drops onto the surface of a crystallized droplet is not long enough compared to the time needed for the growth of rosettes,[8] resulting in small sized irregular crystals.

3.3.3. Crystallization at Shear Rates of 1, 10, and 100 s^{-1} with Cooling Rates of 2 and 5 °C/min. As shown in Figure 6 for a 2 °C/min cooling rate, a shear rate of 1 s^{-1} also increases the proportion of fibers compared to the quiescent conditions as discussed in section 3.3.1. However, few rosettes and fibers are observed at both 10 and 100 s^{-1} shear rate conditions (Figure 10). Spherical rosettes are not easily formed under high shear laminar flow[36] compared to one-dimensional fibers, but at the same time fibers can be easily broken up at shear rates above 10 s^{-1}.

At the cooling rate of 5 °C/min, rosettes and fibers are rarely observed, and irregular crystals dominate the crystal morphology distribution (Figure 10e−h). Also, with an increase of the shear rate, the crystal size becomes larger for 5 °C/min cooling. This may be because fragment breakup produces more rough surfaces. The energy of HCO molecules attaching on the rough surfaces is smaller than their attaching on smooth surfaces,[8,37] facilitating growth of larger crystals.

4. CONCLUSIONS

Crystal size was significantly influenced by the redistribution of HCO-in-water emulsions by shear before the onset of crystallization.

The onset temperature of crystallization increased with increasing shear rate. The induction time to nucleation was found to be linear proportional to the logarithm of the shear rate. The formation of fibers was favored under shear conditions because the activation energy barrier decreased with increasing shear rate. Fibers were also shear sensitive because with the increase of shear time, fibers tended to break down into smaller pieces.

AUTHOR INFORMATION

Corresponding Author

*Phone: +1-519-661-2128. Fax: +1-519-850-2399. E-mail: ahrymak@uwo.ca.

ACKNOWLEDGMENT

The authors gratefully acknowledge the Natural Science and Engineering Council for partial support of this work.

REFERENCES

(1) Hartel, R. W. *Crystallization in Foods*; Aspen Publishers: Gaithersburg, MD, 2001.

(2) Sato, K. Crystallization Behavior of Fats and Lipids-a Review. *Chem. Eng. Sci.* **2001**, *56*, 2255.

(3) Marangoni, A. G.; Narine, S. S. *Physical Properties of Lipids*; Marcel Dekker: New York, 2002.

(4) Padar, S.; Mehrle, Y. E.; Windhab, E. J. Shear Induced Crystal Formation and Transformation in Cocoa Butter. *Cryst. Growth Des.* **2009**, *9*, 4023.

(5) Goddinger, D.; Nordende, K.; Schroeder, T. Antidandruff Shampoo. U.S. Patent Application 20090169644 A1, July 2, 2009.

(6) Marti, I.; Hofler, O.; Fischer, P.; Windhab, E. Rheology of Concentrated Suspensions Containing Mixtures of Spheres and Fibers. *Rheol. Acta* **2005**, *44*, 502.

(7) Da Pieve, S.; Calligaris, S.; Co, E.; Nicoli, M. C.; Marangoni, A. G. Shear Nanostructure of Monoglyceride Organogels. *Food Biophys.* **2010**, *5*, 211.

(8) Sonwai, S.; Mackley, M. R. The Effect of Shear on the Crystallization of Cocoa Butter. *J. Am. Oil Chem. Soc.* **2006**, *83*, 583.

(9) Tahabukina, E.; Jego, F.; Haudin, J. M.; Navard, P.; Peuvrel-Disdier, E. Effect of Shear on the Rheology and Crystallization of Palm Oil. *J. Food Eng.* **2009**, *74*, E405.

(10) Davis, E.; Dickinson, E.; Bee, R. Shear Stability of Sodium Caseinate Emulsions Containing Monoglyceride and Triglyceride Crystals. *Food Hydrocolloids* **2000**, *14*, 145.

(11) Rousseau, D. Fat Crystals and Emulsion Stability—a Review. *Food Res. Int.* **2000**, *33*, 3.

(12) Vanapalli, S. A.; Coupland, J. A. Emulsions under Shear—the Formation and Properties of Partial Coalesced Lipid Structures. *Food Hydrocolloids* **2001**, *15*, 507.

(13) Vanapalli, S. A.; Palanuwech, J.; Coupland, J. A. Influence of Fat Crystallization on the Stability of Flocculated Emulsions. *J. Agric. Food Chem.* **2002**, *50*, 5224.

(14) Xu, W.; Nikolov, A.; Wason, D. T. Shear-induce Fat Particle Structure Variation and the Stability of Food Emulsions: I. Effect of Shear History, Shear Rate and Temperature. *J. Food Eng.* **2005**, *66*, 97.

(15) McClements, D. J.; Dickinson, E.; Povey, M. J. W. Crystallization in Hydrocarbon-in-Water Emulsions Containing a Mixture of Solid and Liquid Droplets. *Chem. Phys. Lett.* **1990**, *172*, 449.

(16) Dhonsi, D.; Stapley, A. G. F. The Effect of Shear Rate, Temperature, Sugar and Emulsifier on the Tempering of Cocoa Butter. *J. Food Eng.* **2006**, *77*, 936.

(17) Stapley, A. G. F.; Tewkesbury, H.; Fryer, P. G. The Shear and Temperature History on Crystallization of Chocolate. *J. Am. Chem. Oil Soc.* **1999**, *76*, 677.

(18) Maleky, F.; Marangoni, A. G. Process Development for Continuous Crystallization of Fat under Laminar Shear. *J. Food Eng.* **2008**, *89*, 399.

(19) MacMillan, S. D.; Roberts, K. J. In Situ Small Angle X-ray Scattering (SAXS) Studies of Polymorphism with the Associated Crystallization of Cocoa Butter Fat Using Shearing Conditions. *Cryst. Growth Des.* **2002**, *2*, 221.

(20) Smith, D. Impact of Composition on the Performance of Sodium Linear Alkylbenzenesulfonate (NaLAS). *J. Am. Oil Chem. Soc.* **1997**, *74*, 837.

(21) Spicer, P. T.; Hartel, R. W. Crystal Comets: Dewetting During Emulsion Droplet Crystallization. *Aust. J. Chem.* **2005**, *58*, 655.

(22) Kloek, W.; Walstra, P.; van Vliet, Ton. Nucleation Kinetics of Emulsified Triglyceride Mixtures. *J. Am. Oil Chem. Soc.* **2000**, *77*, 643.

(23) Lopez, C.; Bourgaux, C.; Lesieur, P.; Bernadou, S.; Keller, G.; Ollivon, M. Thermal and Structural Behavior of Milk Fat 3. Influence of Cooling Rate and Droplet Size on Cream Crystallization. *J. Colloid Interface Sci.* **2002**, *254*, 64.

(24) Lee, O.; Kamal, M. R. Experimental Study of Post-Shear Crystallization of Polypropylene Melts. *Polym. Eng. Sci.* **1999**, *39*, 236.

(25) Verwey, E. J. W.; Overbeek, J. Th. G. *Theory of the Stability of Lyophobic Colloids*; Elsevier Publishing: New York, 1948.

(26) Nikolov, A. D.; Wason, D. T. Effect of Surfactant on Multiple Stepwise Coalescence of Single Drops at Liquid-Liquid Interfaces. *Ind. Eng. Chem. Res.* **1995**, *34*, 3653.

(27) Van Oss, C. J.; Chaudhury, M. K.; Good, R. J. Interfacial Lifshitz-van der Waals and Polar Interactions in Macroscopic Systems. *Chem. Rev.* **1988**, *88*, 927.

(28) Grace, H. P. Dispersion Phenomena in High Viscosity Immiscible Fluid Systems and Application of Static Mixers as Dispersion Devices in Such Systems. *Chem. Eng. Commun.* **1982**, *14*, 225.

(29) Tadmor, Z.; Gogos, C. G. *Principle of Polymer Processing*, 2nd ed.; John Wiley & Sons: Hoboken, NJ, 2006; p 342.

(30) van Boekel, M. A. J. S.; Walstra, P. Effect of Couette Flow on Stability of Oil-in-Water Emulsions. *Colloids Surf.* **1981**, *3*, 99.

(31) Herrera, M. L.; Hartel, R. W. Effect of Processing Condition on Physical Properties of a Milk Fat Model System: Microstructure. *J. Am. Oil Chem. Soc.* **2000**, *77*, 1197.

(32) Mazzanti, G.; Marangoni, A. G.; Idziak, H. J. Modeling Phase Transitions during the Crystallization of a Multicomponent Fat under Shear. *Phys. Rev. E* **2005**, *74*, 041607.

(33) Boerrigter, S.; Hollander, F.; van der Streek, J.; Bennema, P.; Meekes, H. Explanation for the Needle Morphology of Crystals Applied to a β' Triacylglycerol. *Cryst. Growth Des.* **2002**, *2*, 51.

(34) Hollander, F.; Boerrigter, S.; van der Streek, J.; Bennema, P.; Meekes, H. Comparing the Morphology of β-n,n,n with β'-n,n+2,n and β'-n,n,n-2 Triacylglycrol Crystals. *J. Phys. Chem. B* **2003**, *107*, 5680.

(35) Meekes, H.; Boerrigter, S.; Hollander, F.; Bennema, P. Needle Crystal Morphology Explained. *Chem. Eng. Technol.* **2003**, *26*, 3.

(36) Wagner, N.; Brady, J. F. Shear Thickening in Colloid Dispersions. *Phys. Today* **2009**, *October*, 27.

(37) Garside, J.; Davey, R. J. Secondary Contact Nucleation: Kinetics, Growth and Scale-up. *Chem. Eng. Commun.* **1980**, *4*, 393.

Chapter 4 Kinetics of Isothermal Crysallization of Hydrogenated Castor Oil-in-Water Emulsions

In this chapter, I performed most of the experiments, characterization, models and manuscript preparation. Stephanie Kedzior did some DSC experiments. Dr. Andrew Hrymak supervised this work and participated in the edits on the manuscript.

The format of this chapter is based on the *Journal of American Oil Chemists' Society* where we have submitted our manuscript.

Abstract

Kinetics of isothermal crystallization of hydrogenated castor oil in water emulsions exhibiting multiple crystal morphologies have been studied experimentally by DSC and polarized light microscopy. The induction time of nucleation increases with the increase of the isothermal temperature under which crystallization occurred. Crystal growth has been observed by microscopy showing that both crystal morphologies, fibers and rosettes, grow linearly at the initial stage of crystallization and then slow down to reach a plateau value. The Avrami model, which has been widely used in kinetics studies of triacylglycerol systems, was employed to fit experimental results at different isothermal temperatures. It is found that experimental trends could be captured by introducing the volume fraction of each type of morphology into three dimensional and one dimensional full Avrami models.

Keywords DSC; microscopy; Hydrogenated castor oil; Emulsion; Crystallization kinetics; Morphology; Avrami model

Introduction

Hydrogenated castor oil (HCO) as a triacylglycerol (TAG) plays essential roles in modifying the rheology of household products and paints [1]. The development of a fundamental understanding of the crystallization process of HCO is very important in making the desired crystal morphology and size distribution to satisfy the requirements of industrial products [2-3]. Crystallization kinetics of TAG has been previously investigated due to its importance to processing and physical properties of products [4-5].

Many experimental techniques have been applied to kinetics studies, such as differential scanning calorimetry (DSC) [6-9], microscopy [10], time resolved X-ray diffraction (XRD) [11] and ultrasound [12]. Wright et al. [10] suggested that the microscopy method was particularly sensitive to study the induction time. XRD [11] can be used in a kinetics study and for determining polymorphic transformation. Due to its accuracy and easy usage, DSC has been most widely used in both isothermal and non-isothermal crystallization [13]. Smith et al. [14] noted the importance of the temperature for isothermal crystallization because no crystallization should occur before reaching the target isothermal temperature.

Recently, models for crystallization kinetics of TAG have been reviewed by Rousset [5], Foubert et al. [15] and Himawan et al. [16]. Those models have been divided into deterministic, numerical and stochastic approaches. The latter two methods are not widely used because of their complexity. The deterministic approach is widely employed in kinetics models such as those by Avrami [17-18], Gompertz [19] and Foubert [20]. The Johnson-Mehl-Avrami-Komogorov (JMAK) model, which was originally developed for metals and then used for polymers, has been also widely used for triacylglycerols [6, 21].

The Avrami model describes the overall crystallization kinetics including both nucleation and crystal growth. Nucleation is assumed to be either instantaneous or sporadic. Instantaneous crystallization indicates that nucleation occurred as soon as the temperature reaches the crystallization temperature. Sporadic nucleation assumes the nucleation rate is a linear function of time, and then the growth rate is assumed to be constant after the formation of nuclei. The Avrami exponent has been given physical meanings by the type of nucleation and dimension of crystal growth. An exponent of zero or one indicated instantaneous and sporadic nucleation respectively; however, the Avrami exponent usually obtained was non-integer and could not explain the physical meaning of the kinetics. Metin and Hartel [6] used approximated Avrami models to fit crystallization kinetics. The full Avrami model [21] provides more parameters; however, there have been problems if more than one morphology are formed. Other deterministic models include the Gompertz model which was first used for microbes and then employed for triacylglycerols by Kloek et al. [19], and the Foubert model [20] which was developed by considering the first order forward reaction and an *n*th order reverse reaction.

In this paper, isothermal crystallization kinetics of HCO is studied for the temperature range from 55°C to 70°C. At this temperature range HCO exhibits two crystal morphologies, rosettes and fibers [2]. The full Avrami model is modified, to better fit the experimental data and give some physical meaning to the parameters, by introducing the volume fraction of each crystal morphology. DSC is used to quantity the degree of crystallization at varying times during the crystallization kinetics time span.

Models

Avrami [17-18] provided an approximate form of the kinetics model expressed as

$$V = V_m[1 - e^{-kt^n}] \tag{1}$$

where *k* is Avrami constant and *n* is Avrami exponent. The approximate model was derived from the full Avrami model [17-18] whose one, two or three dimensional crystallization rates were given as follows

$$V = V_m[1 - e^{-(\sigma_1 \dot{l} N_0 / p)(e^{-\tau} - 1 + \tau)}] \tag{2}$$

$$V = V_m[1 - e^{-(2\sigma_2 \dot{l}^2 N_0 / p^2)(-e^{-\tau} + 1 - \tau + \tau^2 / 2)}] \tag{3}$$

$$V = V_m[1 - e^{-(6\sigma_3 \dot{l}^3 N_0 / p^3)(e^{-\tau} - 1 + \tau - \tau^2 / 2 + \tau^3 / 6)}] \tag{4}$$

where *V* is the crystal volume per unit volume of suspension; V_m is the maximum volume fraction which is less than 1, and depends on the supercooling rate and impurities. Avrami assumed the volume of crystals increased linearly with the volume fraction of remaining liquid, so $\dot{l}$ is the constant growth rate, which can be attained by microscopy. The characteristic dimensionless time is given by $\tau = pt$ where *p* is the probability of growth per unit time. The number density decreases exponentially $N(z) = N_0 e^{-z}$ with time *z*. σ_1 , σ_2 and σ_3 are shape factors. In our case, one-dimensional fibers and three-dimensional rosettes are the only two morphologies, thus

$$\sigma_1 = \frac{1}{4}\pi d_1^2 \tag{5}$$

$$\sigma_3 = \frac{4}{3}\pi \tag{6}$$

We assume that fibers and rosettes have the same density. Thus the volumes per crystals are respectively

$$v_1 = \frac{1}{4}\pi {d_1}^2 L \tag{7}$$

$$v_3 = \frac{1}{6}\pi d_3{}^3 \tag{8}$$

where d_1 is the diameter and L is the length of the fiber, and d_3 is the diameter of the rosette. Estimates of these three parameters, d_1 , d_3 and L, can be obtained by image analysis of the crystal distributions (assuming that fibers are cylindrical and rosettes are spheres) to determine average dimensions. Then introducing the crystal number of the fiber (N_1) and rosette (N_3), where $N=N_1+ N_3$, the maximum total volume per unit suspension are given by

$$V_{m,1} = v_1 N_1 = \frac{1}{4}\pi d_1{}^2 L N_1 \tag{9}$$

$$V_{m,3} = v_3 N_3 = \frac{1}{6}\pi d_3{}^3 N_3 \tag{10}$$

The maximum total volume of all morphologies is

$$V_m = V_{m,1} + V_{m,3} \tag{11}$$

Substitution of Eqs. (9) and (10) into Eqs. (2) and (4) and their sum gives the total volume of all crystals:

$$V_1 = V_{m,1}[1 - e^{-(\sigma_1 \dot{l} N_0 / p)(e^{-\tau} - 1 + \tau)}] \tag{12}$$

$$V_3 = V_{m,3}[1 - e^{-(6\sigma_3 \dot{l}^3 N_0 / p^3)(e^{-\tau} - 1 + \tau - \tau^2/2 + \tau^3/6)}] \tag{13}$$

$$V = V_1 + V_3 = V_{m,1}[1 - e^{-(\sigma_1 l_1 N_0 / p)(e^{-\tau} - 1 + \tau)}] + V_{m,3}[1 - e^{-(6\sigma_3 \dot{l}_3{}^3 N_0 / p^3)(e^{-\tau} - 1 + \tau - \tau^2/2 + \tau^3/6)}] \tag{14}$$

By taking the induction time into account, t becomes (t-τ_i). After re-arrangement, Eq (14) becomes

$$1 - \frac{V}{V_m} = \phi_1 e^{-(\sigma_1 \dot{l}_1 N_0 / p)(e^{-p(t-\tau_i)} - 1 + p(t-\tau_i))} + \phi_3 e^{-(6\sigma_3 \dot{l}_3{}^3 N_0 / p^3)(e^{-p(t-\tau_i)} - 1 + p(t-\tau_i) - p^2 (t-\tau_i)^2/2 + p^3 (t-\tau_i)^3/6)} \tag{15}$$

where the degree of crystallization is $X=V/V_m$. Φ_1 and Φ_3 are the volume fractions of fibers and rosettes respectively at the end of the crystallization, which can be obtained by microscopy. Here it is assumed that fibers and rosettes nucleate simultaneously.

Thus,

$$\phi_1 = \frac{V_{m,1}}{V_{m,3}+V_{m,1}} = \frac{v_1 N_1}{v_3 N_3 + v_1 N_1} = \frac{\frac{1}{4}\pi d_1{}^2 L N_1}{\frac{1}{6}\pi d_3{}^3 N_3 + \frac{1}{4}\pi d_1{}^2 L N_1} = \frac{\frac{1}{4} d_1{}^2 L N_1}{\frac{1}{6} d_3{}^3 N_3 + \frac{1}{4} d_1{}^2 L N_1} \tag{16}$$

$$\phi_3 = \frac{V_{m,3}}{V_{m,3}+V_{m,1}} = \frac{v_3 N_3}{v_3 N_3 + v_1 N_1} = \frac{\frac{1}{6}\pi d_3{}^3 N_3}{\frac{1}{6}\pi d_3{}^3 N_3 + \frac{1}{4}\pi d_1{}^2 L N_1} = \frac{\frac{1}{6} d_3{}^3 N_3}{\frac{1}{6} d_3{}^3 N_3 + \frac{1}{4} d_1{}^2 L N_1} \tag{17}$$

Experimental Procedures

Materials

Hydrogenated castor oil (BP Chemicals Ltd.) has as its major component tri-12-hydroxystearin. HCO was supplied in a white flake form. The surfactant, linear alkylbenzene sulphonate acid (HLAS), was diluted by distilled water and neutralized with sodium hydroxide solution to pH=7.5±0.5 to form sodium linear alkylbenzene sulphonate (NaLAS). The concentration of NaLAS is 16.7 wt%. The method of preparing the surfactant is similar to that used in industrial applications [1]. A comprehensive study of various surfactants was outside the scope of this work.

Preparation of samples

HCO-in-water emulsions were prepared as follows: (i) 4 g HCO was added into 96 g NaLAS solution; (ii) the above mixture was melted in a 250ml round bottom flask at

92°C in an oil bath and then stirred with a mechanical stirrer at 300 rpm to disperse the oil phase into water by mediation of surfactant; (iii) after holding 5 minutes to remove the crystal memory [1, 22], the emulsion was cooled in the oil bath under 300 rpm mechanical agitation until the temperature of final crystal suspension reached room temperature. The crystal suspension was stored at room temperature and remained stable for more than a month. The HCO suspension could be easily withdrawn with a pipette and re-melted to form emulsions. The droplet size distribution of emulsions prior to crystallization has been studied previously [3]. Based on microscopic observation, flocculation may happen before crystallization, but coalescence rarely occurred. However, coalescence may occur during the crystallization process.

Polarized light microscopy (PLM)

A polarized light microscope (Olympus, Japan) with reflected cross polarized light was used for crystal morphology observation at 20 × magnification using a Linkam Hot Stage TM94 (Linkam Scientific, Surry, UK) to quantify the effects on crystallization due to heating and cooling of oil-in-water emulsions. A sealed sample cell comprised of a round cover glass with the thickness of 0.17mm and diameter of 18mm (Fisher Scientific, Canada), a silicon wafer (UniversityWafer, USA) and a stainless supporting ring with a height of 0.5mm used as spacer created a sample cell to load emulsions. The sample cell was sealed with high vacuum silicon grease (Dow Corning, USA) avoiding contact between the emulsion samples and grease. A digital camera (Olympus, USA) was used to take pictures during the crystallization process. The crystal numbers were counted and then the sizes were measured by ImageJ (NIH, USA). Three experiments were performed and the average value and standard deviation of the measured variables were calculated for statistical purposes.

Differential scanning calorimetry (DSC)

Crystallization kinetics measurements by DSC are well known [6-9]. TA Q200 (TA Instrument, New Castle, DE, USA) differential scanning calorimeter was used to characterize the thermal behavior during the crystallizing of emulsions and melting of HCO crystals. Prior to use, indium (T_{on}=155°C) and n-Hexatriacontane (T_{on}=76.1°C) were used for temperature calibration. The heat flow due to phase changes was calibrated by pure indium. An empty hermetical aluminum pan covered with a lid was used for baseline calibration. Approximately 5-10 mg samples were introduced into the DSC hermetically sealed aluminum pans. The samples were first heated to 92°C at the rate of 10°C/min and held for 5 minutes to erase the crystal memory [1, 22] before cooling. A cooling rate of 40°C/min was used to bring the sample temperature to the target isothermal temperatures: 55°C, 58°C, 68°C and 70°C. An isothermal hold time of 40 minutes was applied at the target temperature.

The onset of crystallization was obtained by DSC [23] from the tangent point of the exothermic peak and baseline and microscopy observation of the appearance of the first HCO crystal. The induction time (τ_i) for isothermal crystallization was the time period between the onset of crystallization and time to reach the target isothermal temperature. The melting points of fibers and rosettes are similar [2], and the highest melting point of 84°C is used as the melting point for the mixed crystal system.

Each of the kinetics models was fitted to the DSC experimental data using root-mean-square-error (RMSE) as a measure of best fit.

Results and discussions

Growth rate

Figure 1 shows the growth process of HCO crystals as a function of hold time at the isothermal target temperature. Mean crystal sizes of rosettes were measured and plotted versus time at all four isothermal hold temperatures, as shown in Figure 2. The growth rate of rosettes is linear at the initial stage and then reached a plateau. The linear regions were estimated by the observation. The growth rates for the initial stage were obtained by fitting the following linear equation

$$d_3 = \dot{l}(t - \tau_{PLM}) \tag{18}$$

where τ_{PLM} is the induction time obtained from the polarized light microscope study as shown in Figure 2. It was found that the higher the isothermal hold temperature, the lower the growth rate due to the lower supercooling. Wright et al. [10] suggested that estimated growth kinetics could be different using different measuring techniques. However, the growth time and final sizes of crystals obtained by DSC (the sample was taken out to the microscope from the DSC pan) and microscopy were similar, which allows us to incorporate the linear growth rate term as a known parameter to the full Avrami model [17-18].

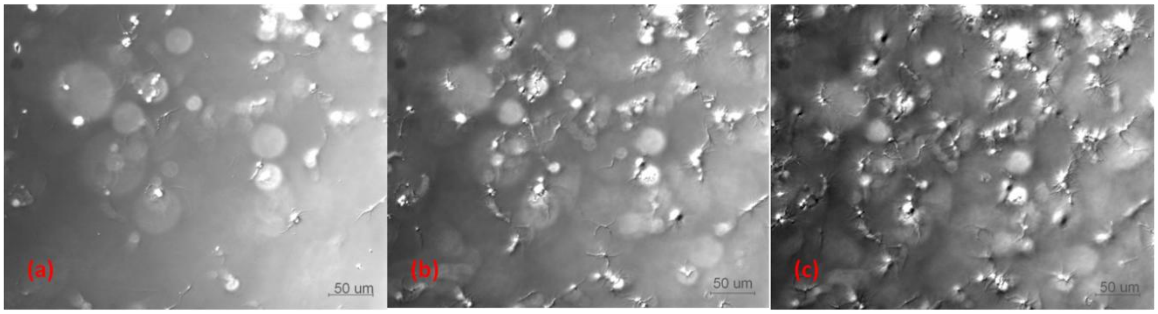

Fig. 1 Polarized light microscope images showing the growth of rosettes at the isothermal temperature of 70°C at different hold time (a) 10 min; (b) 13 min; (c) 34 min.

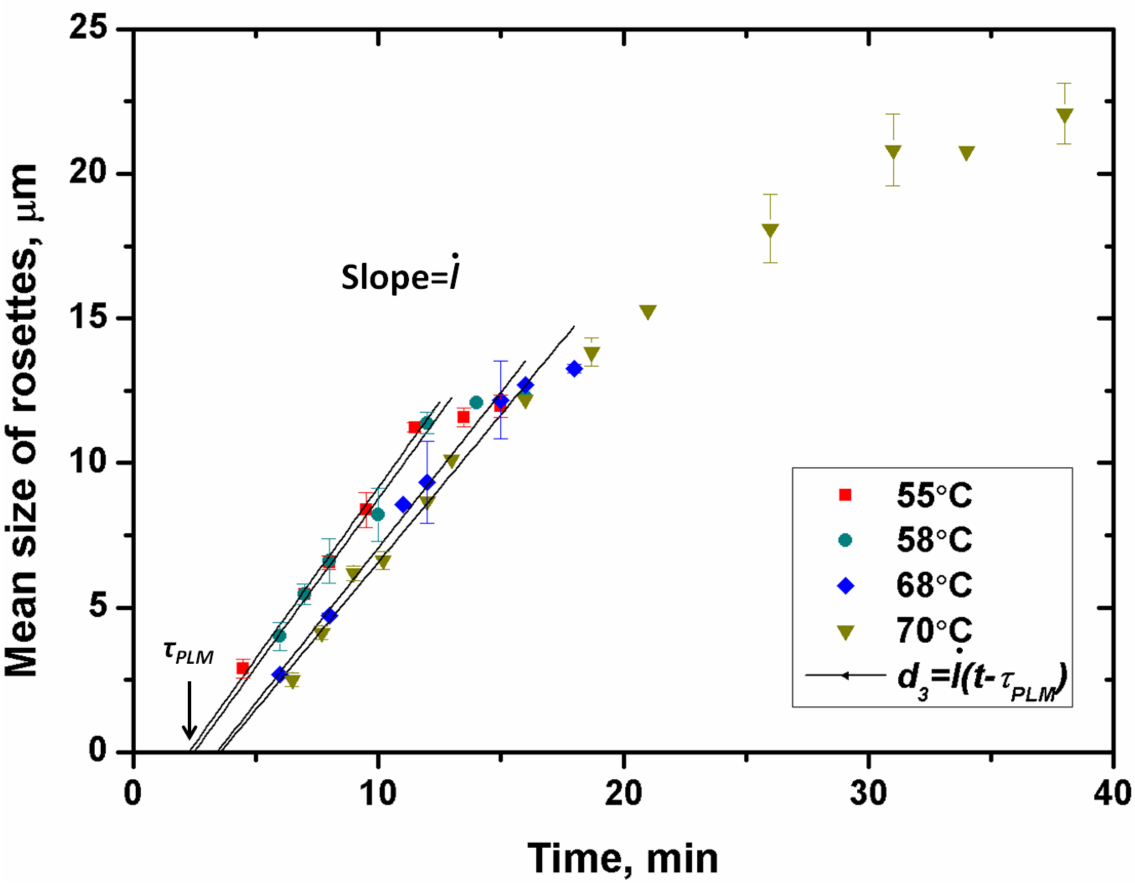

Fig. 2 The relation between mean size of rosettes and the time at isothermal temperatures of 55°C, 58°C, 68°C and 70°C.

In Table 1, the dimensions of rosettes and fibers at the end of crystallization are shown. It was found that the mean size of rosettes is largest at 70°C and smallest at 55°C due to lower supercooling at 70°C that induced a lower nucleation rate.

Table 1 Growth rate and induction time obtained by microscopy of rosettes, and final dimensions of rosettes and fibers at different crystallization temperatures.

Crystallization temperature (°C)	Rosette			Fiber	
	d_3 (μm)	$\dot{l}$ (μm/min)	τ_{PLM} (min)	d_1(μm)	L(μm)
55	11.96±2.80	1.18	2.27	2.65±0.40	19.13±0.91
58	12.28±5.90	1.16	2.48	1.59±0.02	15.12±1.28
68	13.26±6.95	1.07	3.42	1.77±0.17	15.14±0.62
70	22.08±10.61	1.02	3.56	2.07±0.15	25.96±6.69

Note: the number after "±" represents the standard deviation of size distribution.

Note: very few fibers were obtained at the isothermal temperature of 68°C and 70°C.

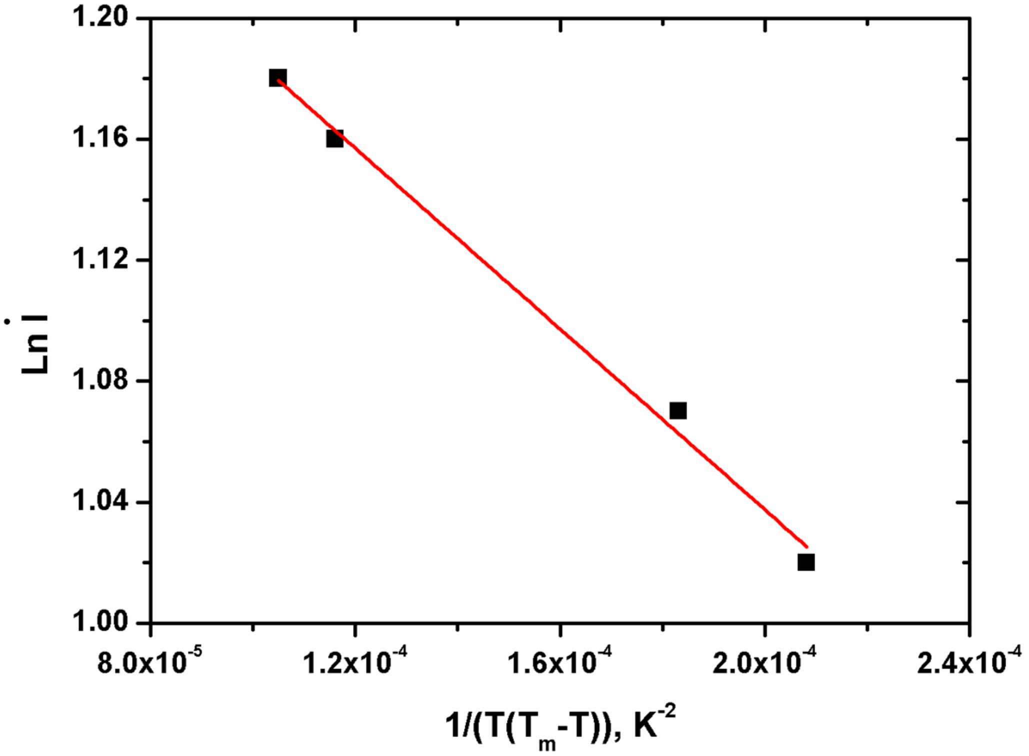

Fig. 3 Application of Hoffman-Lauritzen theory to model spherulitic growth of rosettes. The units of linear growth rate of rosettes ($\dot{l}$) is μm/min.

Hoffman-Lauritzen model was developed to describe the linear spherulitic growth rate of TAGs [16, 24] and a linear relation was expected when plotting $\ln \dot{l}$ and $1/(T(T_m - T))$. In Figure 3, it is clearly shown that a linear model described the data well (R^2=0.992) the logarithm of the linear growth rate of rosettes as a function of the driving force term. This linear relation also indicates a surface nucleation growth mechanism dominates the growth of rosettes during the whole range of isothermal temperature [25] although the growth of rosettes could happen either within one droplet or through coalescence between droplets [3].

Overall crystallization kinetics and the Avrami model

For the given cooling rate of 40°C/min, no significant crystallization likely occurred before reaching the isothermal temperature. DSC exothermic curves versus time under the isothermal temperatures from 55°C to 70°C are shown in Figure 4. On the basis of the DSC exothermic curve in Figure 5, the degree of crystallization versus time is obtained at different isothermal temperatures. As shown in Figure 5, sigmoid shape of crystallization curve reflects the overall crystallization, including nucleation, growth and crystal impingement effect, which slowed the growth [15].

The start point at the beginning of the crystallization peak corresponds to induction time for nucleation listed in Table 1. It was shown that the higher the crystallization temperature, the greater the induction time, due to less supercooling which is the driving force to nucleation. The induction time is inversely proportional to nucleation rate and increases with the crystallization temperature. The induction time obtained by microscopy shown in Table 1 is more rapid than obtained by DSC at the same crystallization temperature. Kawamura [8] suggested this phenomenon could be due to the difference in the sample weight and configuration, and the definition of the induction time.

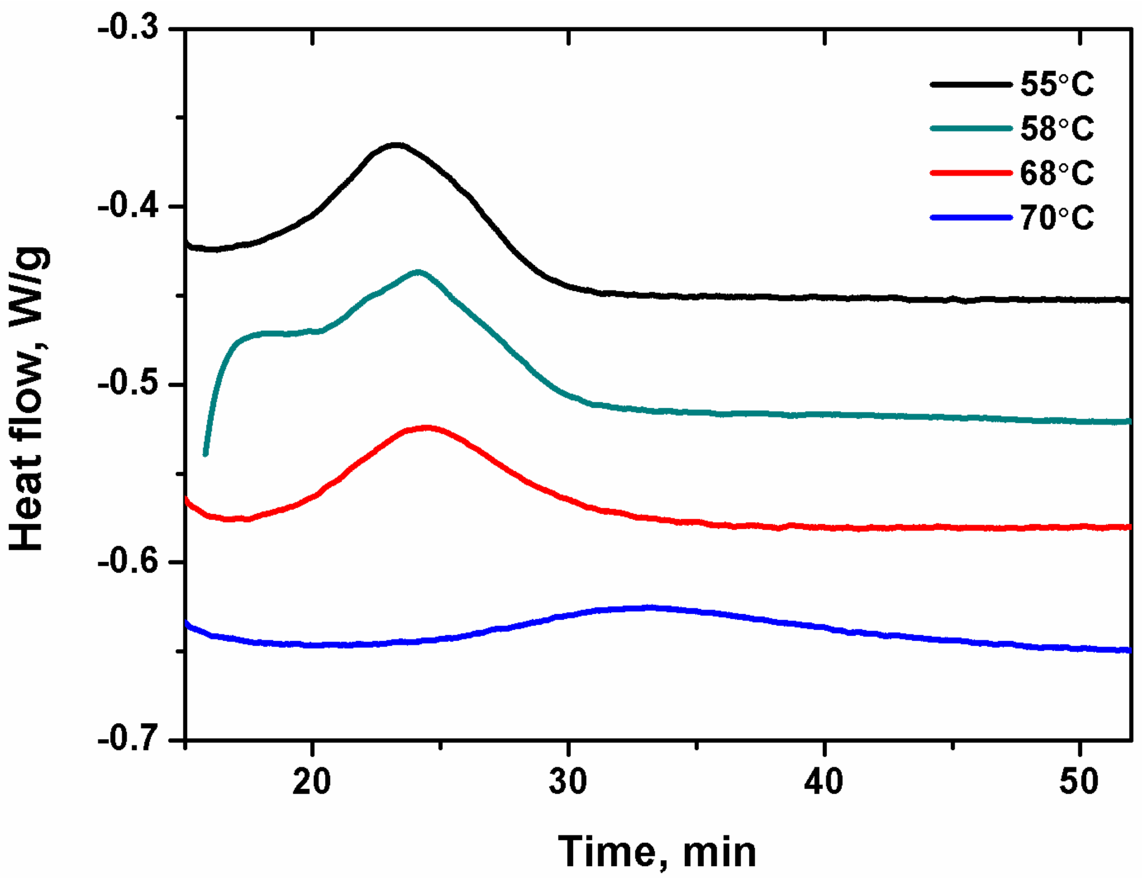

Fig. 4 Crystallization curves by DSC at different isothermal temperature.

The half time of crystallization ($t_{1/2}$), which is the time used to achieve half of the total degree of crystallization, reflects the crystallization rate [26] as shown in Table 2. It is found that half time of crystallization decreases with the decrease of crystallization temperature from 70°C to 55°C. Also, there is large decrease in $t_{1/2}$ from 70°C to 68°C.

Table 2 Induction time, half time of crystallization and number proportion of morphologies at different crystallization temperature.

Temperature (°C)	55	58	68	70
τ_i (min)	2.39±0.50	3.05±0.23	3.34±0.27	5.88±0.43
$t_{1/2}$ (min)	9.55±0.07	9.95±0.15	11.43±0.06	20.57±0.43
Rosette (%)	31.3±0.2	62.9±2.1	92.5±2.2	98.4±0.2
Fiber (%)	68.7±0.2	37.1±2.1	7.5±2.2	1.6±0.2

Note: the number after "±" represents the standard deviation.

Table 2 shows the proportions of each crystal morphology. The final number fraction of each morphology is used to calculate the volume fraction of each based on Eq. 16 and Eq. 17. In Table 3, the modified Avrami model shows the smallest value of RMSE, showed the best fit to DSC results. It is also found that RMSE for 3-D Avrami model exhibits the second smallest value for crystallization occurred at 68°C and 70°C. This is because three-dimensional rosettes take up almost all the proportion of the final crystal morphologies. Fitted parameters in the models are also shown in Table 3. For full Avrami models, initial number of nuclei N_0 and probability of growth p are the two fitted parameters; while constant k and exponent n are the two fitted parameters for approximated Avrami model. Padar et al. [21] suggested that N_0 and p increased with the increase of the supercooling. We found that the trend of p for the modified Avrami model coincided with the conclusions of Padar et al., but that the trend for N_0 was opposite and the reason for this was not clear. For 1-D fibrous and 3-D spherulitic growth with sporadic nucleation, the Avrami exponent is expected to be between 2 and 4, and increase with the crystallization temperature due to the increasing proportion of 3-D spherulitic growth. Although the Avrami exponent n shown in Table 3 is between 2 and 4, n does not increase as expected. Therefore, in this situation the Avrami exponent does not account for the nucleation and the dimension of growth well [17-18].

Table 3 Values of parameters and RMSE of models.

Temperature (°C)	Models	Parameters				RMSE
		N_0 (ml^{-1})	p (min^{-1})	k (min^{-n})	n	
55	1D	5.35×10^{11}	5.11×10^{-6}	—	—	0.9726
	3D	1.58×10^{8}	5.06×10^{-4}	—	—	0.2290
	Approximate	—	—	1.81×10^{-3}	2.99	0.2008
	Modified	1.40×10^{7}	0.141	—	—	0.0273
58	1D	7.51×10^{11}	4.37×10^{-6}	—	—	1.9531
	3D	2.44×10^{8}	4.44×10^{-4}	—	—	1.2227
	Approximate	—	—	6.55×10^{-3}	2.51	0.4289
	Modified	1.75×10^{7}	0.153	—	—	0.0090
68	1D	4.01×10^{11}	4.90×10^{-6}	—	—	0.6081
	3D	2.50×10^{5}	1.98	—	—	0.1804
	Approximate	—	—	1.70×10^{-3}	2.81	0.1120
	Modified	4.66×10^{9}	0.0108	—	—	0.0139
70	1D	2.58×10^{11}	2.53×10^{-6}	—	—	0.6976
	3D	3.45×10^{5}	0.022	—	—	0.1746
	Approximate	—	—	3.70×10^{-4}	2.80	0.1720
	Modified	2.97×10^{9}	0.0559	—	—	0.0145

The modified Avrami model fits the experiments best as shown in Table 3 and the visual comparisons are shown in Figure 5. Campbell et al. [27] suggested that the Avrami model did not account for the droplet size distribution, but was likely skewed toward the behavior of large droplets (1.264±0.437 μm) for both emulsified lard and palm stearin/canola oil. This is because the larger droplet size may contain more impurities, increasing the likelihood for the occurrence of a heterogeneous nucleation in large droplets as in the bulk. For our emulsion system, the mean size of droplet is 36.34 μm [3], but the mean crystal size crystallized in the bulk HCO is less than 30 μm (micrographs are not shown). This evidence provides the probability of using the Avrami model regardless of the droplet size distribution issue. Moreover, the good fit (R^2>0.995) shown in Figure 5 implied that the Avrami model works well on modeling the crystallization kinetics of emulsified HCO. However, there is still a systematic deviation at the end of the crystallization. This is probably attributed to collision between different morphologies. In the modified Avrami model, the fiber-fiber and rosette-rosette collisions are separated, while in fact the collisions could also occur between fiber and rosette.

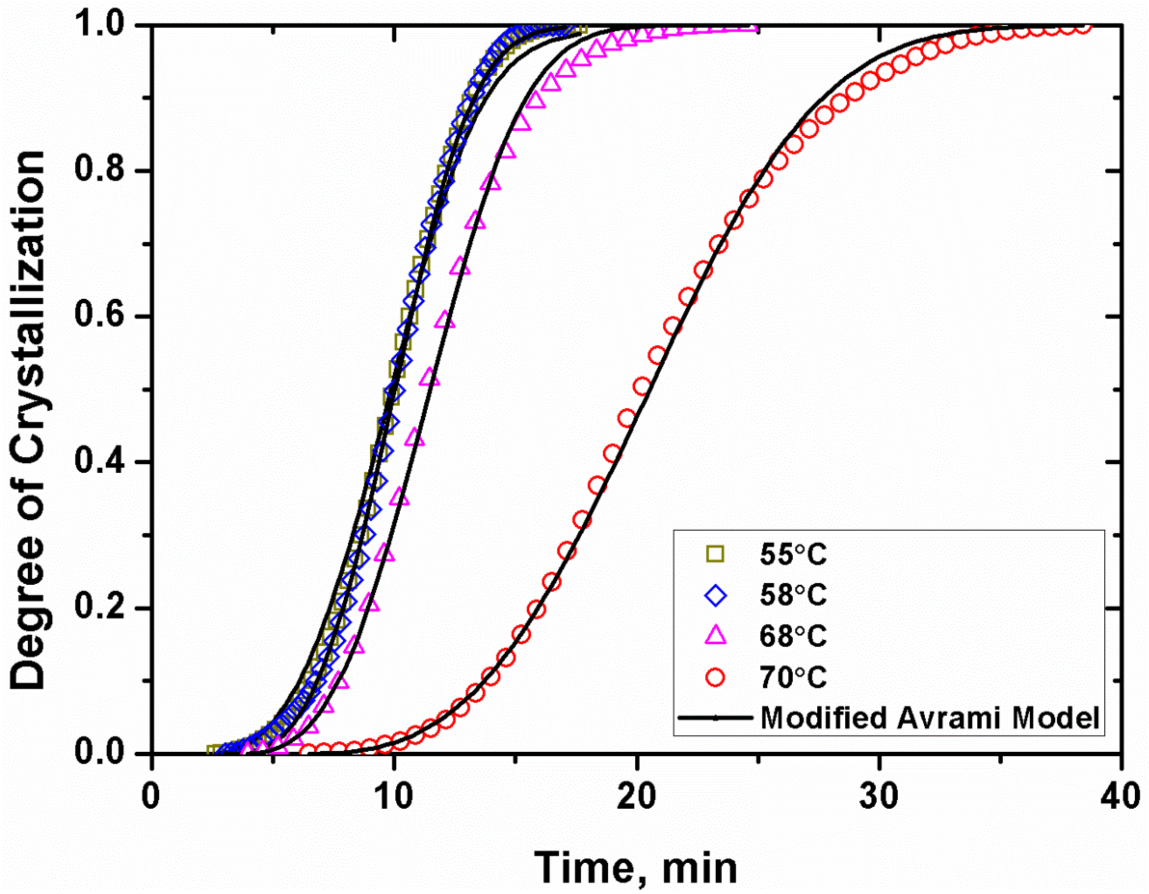

Fig. 5 Comparisons between experiments and modified Avrami models.

Conclusions

The kinetics of isothermal crystallization in the presence of mixtures of crystal morphologies have been captured by DSC and microscopy and modeled by a modified Avrami model. The induction time of nucleation increased with increased crystallization temperature, indicating lower supercooling provides lower driving force to crystallization. The linear crystal growth rate at the initial stage of crystallization decreases with increased isothermal temperature. The overall crystallization kinetics is well fitted by the modified Avrami model which introduces the volume fraction of each morphology.

Acknowledgements

We thank Natural Science and Engineering Research Council of Canada (NSERC) for partial support of this work. We also thank Dr. Kari Dalnoki-Veress, of the Department of Physics at McMaster University, for facilitating this work through the use of the hot-stage microscope.

References

[1] Goddinger D, Nordende K, Schroeder T (2009) Antidandruff shampoo. U.S. Patent 2009/0169644 A1.

[2] Yang D, Hrymak AN (2011) Crystal morphology of hydrogenated castor oil in the crystallization of oil-in-water emulsions: Part 1. Effect of temperature. Ind Eng Chem Res 50: 11585-11593.

[3] Yang D, Hrymak AN (2011) Crystal morphology of hydrogenated castor oil in the crystallization of oil-in-water emulsions: Part 2. Effect of shear. Ind Eng Chem Res 50: 11594-11600.

[4] Hartel RW (2001) Crystallization in Foods, Food Engineering Series. Aspen Publishers, Inc., USA.

[5] Marangoni AG, Narine S (2002) Physical Properties of Lipids. Marcel Dekker, New York, USA.

[6] Metin S, Hartel RW (1998) Thermal analysis of isothermal crystallization kinetics in blends of coca butter with milk fat or milk fat fractions J Am Oil Chem Soc 75: 1417-1624.

[7] Foubert I, Vanrolleghem PA, Dewettinck K (2003) A differential calorimetry method to determine the isothermal crystallization kinetics of cocoa butter. Therm Acta 400: 131-142.

[8] Kawamura K (1979) The DSC thermal analysis of crystallization behavior in palm oil. J Am Oil Chem Soc 56: 753-758.

[9] Lorenzo AT, Arnal ML, Albuerue J, Muller AJ (2007) DSC isothermal polymer crystallization kinetics measurements and the use of Avrami equation to fit the data: guideline to avoid common problems. Polymer Testing 26: 222-231.

[10] Wright AJ, Narine SS, Marangoni AG (2000) Comparison of experimental techniques used in lipid crystallization studies. J Am Oil Chem Soc 12: 1239-1242.

[11] Mazzanti G, Marangoni AG, Idziak SHJ (2009) Synchrotron study on crystallization kinetics of milk fat under shear flow. Food Res Int 42: 682-694.

[12] Povey MJW (1995) Ultrasound studies of shelf-life and crystallization. In: Dickinson E (eds) New Physico-Chemical Techniques for the Characterization of Complex Food Systems. Chapman & Hall, London, pp 196-212.

[13] Zhao J, Reid DS (1994) Thermal studies on the crystallization kinetics of triglycerides and milk fat by DSC. Therm Acta 246: 405-416.

[14] Smith K, Cain FW, Talbot G (2005) Kinetics analysis of nonisothermal differential scanning calorimetry of 1,3-dipalmitoyl-2-oleoylglycerol. J Agric Food Chem 53: 3031-3040.

[15] Foubert I, Dewettinck K, Vanrolleghem PA (2003) Modeling of the crystallization kinetics of fats. Trend Food Sci Technol 14: 79-92.

[16] Himawan C, Starov V, Stapley A (2006) Thermodynamic and kinetic aspects of fat crystallization. Adv Colloid Int Sci 122: 3-33.

[17] Avrami M (1939) Kinetics of phase change, 1. General theory. J Chem Phys7: 1103-1112.

[18] Avrami M (1940) Kinetics of phase change, 2. Transformation-time relation for random distribution of nuclei. J Chem Phys 8: 212-224.

[19] Kloek W, Walstra P, Vliet Ton van (2000) Crystallization kinetics of fully hydrogenated palm oil in sunflower oil mixtures. J Am Oil Chem Soc77: 389-398.

[20] Foubert I, Vanrolleghem PA, Vanhoutte B, Dewettinck K (2002) Dynamic mathematical model of the crystallization kinetics of fats. Food Res Int 35: 945-956.

[21] Padar S, Jeelani SAK, Windhab EJ (2008) Crystallization kinetics of coca fat systems: experiments and modeling. J Am Oil Chem Soc 85: 1115-1126.

[22] Spicer PT, Hartel RW (2005) Crystal comets: dewetting during emulsion droplet crystallization. Aust J Chem 58: 655-659.

[23] Toro-vazquez J, Herrera-coronado V, Dibildox-alvarado E, Charo-alonso M, Gomez-aldapa C (2002) Induction time of crystallization in vegetable oils, comparative measurements by differential scanning calorimetry and diffusive light scattering. J Food Sci 67: 1057-1065.

[24] Kellens M, Meeussen W, Reynaers H (1992) Study of the polymorphism and the crystallization kinetics of tripalmitin: A microscopic approach. J Am Oil Chem Soc 69: 906-911.

[25] Rousset Ph, Rappaz M (1996) Crystallization kinetics of the pure triacylglycerols glycerol-1,3-dipalmitate-2-oleate, glycerol-1-palmitate-2-oleate-3-stearate, and glycerol-1,3-distearate-2-oleate. J Am Oil Chem Soc 73: 1051-1057.

[26] Wright AJ, Hartel RW, Narine SS, Marangoni AG (200) The effect of minor components on milk fat crystallization. J Am Oil Chem Soc 77: 463-475

[27] Campbell SD, Goff HD, Rousseau D (2004) Modeling the nucleation and crystallization kinetics of a palm stearin/canola oil blend and lard in bulk and emulsified form. J Am Oil Chem Soc 81: 213-219.

Chapter 5 Rheology of Aqueous Dispersions of Hydrogenated Castor Oil

In this chapter, I performed all the experiments, characterization and manuscript preparation. Dr. Andrew Hrymak supervised this work and participated in the edits on the manuscript. This chapter is being developed for a journal submission.

Abstract: Three major hydrogenated castor oil crystal morphologies have been observed: fiber, rosette and irregular crystal. Due to the difficulty in obtaining samples with a single crystal morphology, rheological studies of suspensions containing mixtures of the three morphologies in a aqueous solution have been undertaken. The viscometry of dilute suspensions has shown that the magnitude of intrinsic viscosity is dominated by the fraction of a crystal morphology type, i.e. fiber > rosette > irregular crystal. A modified Farris model was fitted to the rheology data from mixtures of crystal morphology with interacting particles. A yield stress exists for concentrated suspensions followed by a shear thinning behavior with the increase of shear rate. A power-law relation has been found between yield stress and total particle volume fraction, and a constant exponent of 1.5 has been obtained regardless of crystal morphology.

Keywords: suspension rheology; morphology; hydrogenated castor oil; fiber; rosette

Introduction

The dispersions of hydrogenated castor oil (HCO), i.e. tri-12-hydroxystearin, crystals are widely used as rheological modifier in paints, cosmetics and household products (Magauran et al. 1994, Goddinger et al. 2009). Three HCO crystal morphologies have been observed: fiber, rosette and irregular crystals (Yang and Hrymak 2011, Yang et al., 2011). Different combinations of the fractions of the three morphologies can be produced by controlling the crystallization temperature, shear rate and time. The purpose of this work is to investigate the effect of HCO crystal morphology on aqueous suspension rheology. However, it is difficult to separate a single morphology from the mixtures of morphologies. Therefore, our studied material system is the mixture of morphologies.

The suspension rheology of hard spheres has been extensively studied, but nonspherical particulate dispersions are widely used (Mewis and Wagner 2009).

Nonspherical particles are often characterized by one dimension, which is significantly different from another orthogonal direction. For example, two simplified non-spherical shape models are rotational ellipsoids and circular cylinders. The shape factor can be quantified by the aspect ratio, *r*, defined as the ratio of maximum Feret diameter (*L*) divided by the minimum Feret diameter (*D*) (Merkus et al. 2009). Therefore, elongated particles, such as fibers and rods have an aspect ratio $r >> 1$, and “flaky” particles $r << 1$. The aspect ratio provided a convenient way to quantify the effect of dimensions of nonspherical particles in the rheology of suspensions (Brenner 1974; Petrie 1999; Petrich et al. 2000). Aspect ratios of particles usually vary with the particle size distribution. However, an average aspect ratio which is calculated from the overall particle distribution is commonly used (Pabst 2006). The three concentration regimes are also quantified by comparing the volume fraction (ϕ) of the dispersion and aspect ratio of particles (Solomon and Spicer 2010). The regimes are typically delineated as follows: dilute regime, $\phi << 1/r^2$; semi-dilute regime, $1/r^2 << \phi << 1/r$; and concentrated regime, $\phi >> 1/r$.

Farris (1968) modeled the relative viscosity of bimodal mixtures and then was extended to multimodal suspensions. In the bimodal system, a very large size ratio between coarse and fine particles is required so that interactions between the two sizes of particles are neglected. Therefore, suspensions of fine particles can be assumed to be acting as the suspending media of coarse particles. The Farris model was also successfully employed to deal with bimodal system with mixtures of morphologies under the assumption of non-interacting particles by Mor et al. (1996) and Marti et al. (2005). Based on the Farris model, the relative viscosity of a bimodal suspension, η_r, is expressed as

$$\eta_r = \frac{\eta}{\mu} = (\frac{\eta_f}{\mu})(\frac{\eta}{\eta_f}) = \eta_{fr}\eta_{cr} = H(\phi_f)H(\phi_c) \tag{1}$$

where η_{fr} is the relative viscosity of fines and is defined as the ratio between the viscosity of suspensions containing only fine particles (η_f) and the viscosity of the media. η_{cr} is the relative viscosity of coarse particles and is defined as the ratio of the viscosity of the suspension after adding coarse particles (η) to the viscosity of suspensions containing just fines (η_f). *H* is the function between relative viscosity of fine and coarse particles and the volume fractions of each type. A Krieger-Doughty (1972) type of function was used by Farris (1968) and Marti et al. (2005) to represent *H*. As $H(\phi) = 1 \text{ when } \phi = 0$, Eq. (1) is valid for all values of ϕ.

Zaman and Moudgil (1998) modified the Farris model for low size ratios (< 2.5) of bimodal particulate systems, and particle-particle interactions were considered. $G(\phi_c)$, a function of volume fraction of coarse particles involving inter-particulate interactions, was used to replace $H(\phi_c)$ and expressed as

$$G(\phi_c) = \frac{\eta_r}{H(\phi_f)} \tag{2}$$

If the fine particles were replaced by the same volume fraction of coarse particles, and the replaced coarse particles were the same with the subsequent added coarse particles, then

$$G_m(\phi_c) = \frac{\eta_{r(mc)}}{G_m(\phi_f)} \tag{3}$$

where the subscript *m* denotes a monodisperse system. Because only coarse particles exist in the suspensions, $\eta_{r(mc)}$ is fixed for fixed total volume fraction regardless of the variation of ϕ_f. Therefore, the presence of fines differentiates $G(\phi_c)$ and $G_m(\phi_c)$, and this difference can be eliminated by normalizing the data

$$J(\phi_f) = \frac{G(\phi_c)}{G_m(\phi_c)} \tag{4}$$

If an empirical correlation of $J(\phi_f)$ is substituted into Eq. (4), combined with Eq. (2) and (3), the relative viscosity as the function of ϕ_f at different total volume fraction of particles can be expressed as

$$\eta_r = \frac{J(\phi_f)\eta_{r(mc)}H(\phi_f)}{G_m(\phi_f)} \tag{5}$$

In this paper, the relationship between mixtures of crystal morphologies and rheology were extensively investigated in both dilute and concentrated regimes.

Experimental

Materials

Hydrogenated castor oil (BP Chemicals Ltd.), tri-12-hydroxysterin, crystals were made by controlling the temperature (Yang and Hrymak, 2011) and shear (Yang et al., 2011). HCO crystals have a density of 0.99 g/cm^3, which is close to water. The HCO was dispersed in an aqueous solution of 16.7 wt% sodium linear alkylbenzene sulfonate (NaLAS), and the pH of the surfactant was kept at 7.5±0.5. The density of pure NaLAS is approximately 1.03 g/cm^3 at 25°C. The volume fraction of HCO was estimated from the weight fraction by considering the density of the dispersion as 1 g/cm^3.

Preparation of HCO dispersions

4 g HCO was added into 96 g NaLAS solution in a 250ml round bottom flask in an oil bath, and then the mixture was melted at 92°C (Goddinger et al. 2009, Spicer and Hartel 2005). Mechanical stirring at 250 rpm was used to disperse the oil phase into water with mediation of surfactant. After holding for 5min, to remove the crystal memory, the emulsion was cooled under 250rpm mechanical agitation until the temperature of the final crystal suspension reached room temperature. Three cooling procedures, oil bath, air bath and water bath, were used to achieve crystallization as shown in Fig. 1, and three different crystal morphologies were obtained respectively as shown in Fig. 2(a), 2(b) and 2(c). However, the degree of crystallization as measured by the DSC melting curves were almost the same (error less than 3%) for the three HCO dispersions.

HCO suspensions were diluted by adding the same concentration of the water-surfactant mixture as for the original suspensions. Due to the fragility of HCO crystals, the suspensions could not be dispersed by strong ultrasonic or mechanical agitation, instead a sample shaker was used over a period of 24 hours.

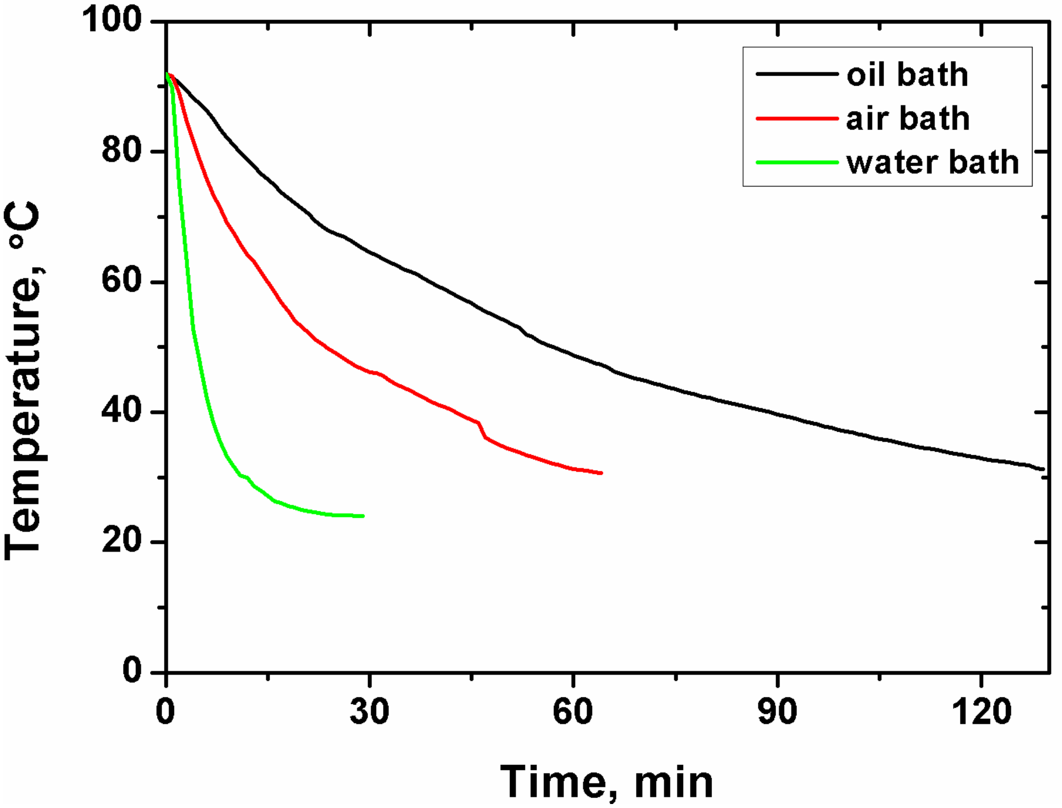

Fig. 1 Temperature-time profiles for the crystallization of oil-in-water emulsions to make HCO dispersions.

Morphology

The HCO crystal morphology was observed under transmitted polarized light microscopy (VWR Vista Vision, USA), and 40 × magnification objective. The particulate suspensions were diluted with distilled water for better observation of individual crystals as shown in Fig. 2. As the orientation of fibers affects the observed lengths, the sample between two microscopy slips was minimized to approximate a two-dimensional plane. A digital camera (VWR VistaVision, USA) was used for recording micrographs.

A JEOL 1200 EX TEMSCAN transmission electron microscope (JEOL, USA) operated at 80 kV was used for the observation of the nano-scaled crystals. Prior to observation, a drop of HCO crystal suspension was loaded on Formvar-coated (Canemco

Inc., Quebec, Canada) copper grids and dried slowly in natural air. The 4 wt% HCO suspension was diluted 10 times with 16.7 wt% of NaLAS and then 1,000 times with water to avoid the aggregation of crystals. ImageJ (NIH, USA) was used for image analysis, where more than 500 particle measurements were assembled to estimate the sizes and number fraction of each crystal morphology.

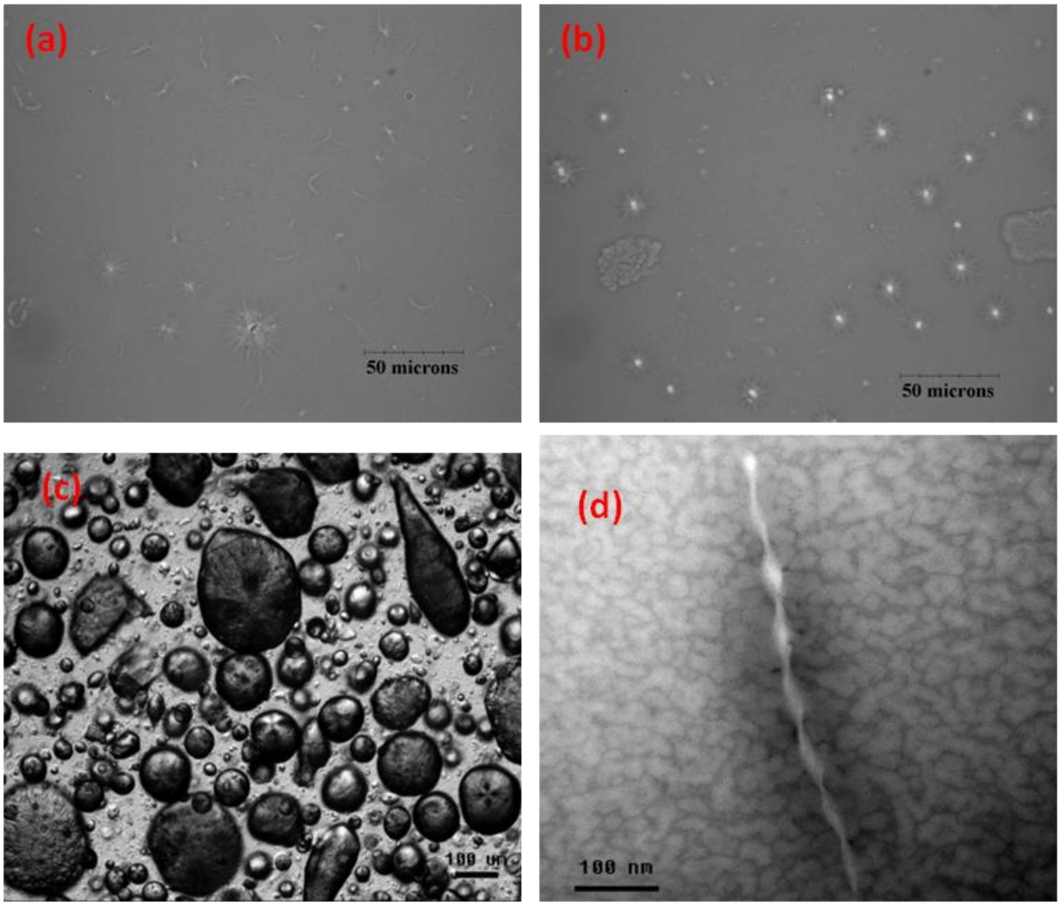

Fig. 2 HCO crystal morphology. (a) $F_{0.52}R_{0.38}I_{0.10}$ (ϕ =0.01); (b) $F_{0.16}R_{0.71}I_{0.13}$ (ϕ =0.01); (c) $F_0R_0I_1$ (ϕ =0.3); (d) nano-fibrous fragments.

Table 1 lists the number fraction of each crystal morphology type in the three different mixtures shown in Fig. 2. Based on the number fraction, the three mixtures are referred to as $F_{0.52}R_{0.38}I_{0.10}$, $F_{0.16}R_{0.71}I_{0.13}$ and $F_0R_0I_1$, where the subscript refers to the number fraction of that crystal morphology type. Table 1 also lists the size of each morphology, and it is found that the equivalent diameter and the polydispersity of the same morphology is slightly different among the three mixtures. Here we focus on the morphological effect and assume there is little effect of the observed size distribution on the rheology (Chong *et al.* 1971).

Table 1 Physical properties of HCO particles in the three suspensions.

Morphology	Parameters	$F_{0.52}R_{0.38}I_{0.10}$	$F_{0.16}R_{0.71}I_{0.13}$	$F_0R_0I_1$
Fibres	n_F	0.52	0.16	0
	L, µm	12.2±6.7	11.5±4.5	-
	D, µm	0.91±0.20	0.79±0.22	-
	r	15.1±6.6	14.5±6.8	-
Rosettes	n_R	0.38	0.71	0
	d_R, µm	14.9±6.3	13.5±7.4	-
Irregular	n_I	0.10	0.13	1
	d_I, µm	10.9±6.8	16.3±10.4	43.8±40.4

n_F, n_R and n_I stand by the number fraction of each morphology.

d_R and d_I are diameters of rosettes and irregular crystals.

Nano-fibrous crystals exhibiting chirality (Kuwahara et al., 1996; Rogers et al., 2008) with the average diameter of 26.7 nm were also found in the suspensions as shown in Fig. 2(d). Thus far, it is not clear whether these are fragments broken down from rosettes or macro-fibers, or form due to primary nucleation. Through image analysis, the number ratio between nano- and micro- sized crystals was quantified to generate a volume fraction distribution as a function of crystal size of the suspension $F_{0.52}R_{0.38}I_{0.10}$ as shown in Fig. 3. By assuming rosettes as equivalent hard spheres, the volume fraction of nano-fibrous fragments was roughly calculated to be around 10^{-6} among the total amount of HCO. Therefore, in this paper, we do not consider the effect of nano-fibrous fragments on the rheology.

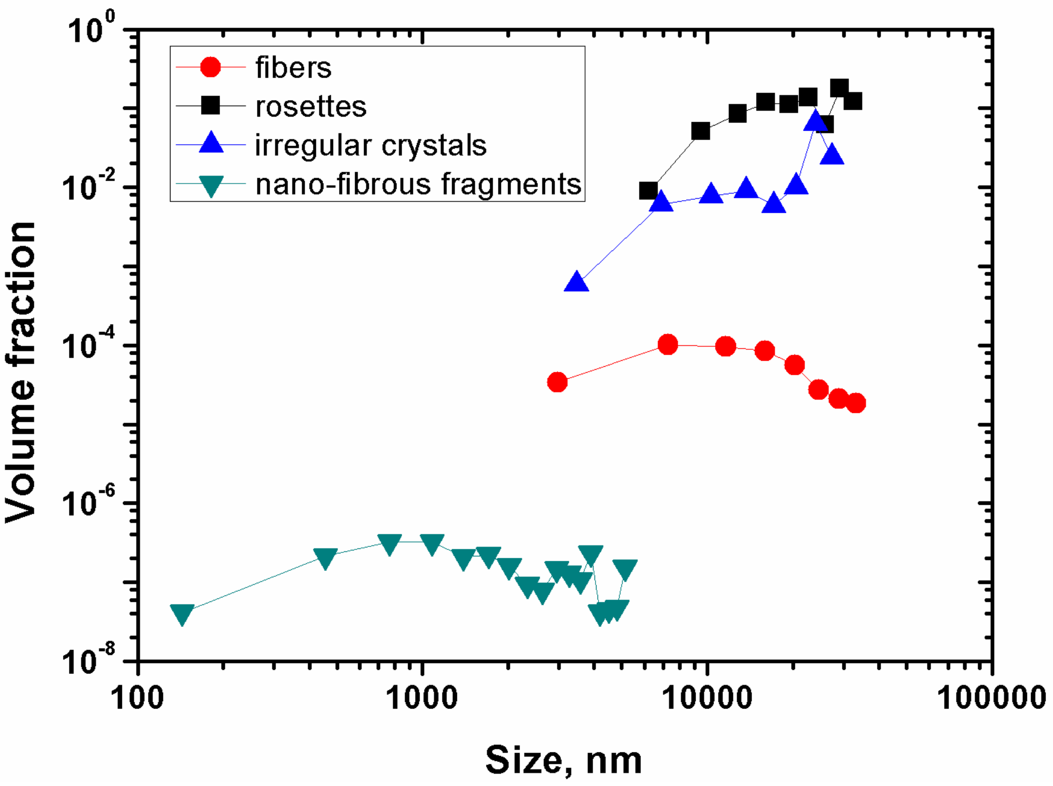

Figure 3 Volume fraction distribution versus the size for suspension $F_{0.52}R_{0.38}I_{0.10}$.

Samples $F_{0.52}R_{0.38}I_{0.10}$ and $F_{0.16}R_{0.71}I_{0.13}$ were stable for more than one month, which showed colloidal behavior (Russel *et al.* 1989) proportional to the smallest dimension of the width of fibers. However, sample $F_0R_0I_1$ with crystal dimensions several times larger than 10 μm, which is normally used as the critical size to distinguish between colloidal and noncolloidal particles (Genovese *et al*. 2007), usually exhibited phase separation over 24 hours.

Rheology

For dilute suspensions, intrinsic viscosity was obtained by Ubbelohde Viscometer (Cannon 300, Cannon Instrument Company, USA) with the capillary inner diameter of 1.27mm. The dimensions of HCO crystals (as shown in Table 1) were much smaller than the inner diameter of the capillary, so any wall effect was neglected. A rotational diffusivity (D_r) was estimated from the theory of Brenner (1967, 1974). The estimated value of D_r is of the order of magnitude of 10^{-5} s^{-1}, such that Brownian motion could be neglected (Mewis, 1994). Therefore, the rotational Peclet number *Pe*, expressed as $Pe = \dot{\gamma} / D_r$, is much greater than $(r^3 + r^{-3})$ (Leal and Hinch, 1973), which means the high-shear limit is applied in the capillary viscometry. In this study, a maximum shear rate used in capillary viscometer was calculated as 21 s^{-1} based on the geometry of the capillary and physical properties (i.e. size, density) of the HCO suspension. As fibers were axisymmetric particles, Mewis (1994) suggested that the disperse phase will orient with the flow as $Pe \to \infty$. Good agreement of the effective viscosity of the dispersions was found between capillary and rotational viscometer data.

For concentrated dispersions, rheological experiments were carried out with a controlled stress rheometer (ATS, Rheologica Instrument, USA) using the co-cylindrical Couette configuration. Steady shear viscosity was obtained by applying a stress from 0.002 to 2000 Pa. The range of the stress was divided by 30 intervals and a hold time of 10 seconds was applied at each shear stress. To make sure the measured viscosity at each shear stress was constant, viscosity data calculated at the shear rate smaller than $0.1 s^{-1}$ was abandoned. All experiments were carried out at 25°C.

Under the shear rate applied ($0.1 \sim 500\ s^{-1}$), the water-surfactant matrix showed Newtonian behavior with a constant shear viscosity of $\mu = 0.0814 \pm 0.0053$ Pa·s. This value was consistent with that obtained by Ubbelohde viscometer (0.0819±0.0001 Pa·s), which was used as the medium viscosity (μ).

Results and discussion

Shear rate dependent dilute dispersions

The intrinsic viscosity $[\eta]$ represents the average contribution of particles to the effective viscosity (η) of the suspensions when the volume fraction (ϕ) becomes infinitesimal, defined as

$$[\eta] = \lim_{\phi \to 0} \frac{\eta - \mu}{\mu \phi} \tag{6}$$

For dilute suspensions, the intrinsic viscosity has been reported to be a function of Peclet number and aspect ratio of particles (Berry and Russel 1987, Brenner 1974, Hinch and Leal 1972). In our case, $Pe >> (r^3 + r^{-3})$, a high shear limit viscosity was obtained for suspensions flowing through the capillary viscometer. From the shear dependent viscometric curves obtained from rotator viscometer using a Couette cell (data not shown), a near Newtonian behavior profile was found with $(\eta_0 - \eta_\infty)/\eta_0 < 5\%$, where η_o and η_∞ represent low and high limit shear viscosity respectively. The expression for effective shear viscosity (η_o) with interacting particles (Berry and Russel 1987) was used to estimate the high shear limit viscosity based on the small difference between low and high shear limit viscosity:

$$\eta = \mu(1+[\eta]\phi + k_H[\eta]^2\phi^2 + ...) \tag{7}$$

where k_H is the Huggins coefficient. Fig. 4 shows the intrinsic viscosity of the three dilute dispersions obtained from the intercept of Eq. (7) and the values are shown in Table 2. It is found that irregular crystals show the smallest intrinsic viscosity of 3.2, which is slightly larger than the theoretical value of 2.5 obtained by Einstein's equation for rigid spheres. The intrinsic viscosity increases to 9.8 for the rosette-rich mixture $F_{0.16}R_{0.71}I_{0.13}$, indicating rosettes exhibit higher intrinsic viscosity than irregular crystals within the range of particular size studied. As rosettes are not solid crystals, but have gaps between their branches, the actual volume occupied by a rosette is less than the excluded spherical volume. Because intrinsic viscosity is the function of actual volume fraction, rosettes show higher values than irregular crystals. $F_{0.52}R_{0.38}I_{0.10}$ exhibits the highest intrinsic viscosity because fibers have the highest aspect ratio, which produces more particle-fluid interactions.

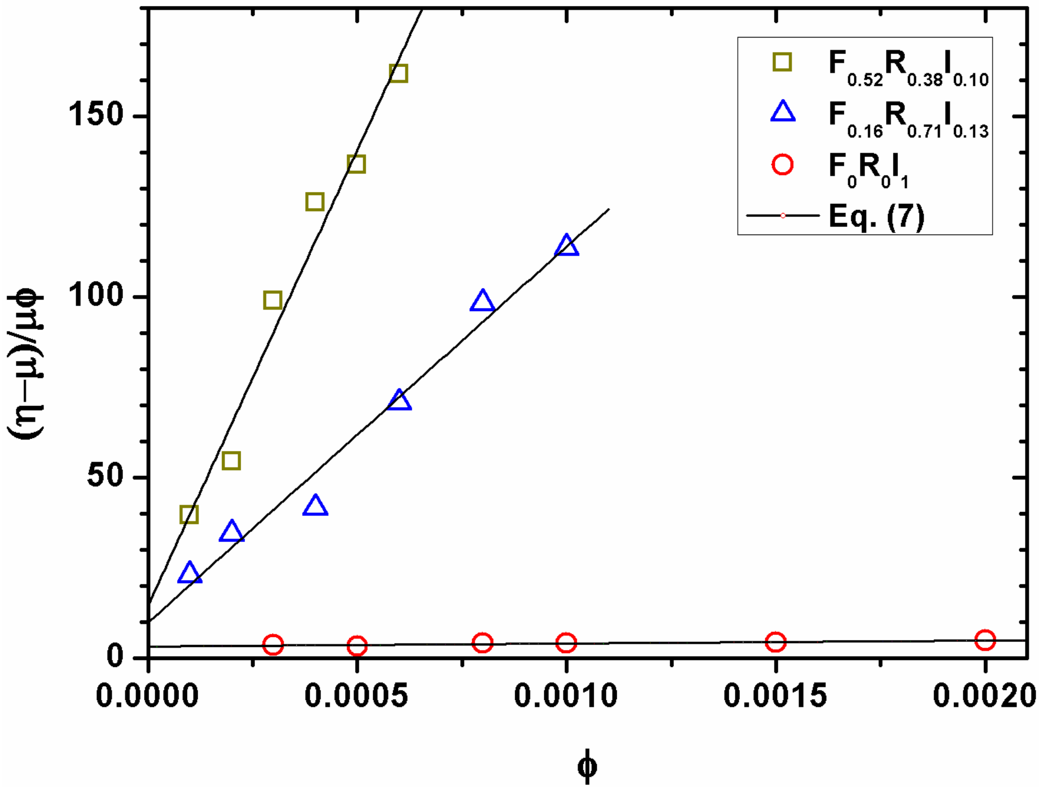

Fig. 4 Dilute suspension viscometry for different proportions of HCO crystal morphologies ($\dot{\gamma}$ ~21s^{-1}).

Table 2 Intrinsic viscosity of dilute suspensions.

Mixtures	$[\eta]$ [-]	$k_H[\eta]^2$ [-]	k_H [-]
$F_{0.52}R_{0.38}I_{0.10}$	14.5	252411	1217
$F_{0.16}R_{0.71}I_{0.13}$	9.8	104035	1083
$F_0R_0I_1$	3.2	830	81

Huggins coefficient reflects the particle-particle interactions, such as hydrodynamic and colloidal interactions (i.e. van der Waals forces, electrostatic forces), and the experimental values are listed in Table 2. It is shown that Huggins coefficient decreases from high aspect ratio fibers to low aspect ratio rosettes and irregular crystals. The values are much higher than k_H=0.4 calculated by Berry and Russel (1987) for long-slender colloidal hard rods with strong Brownian motion. Possible reasons for this discrepancy include hydrodynamic interactions caused by high shear flow or colloidal attractions between particles (Wierenga and Philipse 1996, Solomon and Boger 1998).

Modified Farris model

A modified Farris model is used to build a relationship between relative viscosity of the suspension and the volume fraction of each morphology type. In our study, a suspension with a size distribution rather than mono-sized dispersions (Table 1) is represented in the material system. Marti et al. (2005) suggested that the effect of size distribution could be treated by the effective volume fraction approach (Krieger 1972). The two suspensions, rosette-rich $F_{0.16}R_{0.71}I_{0.13}$ and fiber-rich $F_{0.52}R_{0.38}I_{0.10}$, were considered as fine and coarse particles respectively. The two suspensions were mixed at different volume ratios, but the total volume fraction of HCO was kept constant. Fig. 5 represents $J(\Phi_{F0.16R0.71I0.13})$ or $J(\phi_f)$ (obtained from Eq. (4)) as a function of volume fraction of $F_{0.16}R_{0.71}I_{0.13}$ or ϕ_f at three total volume fraction of particles. At each volume fraction, a second order polynomial equation is satisfied to fit the experimental data. Note that from Eq. (2-4), $J(\phi_f)$ equals unity at $\phi_f = 0$ and $\phi_f = 1$.

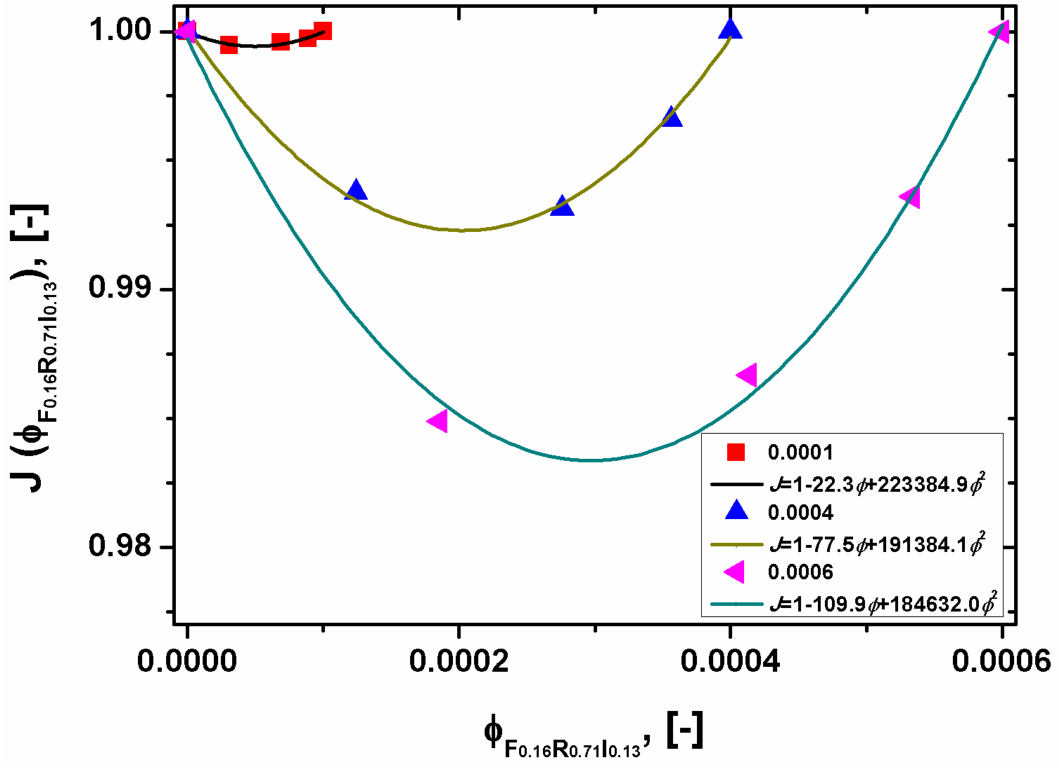

Fig. 5 $J(\phi_{F0.16R0.71I0.13})$ as a function of total volume fraction of the mixture $F_{0.16}R_{0.71}I_{0.13}$.

Zaman and Moudgil (1998) drew the conclusion that $J(\phi_f)$ was the universal function of ϕ_f regardless of total volume fraction of particles. However, Horn and Richtering (2000) found the correlation between $J(\phi_f)$ and ϕ_f were dependent on the total volume fraction of particles and suggested that the conclusion of Zaman and Moudgil (1998) was only true for specific material systems with silica particle size between 0.6 and 1.5, but could not be generalized to describe the zero shear viscosity of bimodal dispersions of smaller highly charged lattices. Therefore, it is not surprising we have found different correlations at different total volume fraction in our suspensions of much larger and mixed shaped particles.

The modified Farris model (Eq. 5) is employed to compare with experimental data and is shown in Fig. 6. A good match between observed and predicted relative viscosity is obtained. Based on the volume fraction of each morphology in the mixture of dispersions, the relative viscosity can also be represented as the function of number fraction of each morphology as shown in Fig. 6.

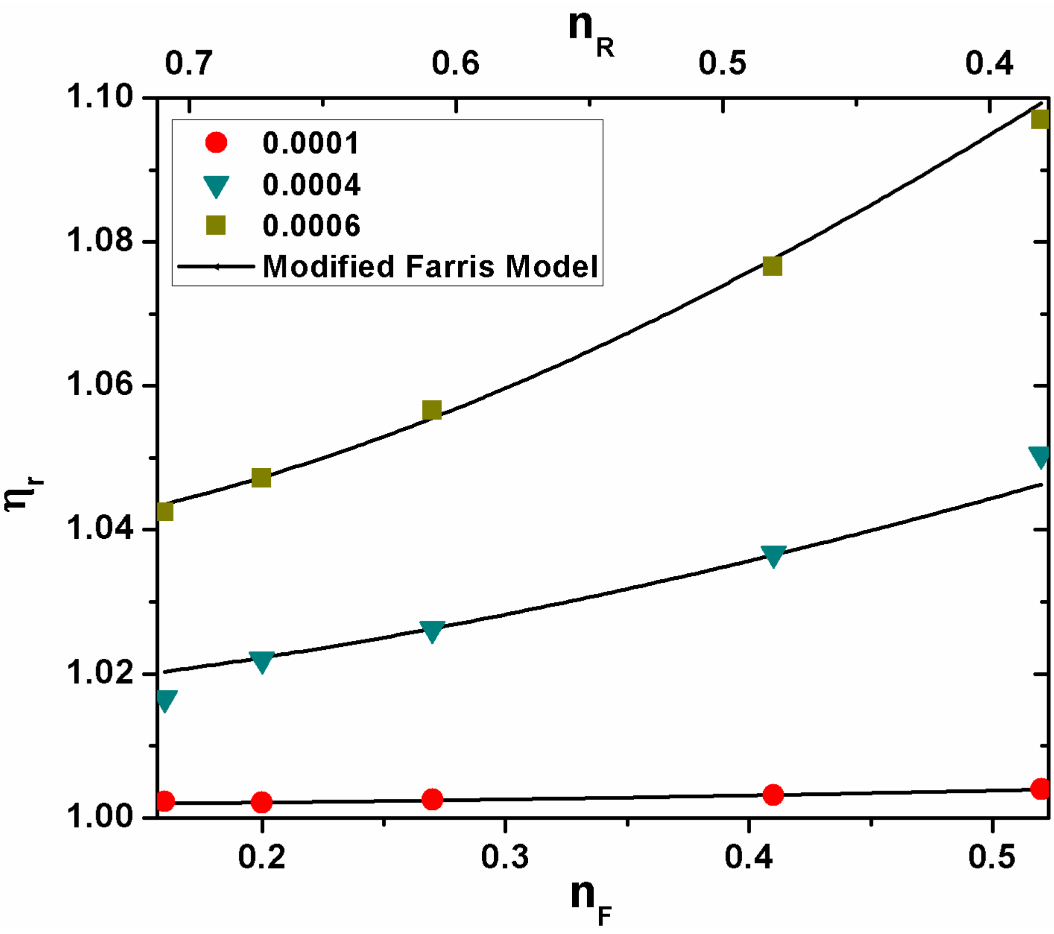

Fig. 6 Comparison between observed and predicted relative viscosity of the mixture as the function of number fraction of fibers and rosettes at different total volume fraction.

Dynamic yield stress of concentrated dispersions

The steady shear tests are performed on the three mixtures with various volume fractions and an example of viscometry curve of fiber-rich suspension are shown in Fig. 7. Within the shear stress applied, shear thinning patterns are shown in the non-dilute regime. The shear viscosity increases with increasing total particle volume fraction.

A yield stress is apparent at the concentrated regime (e.g. $\phi > 0.001$ for $F_{0.52}R_{0.38}I_{0.10}$). The concept of yield stress has some controversy (Barnes and Walters, 1985; Hartnett and Hu, 1989; Astarita, 1990) Viscoplastic models, including yield stress for steady state shear viscosity, have been extensively studied by many researchers (Macosko 1994, Larson 1999). The three parameter Herschel-Bulkley model (Zhou et al. 1998, Mueller et al. 2010) was used to fit the yield stress:

$$\tau = \tau_y + K\dot{\gamma}^n \tag{8}$$

where τ_y is the yield stress below which there is no flow or no viscosity can be measured. K is the consistency or η at $\dot{\gamma} = 1$. n is the flow index showing the degree of shear thinning ($n < 1$) or shear thickening ($n > 1$). Herschel-Bulkley model was fitted to the fiber-rich suspension $F_{0.52}R_{0.38}I_{0.10}$ as shown in Fig. 7. As an engineering reality problem (Astarita, 1990), the whole range of shear rate in Fig. 7 is used in fitting the Herschel-Bulkley model. A yield stress ($\tau_y = 10.57 Pa$) is apparent at the volume fraction of 0.04, but the estimated yield stress at a volume fraction of 0.001 ($\tau_y = 0.06 Pa$) is much smaller.

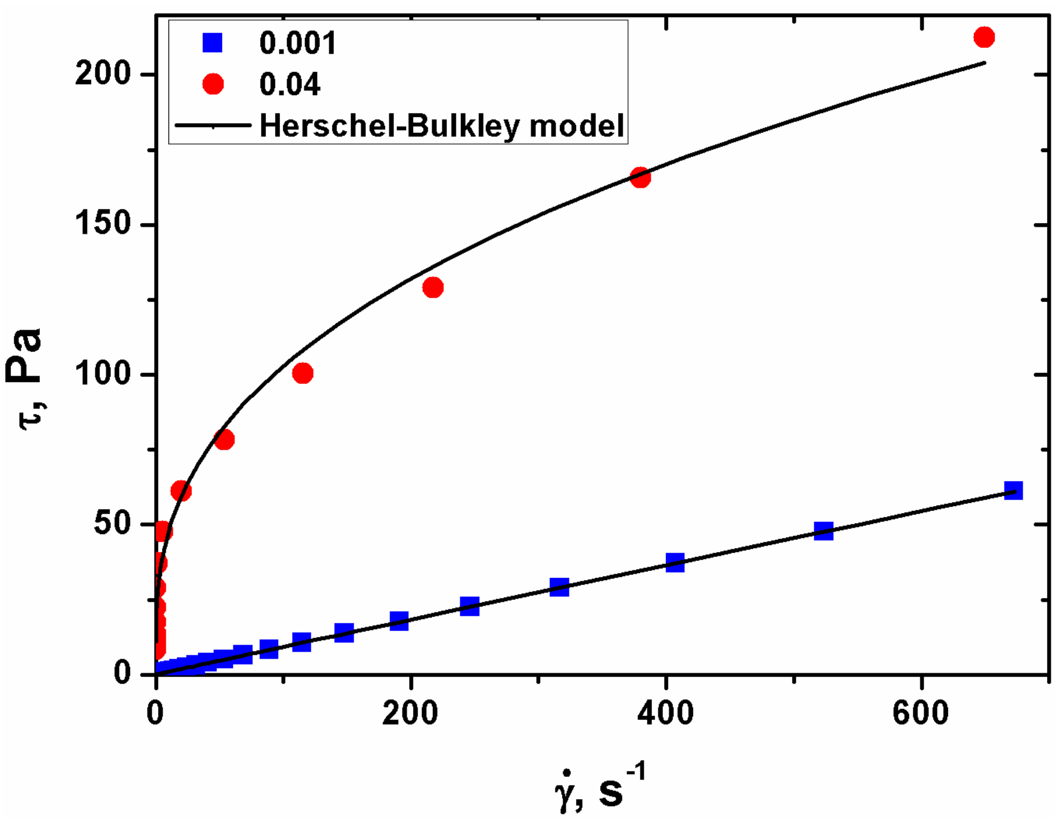

Fig. 7 Fitting of Herschel-Bulkley model to $F_{0.52}R_{0.38}I_{0.10}$.

Fig. 8 shows the relation between the yield stress and the total volume fraction for the three types of morphological mixtures. In Fig. 8(a), it is clearly shown that the logarithm of the yield stress is a linear function of the logarithm of the volume fraction, and all three curves are nearly parallel. A power-law relation suggested by Zhou et al. (1999) was used:

$$\tau_y = B\phi^c \tag{9}$$

where *B* and *c* are fitting parameters, and *B* can be expressed as

$$B = \frac{Ab}{24\pi h_0 d^2} \tag{10}$$

where A is the Hamaker constant; h_0 is the surface separation between two particles (Johnson et al. 1999); d is the diameter of the particle; and b is a fitting parameter. By dividing the yield stress with the parameter B, the function of yield stress versus volume fraction can be normalized as shown in Fig. 8(b), indicating no morphology and concentration influence on the dimensionless yield stress. A magnitude of 1.5 is obtained for the power-law exponent c using regression fitting. Many research groups have observed similar exponential dependence of yield stress and volume fraction, and the exponent is greatly dependent on the material system studied, such as an exponent of 4.2 for alumina suspensions (Zhou et al. 1999), 4.0 for zirconia suspensions (Leong et al 1995), 5.8 for milk fat suspensions, 3.0 for coco butter crystal suspensions, 2.1 for palm oil crystal suspensions (Marangoni and Rogers 2003).

Weak particle-particle linkages are considered as dominant in HCO crystal suspensions at the dilution ratios studied. For triacylglycerols the weak particle-particle linkages was suggested to be van der Waals attractive forces (Marangoni and Narine 2002). The yield stress reflects the breakage of such weak physical bonds. In Fig. 8(a), it is also found that fiber-rich suspension shows the highest yield stress at the same volume fraction, indicating fibers form the strongest HCO crystal network. The intercepts of the solid lines with the y-axis in Fig. 8(a) stand by lnB. The high yield stress reflects high value of parameter B in Eq. (10), which is derived based on the interactions of spheres. At a fixed volume fraction, smaller separation (h_0) between particles and particle size give higher yield stress, and vice versa. At the same volume fraction, compared to rosettes, fibers tend to have more physical interlock which gives much smaller h_0. Following the same thought, compared to irregular crystals, rosettes have much smaller h_0 too. Smallest particle size (length) of fibers also provides a high value B, leading to a high yield stress.

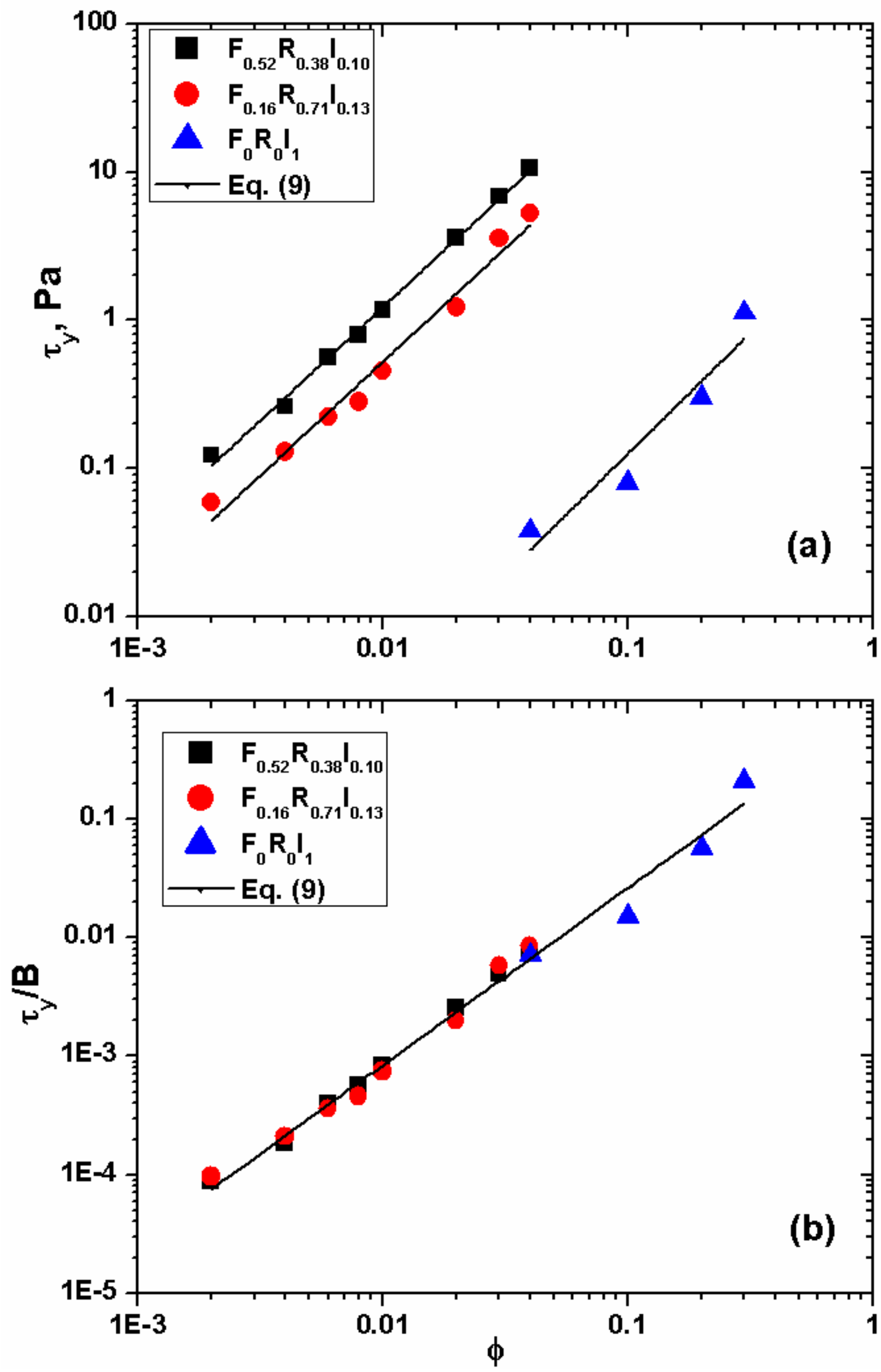

Fig. 8 Yield stress as a function of total volume fraction of the three mixtures. (a) Yield stress versus volume fraction; (b) normalized yield stress versus volume fraction.

Fig. 9 shows the volume fraction dependence of consistency *K* and flow index *n*. In Fig. 9(a), *K* shows a power-law function of particle volume fraction.

The flow index *n* shown in Fig. 9(b) suggests that the extent of shear thinning increased with the concentration and the aspect ratio. The dependence of shear thinning on the particle concentration suggests a particle-particle interaction mechanism. Shear thinning of viscosity was reported to relate with Peclet number and Reynolds number (Stickel and Powell, 2005). Stickel and Powell (2005) indicated that fluids showed Newtonian behavior when $Pe \geq 10^3$ and $\mathrm{Re} \leq 10^{-3}$. We obtained $Pe = 10 \sim 10^7$ and $\mathrm{Re} \leq 10^{-3}$ for our HCO suspensions. Therefore, all the experiments were conducted in the hydrodynamic regime and Brownian motion was considered negligible. Also, due to the small Reynolds number particle inertia could be negligible too, while viscous forces dominated indicating particles and fluid motions were fully coupled.

Shear thinning behavior for non-Brownian particulate suspensions at high Peclet number is not fully understood. *Pe* is so large that no significant reduced viscosity will be observed caused by shear-induced alignment. Shear induced adhesions between particles (Chaouche and Koch 2001) could be an explanation of such shear thinning. At low shear rate, flocs of particles form and break down with the increase of shear rate. Another explanation comes from Mueller et al. (2010) who hypothesized that the shear thinning was caused by the decrease of the local viscosity between gaps of particles. During shear flow, the shear rate in the small gap between two particles is higher than the bulk shear rate. Mueller et al. (2010) states that when the gap decreases, there will arise a point that the heat diffused out to the bulk is not enough, leading to a rise of local temperature in the gap. Thus, the viscosity in the gap will decrease resulting in the lubrication of one particle to another.

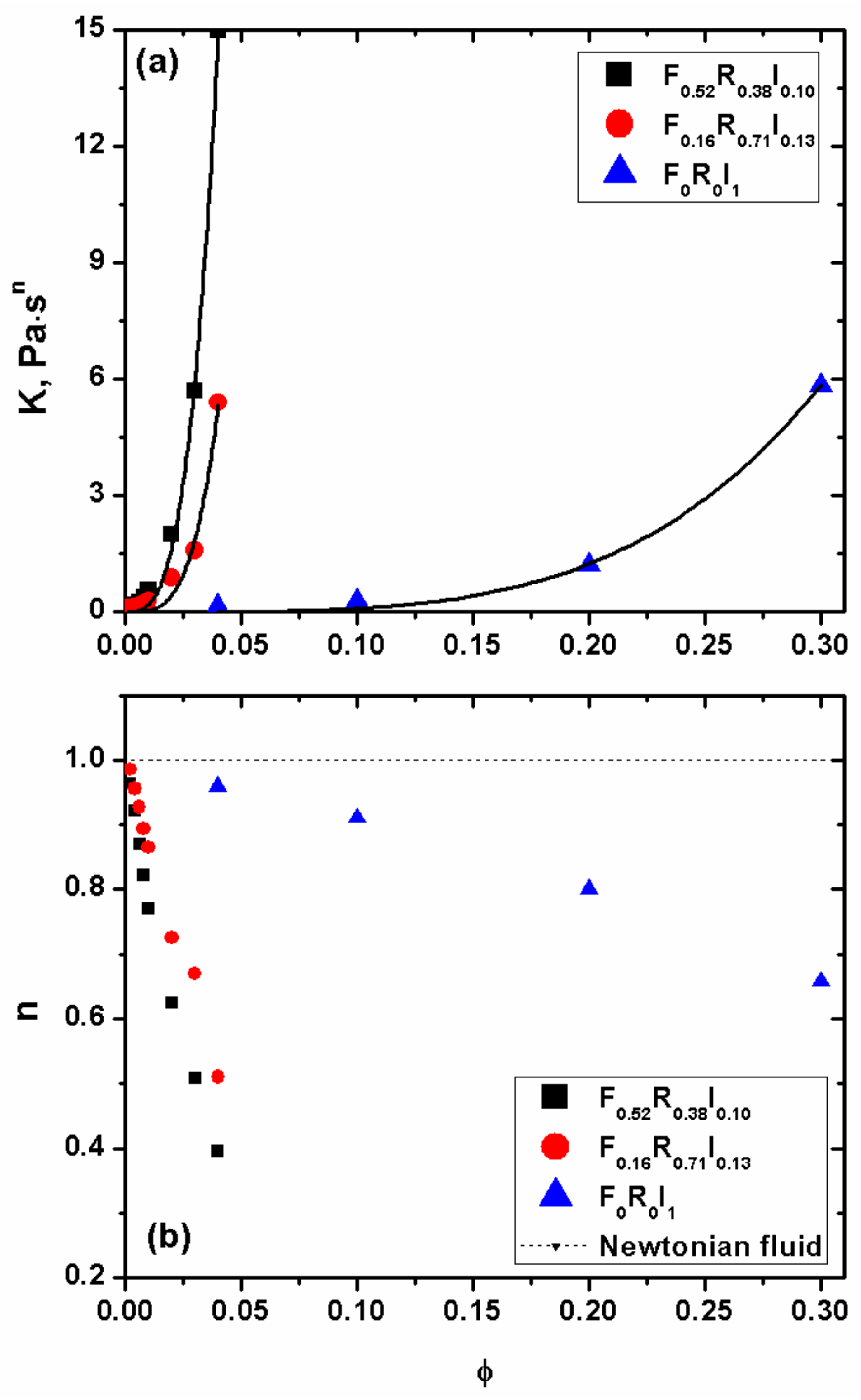

Fig. 9 Particulate volume fraction dependent (a) consistency *K* and (b) flow index *n*.

Conclusions

Rheology of three mixtures of HCO crystal morphologies has been studied to understand the relationship of rheology with crystal morphology. Rheological properties, intrinsic viscosity and yield stress, are functions of the volume fractions and crystal shape. The magnitudes of intrinsic viscosity and yield stress have the following decreasing sequence: fiber>rosette>irregular crystal. The Huggins coefficient is a decreasing function of morphology in the preceding sequence. A modified Farris model has been successfully applied on the mixture of morphology with particulate interactions. Concentrated suspensions show yield stress which is the power law function of total volume fraction.

Acknowledgements The authors thank Dr. Shiping Zhu for facilitating this work through the use of the ATS rheometer. The authors also thank Dr. John Vlachopoulos for his insightful comments.

References

Astarita G (1990) Letter to the editor: the engineering reality of the yield stress. J Rheol 34: 275-277.

Barnes HA, Walters K (1985) The yield stress myth. Rheol Acta 24: 323-326.

Brady JF, (1993) The rheological behavior of concentrated colloidal dispersions. J Chem Phys 99: 567-581.

Berry DH, Russel WB, (1987) The rheology of dilute dispersions of slender rods in weak flow. J Fluid Mech 180: 475-494.

Brenner H, (1967) Coupling between the translational and rotational Brownian motions of rigid particles of arbitrary shape. J Colloid Int Sci 23: 407-436.

Brenner H, (1974) Rheology of a dilute suspension of axisymmetric Brownian particles. Int J Multiphase Flow 1: 195-341.

Chaouche M, Koch DL, (2001) Rheology of non-Brownian rigid fiber suspensions with adhesive contacts. J Rheol 45: 369-382.

Chong JS, Christiansen EB, Baer AD, (1971) Rheology of concentrated suspensions. J Appl Polym Sci 15: 2007-2021.

Farris RJ, (1968) Prediction of the viscosity of multimodal suspensions from unimodal viscosity data. Trans Soc Rheol 12: 281-301.

Genovese DB, Lozano JE, Rao MA, (2007) The rheology of colloidal and noncolloidal food dispersions. J Food Sci 72: R11-R20.

Goddinger D, Nordende K, Schroeder T, (2009) Antidandruff Shampoo. US Patent 2009/0169644 A1, Henkel AG&Co, KGaA, Duesseldorf, DE.

Hartnett JP, Hu RYZ (1989) Technical not: the yield stress – An engineering reality. J Rheol 33: 671-679.

Hinch EJ, Leal LG, (1972) The effect of Brownian motion on the rheological properties of a suspension of non-spherical particles. J Fluid Mech 52: 683-712.

Horn FM, Richtering W, (2000) Viscosity of bimodal charge-stabilized polymer dispersions. J Rheol 44: 1279-1292.

Johnson SB, Franks GV, Scales PJ, Healy TW, (1999) The binding of monovalent electrolyte ions on α–Alumina. 2. The shear yield stress of concentrated suspensions. Langmuir 15: 2844-2853.

Krieger IM, (1972) Rheology of monodisperse lattices. Adv Colloid Interface Sci 3: 111-136.

Kuwahara T, Nagase H, Endo T, Ueda H, Nakagaki M, (1996) Crystal structure of DL-12-Hydroxystearic acid. Chem Lett 6: 435-436.

Larson RG, (1999) The structure and rheology of complex fluids. Oxford University Press Inc., NY.

Leal LG, Hinch EJ, (1973) Theoretical studies of a suspension of rigid particles affected by Brownian couples. Rheol Acta 12: 127-132.

Leong YK, Scales PJ, Healy TW, Boger DV, (1995) Effect of particle size on colloidal zirconia rheology at the isoelectric point. J Am Ceram Soc 78: 2209-2212.

Magauran, et al. (1994) Rheological additive comprising derivatives of castor oil. U.S. Patent, 5,340,390.

Marangoni AG, Narine SS, (2002) Identifying key structural indicators of mechanical strength in networks of fat crystals. Food Res Inter 35: 957-969.

Marti I, Hofler O, Fischer P, Windhab EJ, (2005) Rheology of concentrated suspensions containing mixtures of spheres and fibers. Rheol Acta 44: 502-512.

Macosko CW, (1994) Rheology: Principle, Measurements, and Applications, VCH Publishers Inc., NY.

Mewis J, Wagner NJ, (2009) Current trends in suspension rheology. J Non-Newtonian Fluid Mech 157: 147-150.

Merkus HG, Bellantone M, Scarlett B, (2009) Particle size measurements: fundamentals, practice, quality. Dordrecht, Springer, Netherlands.

Mor R, Gottlieb M, Graham A, Mondy L, (1996) Viscosity of concentrated suspensions of sphere/rod mixtures. Chem Eng Comm 148-150: 421-430.

Mueller S, Llewellin EW, Mader HM, (2010) The rheology of suspensions of solid particles. Proc R Soc A 466: 1201-1228.

Pabst W, Gregorova E, Berthold C, (2006) Particle shape and suspension rheology of short-fiber systems. J Euro Ceram Soc 26: 149-160.

Petrich MP, Koch DL, Cohen C, (2000) An experimental determination of the stress-microstructure relationship in semi-concentrated fiber suspensions. J Non-Newtonian Fluid Mech 95: 101-133.

Petrie CJS, (1999) The rheology of fibre suspensions. J Non-Newtonian Fluid Mech 87: 367-402.

Rogers MA, Wright AJ, Marangoni AG, (2008) Engineering the oil binding capacity and crystallinity of self-assembled fibrillar networks of 12- hydroxystearic acid in edible oils. Soft Matt 4: 1483-1490.

Russel WB, Saville DA, Schowalter WR, (1989) Colloidal Dispersions. Cambridge University Press, Cambridge.

Solomon MJ, Boger DV, (1998) The rheology of aqueous dispersions of spindle-type colloidal hematite rods. J Rheol 42: 929-949.

Solomon MJ, Spicer PT, (2010) Microstructural regimes of colloidal rod suspensions, gels and glasses. Soft Matt 6: 1391-1400.

Spicer PT, Hartel RW, (2005) Crystal comets: dewetting during emulsion droplet crystallization. Aust J Chem 58: 655-659.

Wierenga AM, Philipse AP, (1996) Low-shear viscosities of dilute dispersions of colloidal rodlike silica particles in cyclohexane. J Colloid Inter Sci 180: 360-370.

Yang D, Hrymak AN, (2011) Crystal morphology of hydrogenated castor oil in the crystallization of oil-in-water emulsions: Part 1. Effect of temperature. Ind Eng Chem Res 50: 11585-11593.

Yang D, Hrymak AN, Kamal MR, (2011) Crystal morphology of hydrogenated castor oil in the crystallization of oil-in-water emulsions: Part 2. Effect of shear. Ind Eng Chem Res 50: 11594-11600.

Zaman AA, Moudgil BM, (1998) Rheology of bidisperse aqueous silica suspensions: a new scaling method for the bidisperse viscosity. J Rheol 42: 21-39.

Zhou Z, Solomon MJ, Scales PJ, Boger DV, (1999) The yield stress of concentrated flocculated suspensions of size distributed particles. J Rheol 43: 651-671.

Chapter 6 Concluding Remarks

Crystal morphology of hydrogenated castor oil has been investigated in an oil-in-water emulsion system by considering the three important factors: temperature, shear and time. The suspension rheology modified by the arising crystal morphologies has been studied to generate the relation between morphology and rheological properties. The research objectives proposed in Chapter 1 have been fulfilled and the major conclusions and contributions are listed as follows:

1. Three major types of micron-sized crystal morphology have been observed: fiber, rosette and irregular crystal. Nano-fibers with the width of around 26.65 nm and length ranging from 80 to 5000 nm exhibiting chiral structures have been confirmed by TEM as the elements of both macro- fibers and rosettes.

2. Fibers and rosettes have been found to show the same polymorphic structures but different shapes, suggesting different nucleation mechanisms. The d-spacing at 4.46 and 3.97 Angstroms are not conventional polymorphic form of beta prime. This could be attributed to the hydroxyl bond or the existence of surfactant. A lower activation free energy for the rosette than the fiber indicates that the heterogeneous nucleation interface for the rosette demands less supercooling. The conclusion that the growth of rosettes requires low supercooling is a new addition to the literature. Normally, high supercooling is favored for spherulites where the crystal growth rate is greater than the diffusion rate in the melt. Irregular crystals

have been found to form under highest supercooling and show thermal instability. A solid phase transition from unstable irregular crystals into thermally stable rosette-like structures starts from the surface of irregular crystals.

3. The non-isothermal crystallization study showed that the formation of rosettes and fibers was favored by a slow cooling rate (1°C/min) while the formation of irregular crystals was favored by a fast cooling rate (5°C/min).

4. Shear increased the nucleation rate, and the induction time to nucleation was shown to be linear proportional to the logarithm of the shear rate. Fibers were favored by gentle shear (e.g., 1 s^{-1}), but fibers can be broken up with increased shear time. A detailed study on the crystal breakage is shown in the Appendix.

5. Kinetic study of isothermal crystallization has shown that induction time of nucleation linearly increases with the increase of the isothermal temperature under which crystallization occurred for both fibers and rosettes.

6. The Avrami model has been modified by introducing the volume fraction of each type of morphology into three dimensional and one dimensional full Avrami models, and has been found to be able to capture experimental trends better than the traditionally used simplified equation format.

7. The viscometry of dilute suspensions has shown that the magnitude of intrinsic viscosity is dominated by the fraction of a crystal morphology type, i.e. fiber >

rosette > irregular crystal.

8. A modified Farris model has been fitted to the rheology data from mixtures of crystal morphology with interacting particles providing an empirical correlation between relative viscosity and crystal morphology for dilute dispersions.

9. A yield stress has been found for concentrated suspensions followed by a shear thinning behavior with increased shear rate. A power-law relation has been found between yield stress and total particle volume fraction, and a constant exponent of 1.5 has been obtained regardless of crystal morphology.

Appendix A Effect of Shear on the breakage of Hydrogenated Castor Oil Crystals in Concentrated Aqueous Dispersions

In this chapter, I performed all the experiments and characterization. Dr. Andrew Hrymak supervised this work and participated in the edits.

Introduction

In industrial processing and during transportation it is common for the processing steps (e.g. pipe flow, pumping) to break crystal particles (Reynolds et al. 2005), to affect the morphology, and thus the rheology of particulate dispersions. The breakage is determined by two processes: the mechanical strength of crystals and the forces loaded on the crystals. The mechanical strength is influenced by the attachment energy between crystal units. The applied breaking force could come from collisional mechanical break-up or turbulent fluid-mechanical break-up (Sung et al. 1973, Evans et al. 1974). Collisional break-up may happen during crystal-wall or crystal-crystal interactions. Fluid-mechanical break-up is caused by shear stresses on the crystal due to drag or pressure effects.

The rheology of particulate dispersions is affected by many factors, such as particle size distribution, morphology, volume fraction and medium and so on (Mewis and Wagner 2009). Particle size distribution and morphology are two factors that are affected during the shear flow breakage of particles.

In this section, HCO crystal breakage is studied in aqueous dispersions under simple steady shear flow by considering the following factors: shear rate, time under shear and initial crystal morphology.

Experimental

Materials

A material system containing 4 wt% of hydrogenated castor oil (HCO) crystals in 96 wt% aqueous sodium linear alklybenzene sulfonate (NaLAS, 16 wt% in total) was used for the breakage study.

Polarized Light Microscopy

A polarized light microscope (VWR Vista Vision, USA) with transmitted polarized light was used for crystal morphology observation and size measurements (with a 40 × objective lens). A drop of crystal suspension with fixed amount of 10 μl was loaded on the microscope slice and then covered with a cover slip. The drop of suspension can automatically spread between the microscope slice and cover slip to form a cover slip sized uniform film with uniformly dispersed particles. Then, the amount of particles counted for different samples can be compared. A digital camera (VWR VistaVision, USA) was used for recording micrographs and ImageJ (NIH, USA) was used for image analysis. More than 600 particle measurements were done to calculate the sizes and number fraction of each morphology.

Transmitted Electron Microscopy

A JEOL 1200 EX TEMSCAN transmission electron microscope (JEOL, USA) operated at 80 kV was used for the observation of the nano-scaled crystals and fragments created by shear stresses. Prior to observation, a drop of HCO crystal solution with the volume approximately 1.57 μl was loaded on Formvar-coated copper grids (Canemco Inc., Quebec, Canada) and dried in natural air. The 4 wt% HCO suspension was diluted 10 times with 16.7 wt% of surfactant and then 10,000 times with water to avoid the aggregation of crystals. In the results section, μl means every microlitre of 100,000-time diluted dispersions. Therefore, the total HCO volume fraction in every microlitre 100,000-time diluted dispersions can be calculated as 4E-07. By counting the number and size of nano-fibers on every TEM grid the volume fraction of nano-fibers can be calculated. Then, the volume fraction of nano-fibers among the total HCO can be obtained.

Rheometer

An ARES strain-controlled rheometer (TA Instruments, USA) was used for the crystal breakage studies using two parallel plates (40 mm in diameter, gap size 1.5mm) to provide a defined shear on HCO samples. Shear rates from 10 s^{-1} to 700 s^{-1} and shear times from 30 sec to 50 min were applied. Therefore, the microstructures (Mewis, 1979; Barnes, 1997) of suspensions were different compared to the original suspension which caused different rheology behaviors. Mainly two reasons contribute to the microstructure variation: the breakage of crystals and the rearrangement of particles. To compare the rheology of the particulate suspensions after shear caused only by the crystal breakage, the sheared products were diluted 10 times with the same concentration of surfactant NaLAS and allow the microstructure to recover for 48 hours.

Rheological measurements were carried out in a stress-controlled ATS rheometer

(Rheologica, USA) using a cone and plate (40 mm in diameter, 2° cone angle) shear device. Steady shear stress was applied from 0.01 to 500 Pa. All experiments were carried out at 25°C.

Results and discussion

Crystal morphology

As discussed previously, three types of micron-scaled HCO crystal morphologies (rosettes, fibers and irregular crystals) were observed. TEM images show that fibers observed at the optical microscope level are actually nano-fibrous structures made up of fibers with a mean thickness of 26.65±9.09nm (Figure A.1a) with branches often observed. Individual nano-fibers (normally the lengths are less than 1 μm) exhibited chirality (Kuwahara, 1996; Rogers, 2008) as shown in Figure A.1b. It is not clear whether these are fragments broken down from rosettes or macro-fibers (Figure A.1c), or form due to primary nucleation. Note: “fragments” are used to describe the structures shown in Figure A.1b. In Table A.1, it is shown that there exists tremendous amount of fragments.

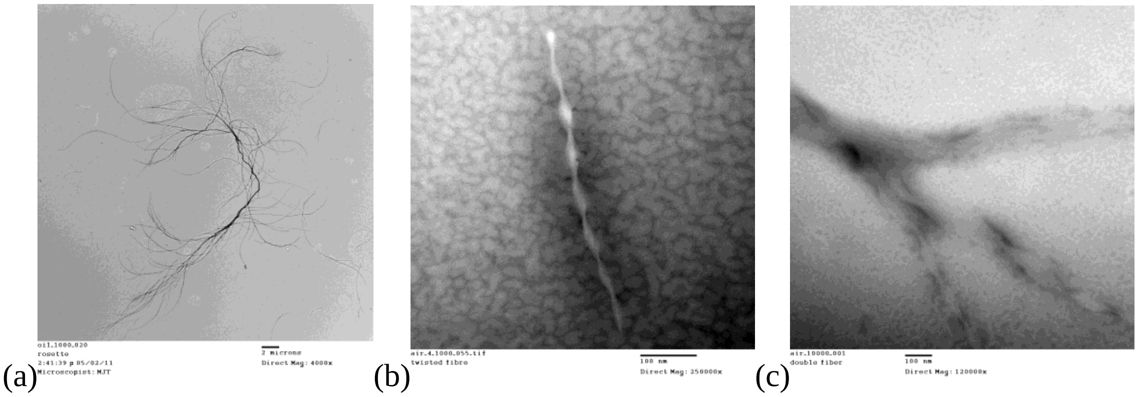

(a) (b) (c)

Figure A.1 TEM images for (a) fiber; (b) nano-sized fibrous fragments; (c) broken fragments.

Table A.1 Parameters of micro- and nano- sized crystals of the 4% original HCO suspension.

Parameter	Fiber	Rosette	Irregular	Fragments
Number per µl	26.1	23.6	1.27	1.29E+09
Diameter or length (µm)	10.9	19.9	3.27	1.24
Width (nm)	910	-	-	26.7
Volume fraction	1.11E-04	0.467	1.12E-04	0.532

Effect of shear rate and shear time on the number density

After various shear histories, the numbers of fibers and rosettes were counted and divided by the numbers of fibers and rosettes in the original suspension before shear. Therefore, the number fraction of particles for the original suspension equals to 1 which is shown as the solid sphere in Figure A.2. It is found in Figure A.2(a) that at the shear rate of 10 s^{-1}, the number of fibers increases at the first 30 seconds and then decreases with further increasing the shear time. The same trend happens at the shear rate of 50 s^{-1} but the increases amount of fibers at the shear time of 30 seconds is higher than that at the shear rate of 10 s^{-1}. When the shear rate was above 100 s^{-1}, the number fraction of fibers decreased with the increase of shear time. In Figure A.2(b), it is shown that the number fraction of rosettes decreases with the increase of both shear time and shear rate. However, at the shear rate lower than 100 s^{-1}, the amount of rosettes lost is much smaller than that of fibers, indicating fibers are easier to break down at the same shear stress.

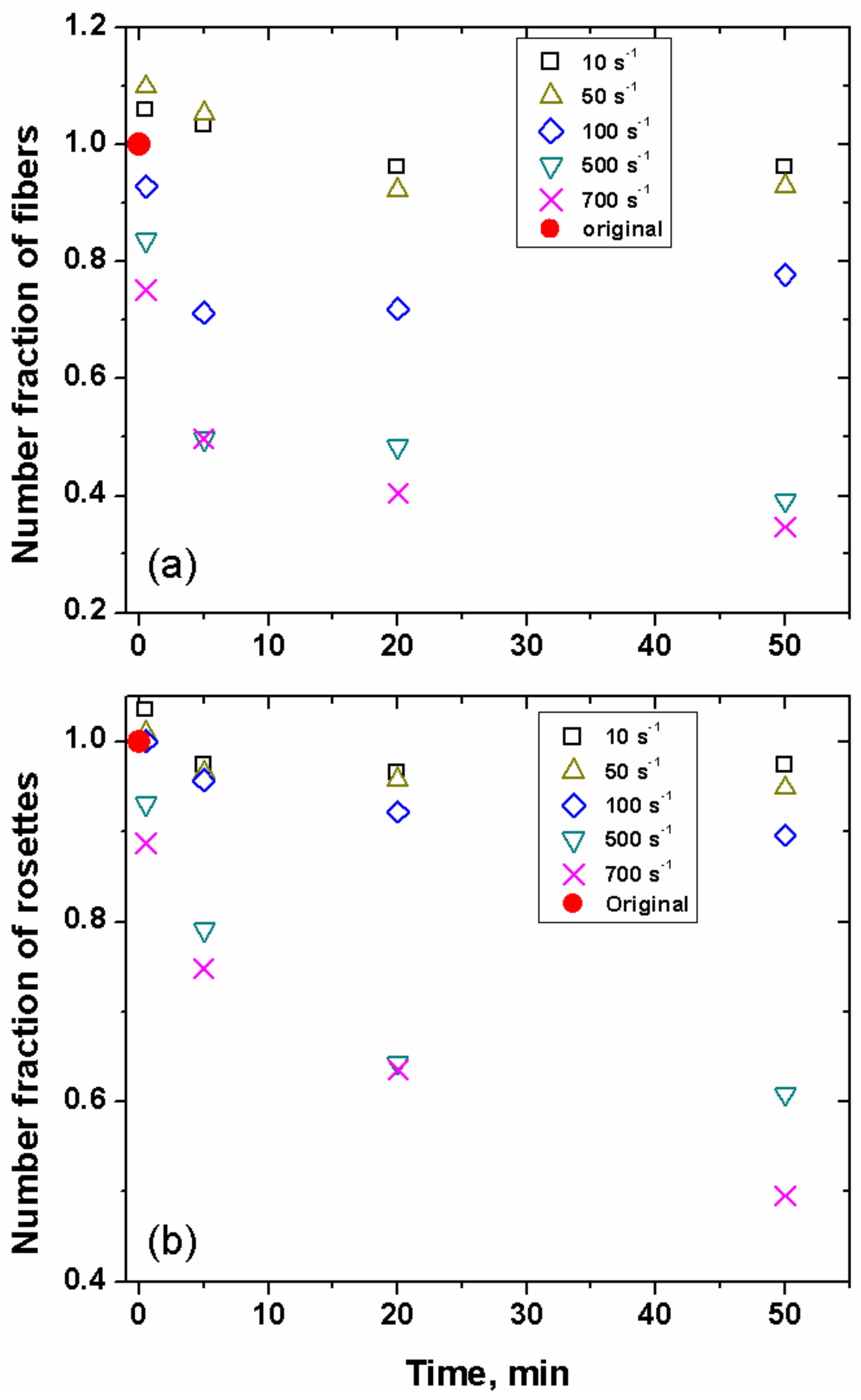

Figure A.2 Number fraction of different crystal morphology at various shear conditions.

Effect of shear rate and shear time on the crystal size distribution

The mean length of fibers and mean diameter of rosettes were obtained by light microscopy and the results are shown in Figure A.3. It is found that the higher the shear rate, the smaller the average length of fibers and diameter of rosettes. In Figure A.3, at a fixed shear time it is found that when the shear rate is less than 100 s^{-1}, the average dimensions of both fibers and rosettes decrease slowly with the increase of shear rate from 10 s^{-1} to 100 s^{-1}. A dramatic decrease of dimension happened when shear rate increased to 500 s^{-1}.

At each shear rate, the average dimensions of both fibers and rosettes decrease almost 50% among the total decrement in 5 min. With increased shear time, a plateau tends to form, indicating no breakage happens with further increasing the shear time.

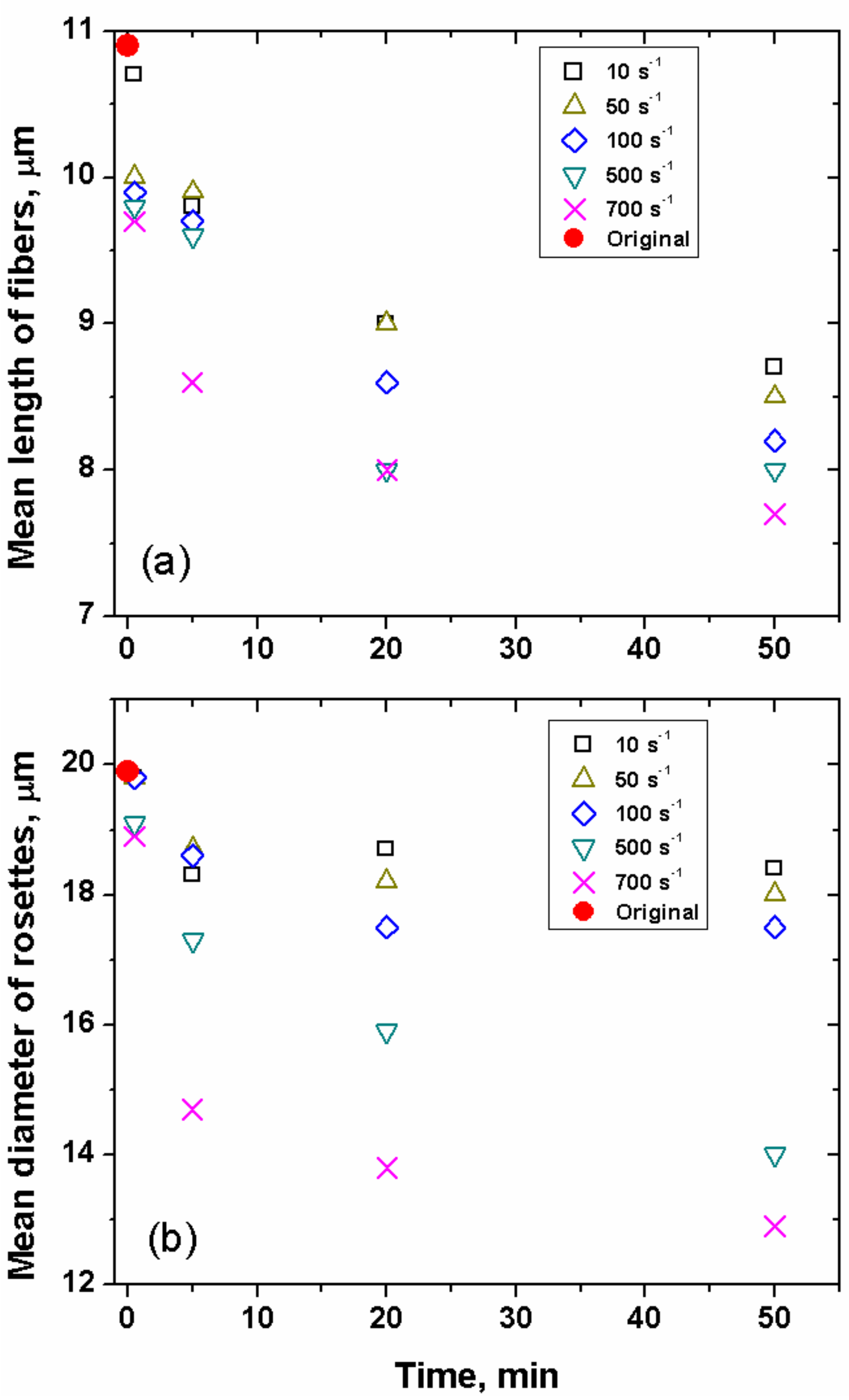

Figure A.3 Variation of mean lengths of fibers (a) and diameters of rosettes (b) at different shear rate and time.

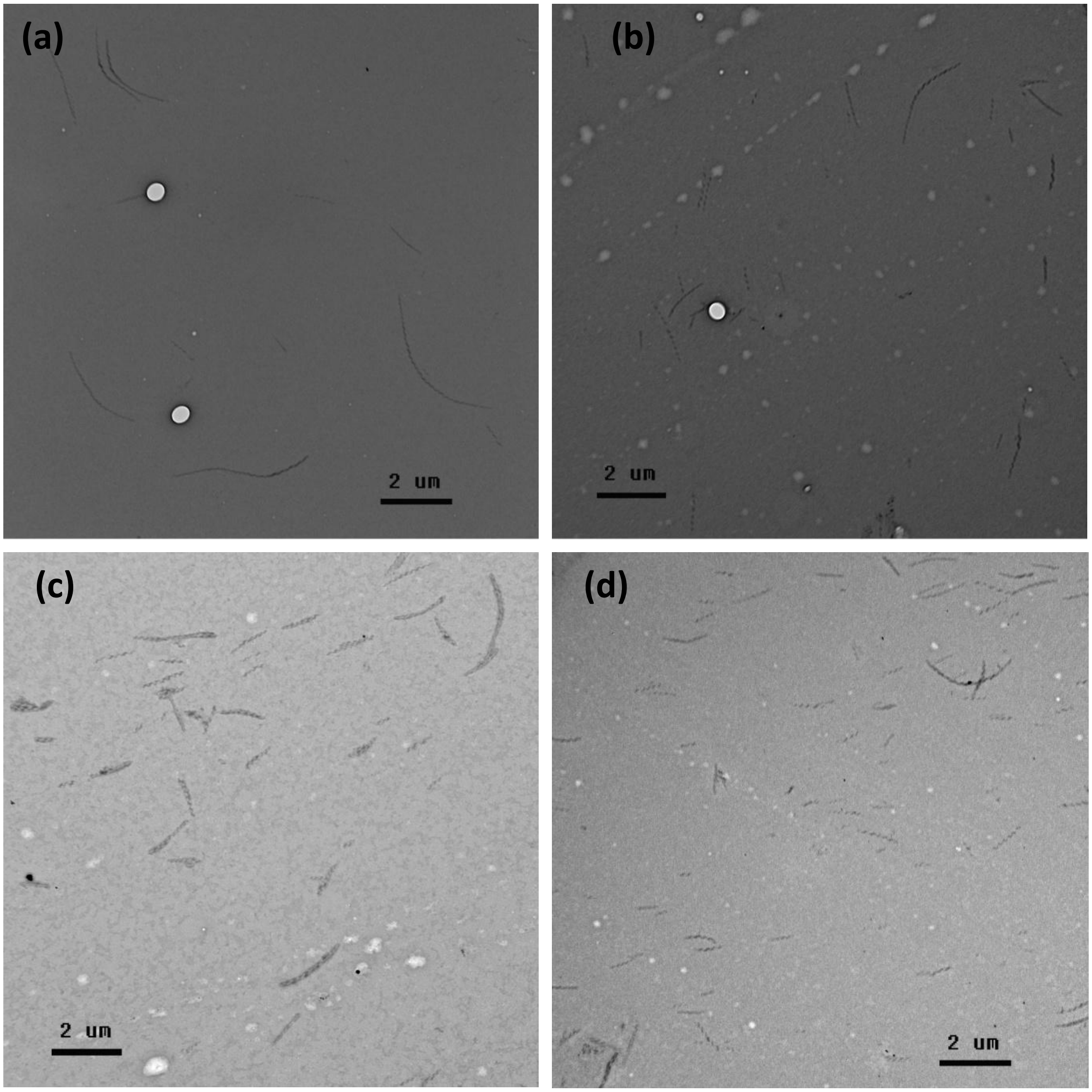

Figure A.4 TEM images of nano-fibrous fragments at the shear rate of 500 s^{-1} for (a) 0 sec; (b) 1 min; (c) 10 min; (d) 50 min.

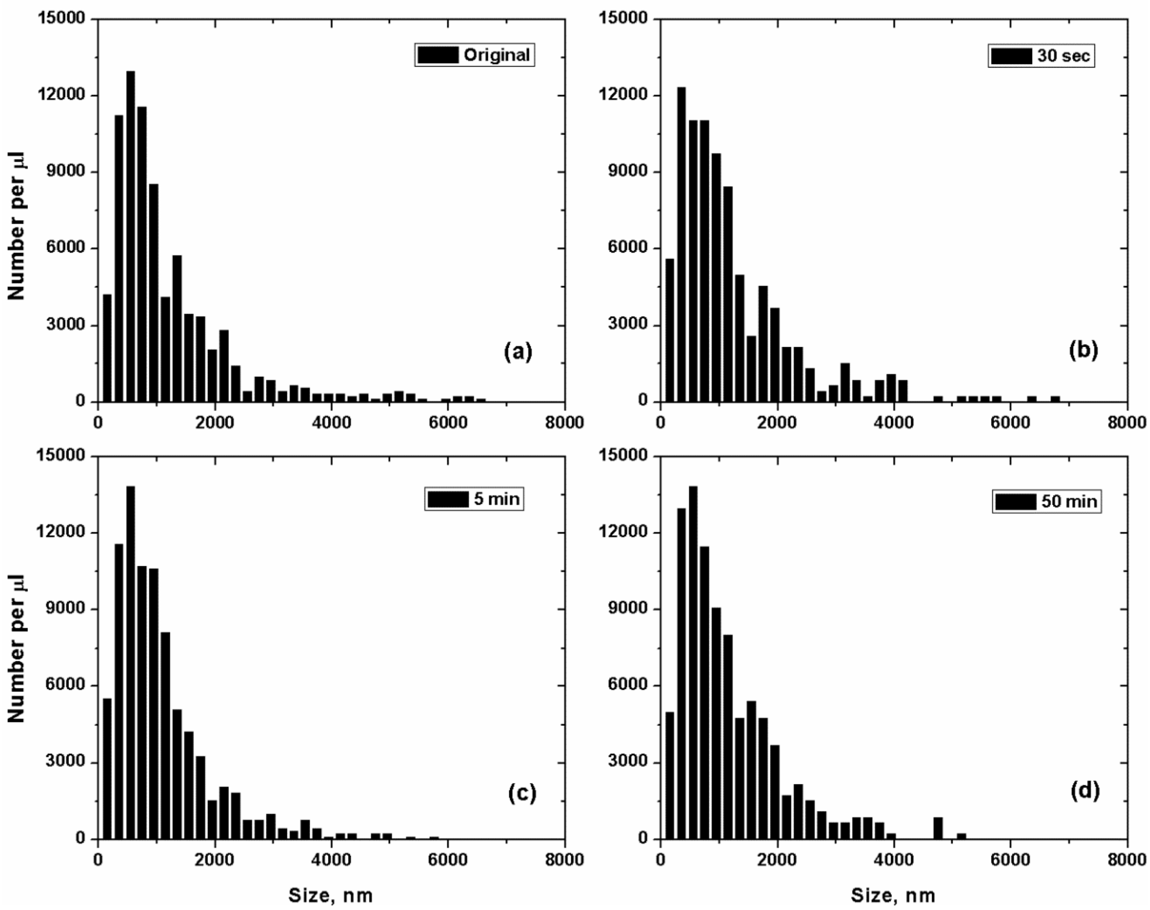

Figure A.5 Crystal size distribution of nano-fibrous fragments at a shear rate of 50 s^{-1} for (a) 0 s; (b) 30 s; (c) 5 min; (d) 50 min.

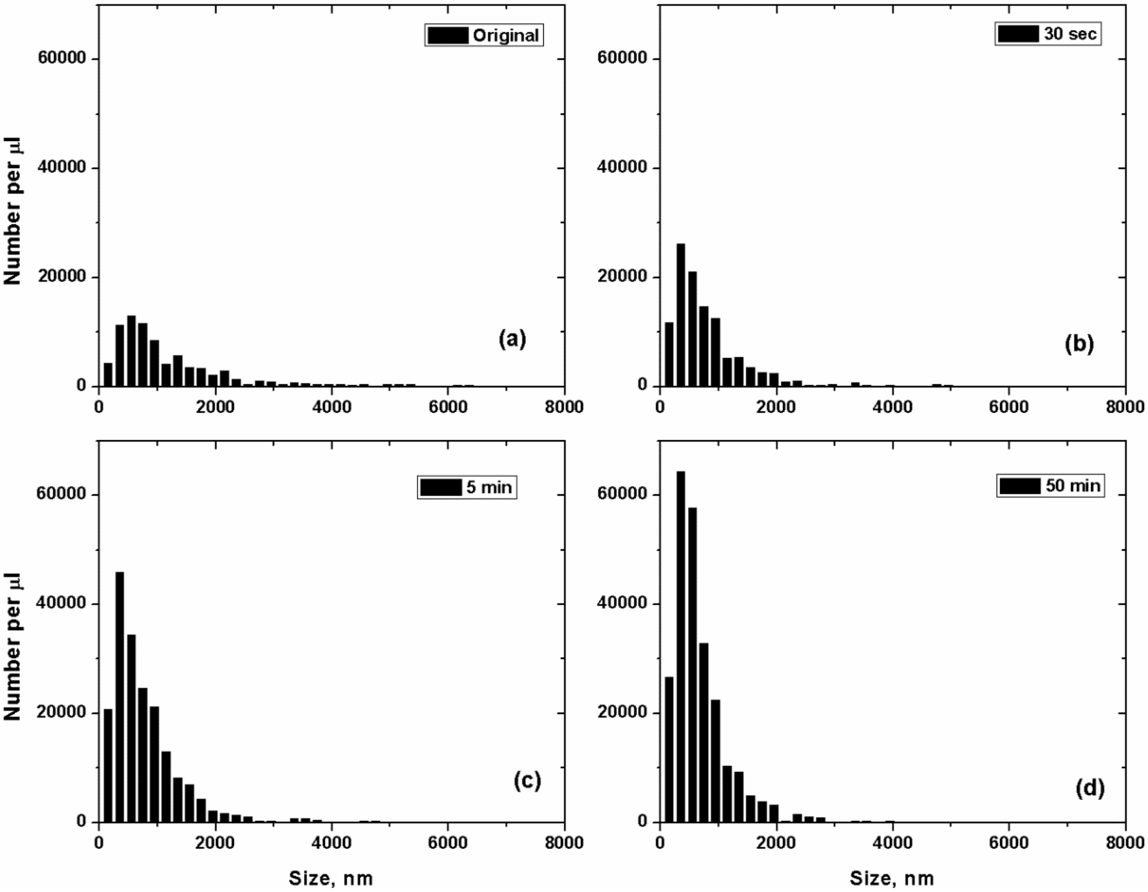

Figure A.6 Crystal size distribution of nano-fibrous fragments at a shear rate of 500 s^{-1} for (a) 0 s; (b) 30 s; (c) 5 min; (d) 50 min.

Figure A.4 shows the TEM images of fragments sheared at 500 s^{-1} for different times. Increasing number and decreasing length were found with increased shear time. Figure A.5 and A.6 show the crystal size distribution of nano-fibrous fragments at 50s^{-1} and 500 s^{-1} sheared for 0 sec to 50 min respectively. At 50 s^{-1} shear, the number density of fragments slightly increases with the shear time. However, at 500 s^{-1}, the number density of fragments increases dramatically with the shear time, and the size distribution shifts to the lower size region. The increment of number density of fragments is likely to be caused by breakage of arms of rosettes and fibers, and longer nano-fibers.

Figure A.7 shows the mass balance analysis by comparing the decreased mass of micro-sized particles (mainly rosettes) and the increased mass of nano-fibers. Although the discrepancy exists, the image analysis method used for breakage study provides a decent level of accuracy.

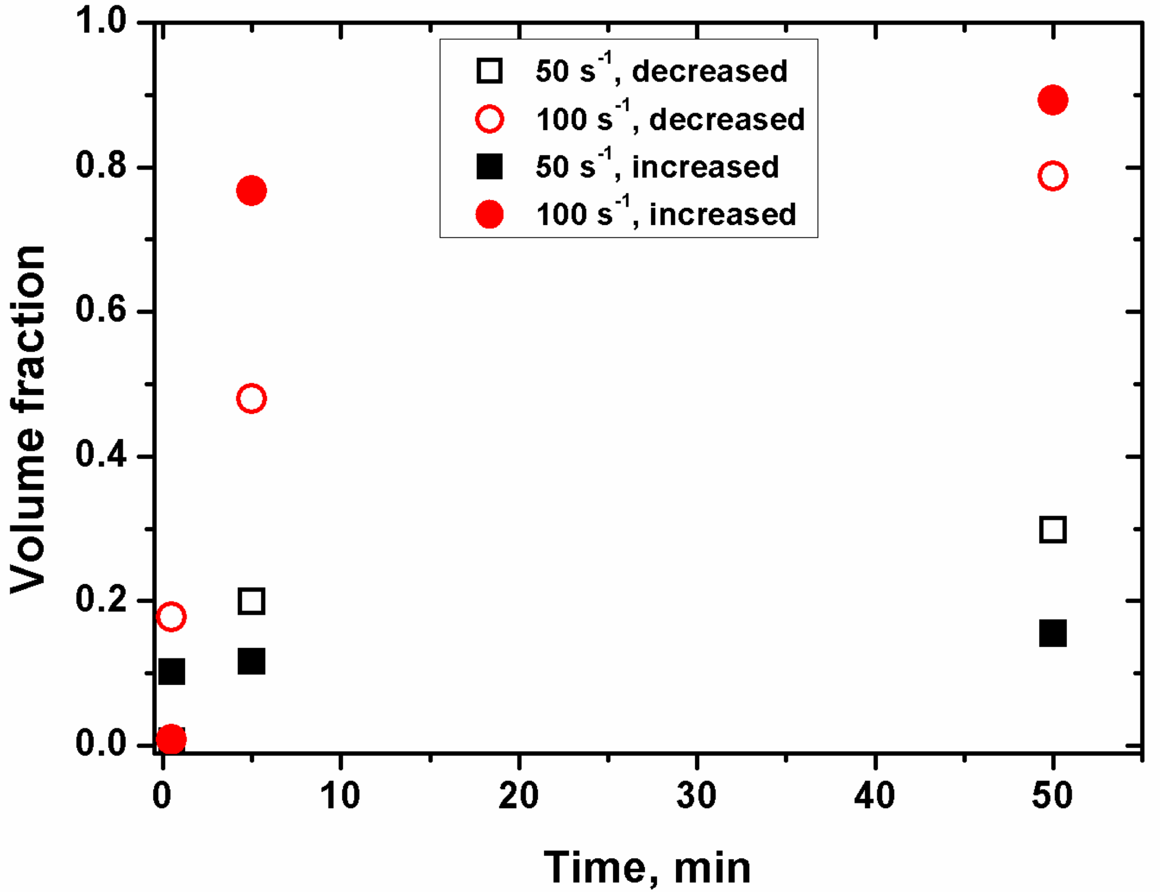

Figure A.7 Mass balance analysis.

Mechanism of crystal breakage

The material system with 4 wt% HCO is considered a concentrated suspension, so particle- particle interactions are dominant (Mewis and Macosko, 1994). Therefore, it is suggested that the decrease in particulate dimensions is due to the collisions between particles. Meanwhile, particles tend to periodically rotate depending on the geometry and concentration based on *Jeffery Orbit* (Jeffery, 1922; Goldsmith and Mason, 1967). Compared to rosettes, fibers are more geometrically sensitive to shear, so much more obvious changes on the number fraction and mean dimensions for fibers were found.

In Figure A.8, the mechanisms of the breakage for both fibers and rosettes into nano-fibrous fragments are proposed based on the experimental data obtained. *Mechanism 1* shows that fibers break down into shorter fibers first and then further break into nano-fibrous fragments. *Mechanism 2* states that nano-fibrous fragments are broken down from the fibers without the appearance of the interim shorter fibers. Whether *Mechanism 1* or *Mechanism 2* dominates depends on the balance between local shear stress and the attached free energy (Garti and Sato, 2001) of crystal lattices. A higher shear stress than attached free energy is required to break nanofibers, while much larger shear stress is necessary to break a bundle of nanofibers (micro-fibers). At low shear rate and shear time *Mechanism 1* tends to increase the number fraction of fibers, where *Mechanism 2* does not. However, both the two mechanisms contribute to the decay of length distribution. In Figure A.2(a), at the shear rate lower than 50 s^{-1} and shear time smaller than 30 seconds the number fraction of fibers increases, indicating *Mechanism 1* dominates. When the shear rate reaches to 100 s^{-1}, the number fraction of fibers decreases even at a shear time of 30 seconds. This is probably because the increased fibers breaks down into fragments immediately based on *Mechanism 1*. *Mechanism 2* is always likely to happen during the shear history used.

Mechanism 3 shows that rosettes experience a reduction in diameter rather than disintegration. *Mechanism 4* states that rosettes break into several clusters of fiber arms first and then the clusters break down into single fibers. These single fibers can break into fragments through either *Mechanism 1* or *Mechanism 2* or both. Within the shear rate and shear time used, clusters of fibers disintegrated from rosettes were rarely observed, indicating *Mechanism 4* was not likely in this study. Therefore, *Mechanism 3* dominates the breakage of rosettes.

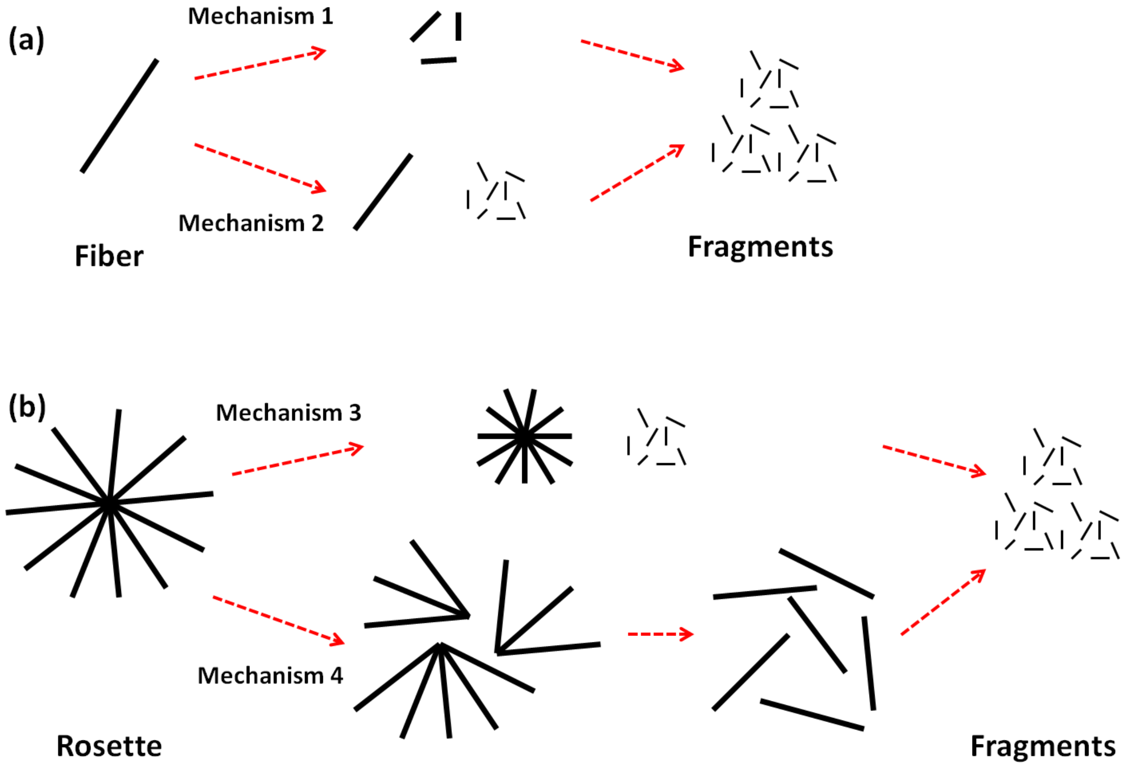

Figure A.8 Mechanisms of the breakage of fibers (a) and rosettes (b).

Rheology

The 4 wt% HCO original suspension was diluted 10 times after shear and dispersed well with gentle shear. Shear thinning behavior was observed for the HCO suspension. Low shear viscosity at the shear rate of 0.01 s^{-1} for all the after-shear suspensions are shown in Figure A.9, and decreased with increased shear rate and shear time. The decrease of low shear viscosity is attributed to the decrease of the mean sizes of rosettes and fibers as well as the decrease of aspect ratio of nano-fibrous fragments. However, due to the difficulty of separating the morphologies, we do not know how much one type contributes to the rheology of the whole suspension.

In Figure A.9(a), when shear rate is fixed, it is found that the viscosity decreases dramatically at the shear time from 0 to 5 min but much less between the shear time of 5 min and 50 min. Also it is shown that the viscosity data exhibited a plateau with increased shear time, and the plateau occurred earlier at higher shear rates. Figure A.9(b) shows that at a fixed shear time of 30 sec, viscosity decreased at shear rates less than 100 s^{-1} but plateaued at shear rates above 100 s^{-1}. Thus, 30 seconds of shear time is too short for the crystal to break to a significant extent.

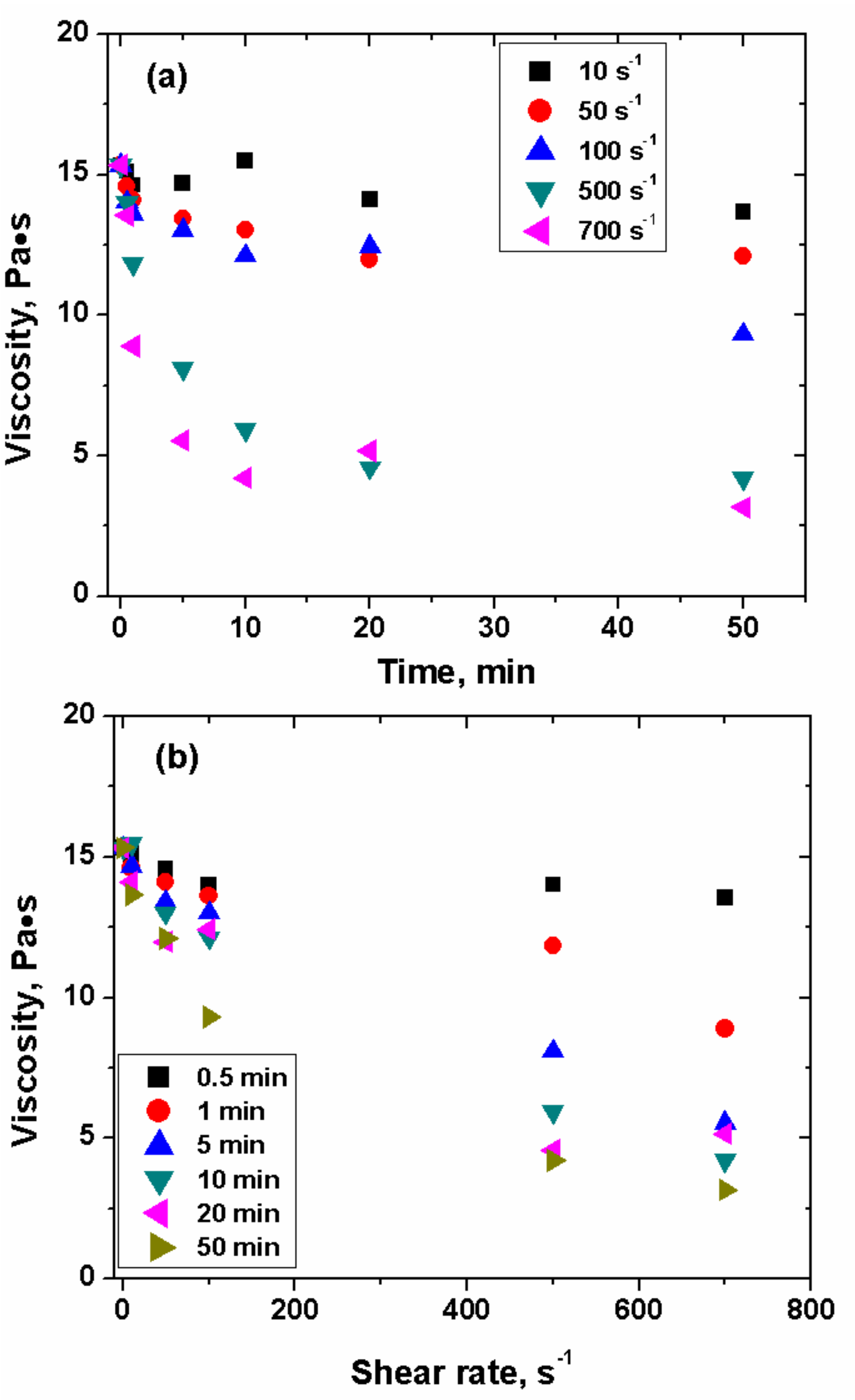

Figure A.9 Viscosity of shear broken suspensions at various (a) shear time and (b) shear rates.

Conclusions

Nano-fibrous fragments with a chiral structure have been observed by TEM after steady shear exposure to a 4 wt% HCO suspension. The micro-fibers have been found to be a bundle of the nano-fibrous structures and sensitive to shear. Under sustained shear histories, a decrease in the dimensions of fibers and rosettes and an increased amount of nano-fibrous fragments were found. The number fraction of fibers increases at low shear rate and shear time but decrease with shear rate above 100 s^{-1}. The number fraction of rosettes decreases with the shear rate and shear time. The mechanisms of crystal breakage have been proposed. The increased mass of nano-fibrous fragments is caused by the decreased mass of micro- fibers and rosettes. The mass balance analysis shows that the experimental accuracy is in a decent level. The viscosity of the sheared suspension has been found to decrease at low shear rates due to the decrease of the dimensions of rosettes and fibers and the aspect ratio of nano-fibrous fragments.

References

Barnes HA, (1997) Thixotropy- a review. J Non-Newtonian Fluid Mech 70: 1-33.

Evans TW, Margolis, GD, Sarofin AF, (1974) Mechanisms of secondary nucleation in suspension crystallizers. AIChE J 20: 950-958.

Garti N, Sato K, (2001) Crystallization Processes in Fats and Lipid Systems. Marcel Dekker Inc., NY, USA.

Goldsmith HL, Mason SG, (1967) Microrheology of dispersions. In: Eirich FR (ed)

Rheology, vol. 4, Pergamon, New York, pp 85.

Kuwahara T, Nagase H, Endo T, Ueda H, Nakagaki M, (1996) Crystal structure of DL-12-Hydroxystearic acid. Chem Lett 6: 435-436.

Jeffery GB, (1922) The motion of ellipsoidal particles immersed in a viscous fluid. Proc R Soc Lond A 102: 161-179.

Mewis J, (1979) Thixotropy- a general review. J Non-Newtonian Fluid Mech 6: 1-20.

Mewis J, Macosko CW, (1994) Suspension rheology. In: Macosko CW (ed) Rheology: Principle, Measurements, and Applications, VCH Publishers Inc., NY, pp 425-474.

Mewis J, Wagner NJ, (2009) Current trends in suspension rheology. J Non-Newtonian Fluid Mech 157: 147-150.

Reynolds GK, Fu JS, Cheong YS, Hounslow MJ, Salman AD, (2005) Breakage in granulation: a review. Chem Eng Sci 60: 3969-3992.

Rogers MA, Wright AJ, Marangoni AG, (2008) Engineering the oil binding capacity and crystallinity of self-assembled fibrillar networks of 12- hydroxystearic acid in edible oils. Soft Matt 4: 1483-1490.

Sung CY, Estrin J, Joungquist GR, (1973) Secondary nucleation of magnesium sulphate by fluid shear. AIChE J 19: 957-962.